APPLICATION OF ADDITIVELY MANUFACTURED MICRO-PIN ARRAY RECEIVER FOR CONCENTRATED SOLAR POWER GENERATION

By

RAYMOND PERE ODELE
THESIS

Submitted in partial satisfaction of the requirements for the degree of

MASTER OF SCIENCE

in

MECHANICAL AND AEROSPACE ENGINEERING

in the

OFFICE OF GRADUATE STUDIES

of the

UNIVERSITY OF CALIFORNIA

DAVIS

Approved:

VINOD NARAYANAN, Chair

PAUL ERICKSON

BRYAN JENKINS

Committee in Charge

2021

ABSTRACT

Concentrated solar power is being investigated by the U.S. Department of Energy (DOE) as a renewable energy source for meeting baseload and peak load electric power. The gas receiver pathway, utilizing supercritical CO_2 as the working fluid, has been identified as a potentially viable source of implementing CSP technologies because of recent interest in supercritical carbon dioxide Brayton cycles [1]. In past studies, lab-scale experiments and on-sun test done on a micro-pin-array solar receiver utilizing sCO_2 as the heat transfer fluid have shown the ability to absorb heat flux up to 100W/cm^2 at thermal efficiency above 90 percent[2], [3]. The feasibility of using microscale unit cells, as building blocks for a megawatt-scale (250MW thermal) open solar receiver through a numbering-up approach, where multiple microscale unit cells are connected in parallel, has been explored by Zada et al.[4]. In the previous studies, a microlamination approach (in which the pin array is chemically etched in a sheet and diffusion bonded to a flux plate) is used in the manufacture of these receivers. The limitation of this manufacturing method has a consequence in limiting the pin array length of the receiver. These short pin array lengths would require more unit cells in the receiver, and thus a more complicated header system. Also, a notable assumption from previous studies is that a uniform heat flux is imposed on the receiver module(s) over a period, whereas in a heliostat field, the flux distribution is highly non-uniform and varies temporally and spatially.

In this study, additive manufacturing of the receiver is presented as an alternative means of manufacturing the receivers. Additive manufacturing enables longer pin array lengths, thus reducing the complexity and mass of the header network. In order to study the performance of the receivers, and account for the spatial variation of properties throughout the receiver, a numerical code with a 2-dimensional discretization is developed and the performance of the additively manufactured pin array receiver (AM^{2}PAR) and the microlaminated pin array receiver (µLPAR) are compared at their respective

design lengths. Furthermore, this work explores the impact of non-uniform heat flux on a AM^{2}PAR central tower receiver. The heat flux data for a select geographical location has been modeled with NREL's SolarPILOT to model hourly heat flux distribution over a central receiver on a typical hot summer day. The flux data from SolarPILOT is used in numerically modeling the thermal and hydraulic parameters in the modules of a central receiver with an area of 250m^2 (7.5m radius and 10m height). The non-uniformity effects are compared with the results of a uniform-flux model. The study results present the estimated mass flow distribution for the novel receiver design needed to heat supercritical CO_2 from 550℃ to 720℃ with a maximum permissible pressure drop of 4 bar. The central receiver's surface temperature distribution is assessed to highlight non-uniformity in surface and fluid temperature distribution due to the flux non-uniformity. Thereafter, a novel receiver concept of using variable height pin arrays: VPH-AM^{2}PAR is explored. In such a receiver, the modules will have varied pin heights in accordance with the respective flux on the module. It is shown that the VPH- AM^{2}PAR is effective in reducing the peak surface temperature on the receiver. The study addresses the thermofluidic operating adjustments required and the total thermal power generated to ensure the creep life of the receiver meets a 30 year lifetime requirement.

ACKNOWLEDGEMENTS

I firstly wish to give gratitude to God for his strength throughout my program. I lean on God for speed, strength, provision and direction and I am grateful to God for seeing me through to this stage.

I want to also acknowledge my advisor, Professor Vinod Narayanan, for his tutelage. I am thankful for his guidance and frequent meetings in which I built a firmer knowledge and application of heat transfer towards writing up this thesis and pivoting my engineering career. I appreciate the rigor with which professor Vinod executes his work, reading every line of my work to make ensure an enhanced clarity of

Furthermore, I acknowledge my loving wife, Elsie, for her constant support throughout my program whilst we were engaged and continuing to support me towards the end of the program—during which we got married. All the time spent editing the work, helping me be more efficient, and checking in on my progress means a lot to me.

I acknowledge my family members—my mum and siblings—for being a great back bone. I appreciate Ebiere and Ogaga particularly for their financial sacrifices throughout my program, Priye and Opuye for always being available as great siblings throughout my study in a distant land, and Mummy for being a great caretaker and rock. Your selflessness has helped me go through my program with more stability, and I am indeed grateful. I am also indebted to my friend turned brother Yemi, for taking the progress of my work personally.

I am thankful to my professors for all the knowledge instilled in me, and all the experience shared. Classes by Professor Hafez, Professor Ben Shaw, Professor Robinson and Professor Vinod particularly piqued my interest in thinking about research application of what I have learned.

Finally, I am grateful to Professor Erickson and Professor Jenkins for taking their time to read through my work and for giving me valuable feedback.

NOMENCLATURE

A_c	Cross sectional area of pin (m^2)
C_p	Specific heat capacity $(KJ\ /kg\cdot\ k)$
D_h	Hydraulic diameter of the pin (m)
D_{LC_min}	Hydraulic diameter calculated based on the minimum flow area (m)
G_{solar}	Solar insolation (W/m^2)
S_l	Longitudinal pitch (m)
S_t	Transverse pitch (m)
T_a	Ambient temperature (K)
T_{dish}	Parabolic dish concentrating surface temperature (K)
T_{in}	Receiver inlet fluid temperature (K)
T_{out}	Receiver outlet fluid temperature (K)
T_{so}	Receiver surface temperature (K)
V_{max}	Maximum velocity across pin fin array $(m\ /s)$
W_{pin}	Width of pin in the receiver (m)
k_{bulk}	Fluid conductivity $(W\ /mK)$
$\dot{m}$	Mass flow rate $(kg\ /s)$
ΔP	Pressure drop (Pa)
h	Enthalpy at a control volume of the receiver (KJ)
H_{pin}	Height of pin in the receiver (m)
IC	Heat flux (W/cm^2)
N	Number of pins in a control volume
Nu	Nusselt number
P	Perimeter of pin fin (m)
Pr	Prandtl number
Re_{LC_min}	Reynolds number based on D_{LC_min}
dq_{conv}	Convection heat loss (W)
dq_{fluid}	absorbed heat by the working fluid (W)
dq_{in}	heat flux into the receiver (W)
dq_{rad}	Radiation heat loss (W)

dR_t	Heat transfer resistance to fluid heat absorption $(k\ /W)$
dx	increment in the x direction (m)
dy	increment in the y direction (m)
f	Friction factor
i	index in the horizontal direction
j	index in the vertical direction
k	Conductivity of Haynes 282 (W/mK)
m	Fin efficiency parameter
w	Width

GREEK SYMBOLS

η_0	overall fin efficiency
η_f	pin efficiency
η_{rec}	Receiver efficiency
η_{th}	Thermal efficiency
ρ_λ	Reflectivity coefficient
α	Absorptivity coefficient
ε_λ	Emissivity coefficient
μ	Dynamic viscosity $(Pa.s)$
ρ	Density $(kg\ /m^3)$
σ	Stefan-Boltzmann constant $(W\ /m^2K^4\ )$.

SUBSCRIPTS

f	fin area
sCO_2	supercritical carbon dioxide
t	total surface area
λ	Function of wavelength

TABLE OF CONTENTS

ABSTRACT ii
ACKNOWLEDGEMENTS iv
NOMENCLATURE v
LIST OF FIGURES ix
LIST OF TABLES xii
CHAPTER 1 INTRODUCTION 1
CSP Central Receiver Technologies 3
CSP Potential Pathways 4
MSTR Microchannel Receiver Development 11
Research Objectives 16
CHAPTER 2 UNIT CELL NUMERICAL MODEL DEVELOPMENT 18
Grid Discretization 18
Modelling Approach 21
Numerical procedure 26
CHAPTER 3 UNIT CELL RECEIVER RESULTS 30
Additively Manufactured Vs Microlaminated Receiver (AM^2PAR Vs µLPAR) Unitcell Lengths 32
AM^2PAR vs µLPAR Pin Array Length Parametric Studies 33
AM^2PAR vs µLPAR Receivers - Local Variation Comparison At Maximum Pin Array Lengths 38
AM^2PAR vs µLPAR Receivers- Variation of Incident Flux 40
CHAPTER 4 CENTRAL RECEIVER DESIGN AND MODELLING 44
Heliostat Field Layout and Aiming Strategies On Central Receivers 44
Solar Flux Mapping on Central Receivers 46
Power Generation Considerations 48
Field Development and Optimization with SolarPILOT 51
SolarPILOT Simulation Results 55
Unit Cell And Module Integration 63
Numerical Modelling Parameters 65
CHAPTER 5 CENTRAL RECEIVER SIMULATION RESULTS AND DISCUSSION 68
Solar Flux Impact on the Surface Temperature and Efficiency (Spatial and Temporal) 68
Fluid and surface temperature distribution at solar noon 72
Analysis of the Impact Of Non-Uniform Flux Distribution on the AM^2PAR Central Receiver 74

Design For Thermal Optimization of the Receiver: Novel Design Concepts 76
Variable Pin vs Uniform Pin vs Ideal Case Over a Summer Day 84
Operational Modification for Improved Creep Life 88
CHAPTER 6 ANALYSIS MODEL FOR EXPERIMENTAL STUDY OF THE MICRO-PIN-ARRAY RECEIVER 95
Analysis Code for Flux Estimation in a Parabolic Dish 95
Uncertainty Analysis 98
Uncertainty In The Nodal Temperature 98
Uncertainty In The Surface Heat Flux 99
Uncertainty In Fluid Heat Absorbed 100
Uncertainty In Convection 100
Uncertainty In Radiation 101
Uncertainty In Receiver And Thermal Efficiency 102
Uncertainty Estimates for Representative Experimental Data 104
CHAPTER 7 CONCLUSIONS AND RECOMMENDATIONS 106
REFERENCES 109
APPENDIX 112
NUMERICAL PROGRAM FOR COMPUTING THE MPAR RECEIVER THERMAL AND HYDRAULIC PARAMETERS FOR A CONSTRAINED INLET AND OUTLET TEMPERATURE 112
NUMERICAL CODE FOR OBTAINING THE RECEIVER PERFORMANCE PARAMETERS (TEMPERATURES, EFFICIENCIES AND PRESSURE DROP) FOR A GIVEN HEAT FLUX DISTRIBUTION 120
NUMERICAL CODE FOR CONDUCTING UNCERTAINTY ANALYSIS OF A MPAR RECEIVER MODULE'S PERFORMANCE PARAMETERS 133

LIST OF FIGURES

Figure 1: Concentrated solar power technologies (source: Mehos et al [1[) 3
Figure 2: Crescent Dunes Solar Energy Project in Tonopah, Nevada (source: SolarReserve.com) 4
Figure 3: Schematics of three pathways to solar-sCO2 power plant technology. A. High-temperature molten salt receiver pathway. B. solid particle receiver pathway and c. gas receiver pathway. Adapted from Narayanan et al. [2]. 6
Figure 4: Receiver scheme for the eight flow pattern configurations suggested by Wagner [7] 7
Figure 5: Cavity receiver conceptual design with key design parameters highlighted. Source: Wagner [12] 9
Figure 6: Example of Brayton Energy internal supported sCO_2 receiver unit cell. (Source: Mehos et al. [1]) 10
Figure 7: Representation of the microchannel receiver in an open central power tower configuration. Source: Narayanan et al. [2] 12
Figure 8: a) Exploded view of a 2x2cm micro-pin-array receiver (MPAR), referred to as MSTR by Narayanan et al. [13] and b) 8cm x 8cm scaled up version of the MPAR showing the inlet header, the distribution headers, the unit cells (flow microstructures) and the outlet header .source: Narayanan et al. [13]. 13
Figure 9: Flow network in a micro-pin-array receiver (MPAR) with 3 unit cells, 4 inlet headers and 3 outlet headers. 18
Figure 10: (a) 2-D discretization of the unit cell into control volumes (b) thermal resistance model from [13] which couples with an energy balance equation that solves for each of the control volumes. 20
Figure 11: comparison of the sCO_2 correlation by Rasouli et al. with results from pressure drop experiments with air. 25
Figure 12: (a) schematic showing the control volume 2 dimensional discretization from inlet to exit (b) flow chart describing the procedure of calculating the thermal and hydraulic parameters of a flow given a fixed inlet and outlet temperature. 29
Figure 13: Top view (left) and bottom view(right) of an MPAR module with three unit cells (6 pin arrays). 31
Figure 14: This model shows a uniform flux applied on a single pin array. A uniform flux all through, implies that there is no vertical variation in fluid and thermophysical properties, but there is variation along the flow path (horizontally) as the fluid heats up. Hence such a model can be simplified into a one-dimensional analysis. An array of lengths (ranging from 2.5cm to 30cm) are simulated to determine the relationship between the length of a unit cell and the associated pressure drop for a given outlet temperature constraint. 33
Figure 15: Pressure drop vs unit cell length for receiver unit cell lengths ranging from 2.5cm to 30cm. 34
Figure 16: comparison of the thermal performance of additively manufactured and microlaminated receiver unit cells. 36
Figure 17: Comparison of the local surface and bulk fluid temperatures (primary ordinate) and heat transfer coefficient (secondary ordinate) of μLMPAR and AM^2PAR pin arrays as a function of non-dimensional length. 38

Figure 18: plot comparing internal flow thermal resistance and overall fin efficiency of the microlaminated (3.3cm scaled to 1.0) and additively manufactured (16.6cm scaled to 1.0) unit cell receivers. 39
Figure 19: Comparison of the AM^{2}PAR (unit cell length = 16.6cm) and µLPAR (unit cell length = 3.3cm) receivers' thermal performance over a range of heat flux from 20W/cm^2 to 120W/cm^2 for flow temperature increase from 550 to 720°C. 40
Figure 20: plot comparing the pin resistances and the pin efficiencies of the µLPAR and AM^{2}PAR receivers over a range of simulated heat fluxes, for a target inlet temperature of 550°C and a constrained outlet temperature of 720°C. 42
Figure 21: Plot of the convective heat transfer coefficient and the heat losses in an additively manufactured micro-pin-array receiver for a fixed temperature increase of 550 to 720°C. 42
Figure 22: equatorial aiming on a receiver (source: [22]) 45
Figure 23: non equatorial aiming on receiver (source: [22]) 45
Figure 24: Non uniform flux profile on a central receiver (source: [26]) 47
Figure 25: SolarPILOT Heliostat layout after field optimization for Daggett-Barstow field simulation, with the color codes displaying the efficiencies of the individual heliostats. 54
Figure 26: SolarPILOT flux maps for several times (sun positions) in the simulated day. 63
Figure 27: Sketch of the unit cell pin arrays combined to form a ~1m long by 0.2m wide module. 64
Figure 28: Flow chart showing the numerical sequence of solving the micro-pin array external receiver with a target output temperature of 720°C. 67
Figure 29: heat maps of solar flux (left column) maximum module surface temperatures (middle) and module efficiency (right column) between 8 hours and 18hours. 71
Figure 30: map of mass flow of sCO_2 in each grid row of the unit cell 72
Figure 31: Surface temperature distribution over the receiver at solar noon on a hot summer day. 73
Figure 32: Map of fluid outlet temperatures from each of the 1250 modules simulated ranging from 575^{0}C to 800°C for solar noon for a bulk fluid outlet temperature of 720°C. 73
Figure 33: plot of the maximum surface temperature and thermal efficiency of the receiver in the ideal and real scenario (UPH_AM2PAR) as a function of hour of a typical day in July. 75
Figure 34: comparison of the pressure drop and the total mass flow rate in the ideal and the real case (UPH_AM^{2}PAR) receiver 76
Figure 35: plot to show the pin height distribution over the different modules of the receiver as a function of their vertical position and flux in the receiver. 78
Figure 36: Maps of solar flux (left column) maximum module surface temperatures (middle) and module efficiency (right column) between 8 hours and 18hours on the VPH-AM^{2}PAR between 8hrs and 18hhours. 79
Figure 37: Map of fluid outlet temperatures from each of the 1250 modules simulated ranging from 575^{0}C to 800°C for solar noon for an average fluid outlet temperature of 720°C at noon time. 80
Figure 38: Surface temperature distribution over the receiver at solar noon on a hot summer day for the variable pin receiver. 81
Figure 39: Mass flow distribution in each grid row of the variable height receiver at solar noon. 82
Figure 40: Side by side comparison of the VPH-AM^{2}PAR receiver and the UPH-AM^{2}PAR receiver at solar noon. 82
Figure 41: plot of the fluid thermal power of the VPH-AM2PAR vs UPH-AM2PAR given a fixed inlet fluid temperature of 550°C and a constrained outlet temperature of 720°C. 83

Figure 42: plots of the thermal efficiencies and the maximum surface temperatures of the different receiver concepts and the ideal case at different times of a hot summer day in Daggett-Barstow. 85
Figure 43: plot of the hydraulic parameters of the uniform height, variable height receiver and the ideal case for a target bulk outlet temperature of 720°C. 85
Figure 44: Distribution of module maximum temperatures of the UPH-AM^{2}PAR and the VPH-AM^{2}PAR receivers. 87
Figure 45: Flow chart showing the algorithmic sequence for obtaining the solution of a maximum receiver surface temperature less than 770°C. 89
Figure 46: Thermal behavior of the variable pin height receiver comparing the fixed outlet fluid temperature condition and the fixed maximum surface temperature condition of 770°C. 90
Figure 47: Comparison of the hydraulic parameters (mass flow and pressure drop) in the variable pin fixed fluid temperature (VPH-AM^{2}PAR-FT) and variable pin fixed surface temperature (VPH-AM^{2}PAR--ST) modes of receiver control. 91
Figure 48: Fluid thermal power for the various concepts of the receiver. UPH-AM^{2}PAR and the VPH_AM^{2}PAR_FT have a constrained outlet fluid temperature of 720°C at all hours, whilst the VPH_AM^{2}PAR_ST has a constrained surface temperature of 770°C at all hours. 92
Figure 49: Distribution of the maximum surface temperatures in the VPH-AM^{2}PAR-FT (Variable pin fixed outlet fluid temperature = 720°C) and the VPH-AM^{2}PAR--ST (variable pin fixed maximum surface temperature of 770°C) modes of receiver operation. 94
Figure 50: Two-axis tracking 7-m parabolic solar dish at the STEEL lab (UC Davis) in operation during an on-sun experiment with a prototype 8 cm x 8 cm micro-pin-array receiver. 96
Figure 51: control volume discretization of the AM^{2}PAR receiver in 2 dimensions. 97

LIST OF TABLES

Table 1:Pin dimensions of micro-pin array receivers based on manufactured prototypes of micro-pin fin arrays used in prior and concurrent research studies by our group. 32
Table 2: TMY data for Daggett-Barstow during a hot summer day in July (source: SolarPILOT software). 52
Table 3: Receiver geometry input parameters. 53
Table 4: Flux simulation results summary for a solar noon at DNI value 982W/m^2 55
Table 5: Receiver structural and fluid operating parameters for numerical simulation 68
Table 6: Representative measurement uncertainties used in error propagation. 104
Table 7: Results of the error propagation with a dummy surface temperature map. 105

CHAPTER 1
INTRODUCTION

Fossil fuels have been the dominant mix in the world's energy portfolio for a long time. Renewable energy from the sun has gained traction in an effort to reduce carbon emissions and create a more sustainable world. The most prevalent method of conversion of solar energy to electricity is through photovoltaic (PV) cells. As the world moves towards enriching its renewable energy portfolio, the popularity of PV cells have increased. Technological advances have made PV cells cheaper and more efficient. The main challenge with integration of renewables is the mismatch between generation and demand, which requires energy storage. Energy storage for PV systems is predominantly via batteries, which are more expensive compared to other forms of renewable energy storage. The lithium ion batteries require reliance on mining lithium carbonate which is a water and labor intensive operation, besides the unsustainable environmental impact. Concentrated solar power is an alternate technology to PV technology that concentrates heat directly from the sun through reflecting surfaces onto a central receiver. It offers the advantage of variability of energy generation associated with the intermittency of the solar resource, reliable system capacity and dispatchable high-value energy, which photovoltaics and wind energy are unable to provide. A CSP plant is also capable of ramping up rapidly, thus providing multiple ancillary services such as regulation and spinning reserves [1]. It uses traditional materials in construction and for storage. CSPs make use of central receivers which absorb heat from the sun through a working fluid. The heat absorbed during the day can be stored at night in a thermal tank, which could be used to supply heat to steam, and power a turbine.

CSP systems are generally classified by how the various systems collect solar energy. The four main systems, as shown in Figure 1, include the linear Fresnel, central receiver (power tower), parabolic dish, and the parabolic trough systems.

Linear Fresnel: This is a solar collector operating in a linear system such that a long array of long, narrow, flat or slightly curved mirrors reflects the sun rays onto a fixed linear receiver mounted over a tower above and along the reflectors [5]. The advantages of the linear Fresnel are its attractiveness as a low-cost option for CSP when compared to other technologies, and its use of stationary receiver without rotating parts—causing lower construction and operating costs. Drawbacks of the linear Fresnel are that optical losses are very high as a result of shading, thus causing the mirrors to be spaced in a greater area. Also, the linear Fresnel does not produce very high temperatures compared to the other competing systems.

Parabolic trough systems: This is a linear system solar collector which has a receiver installed along the focal line of a parabolic trough concentrator. The parabolic trough system tends to have higher optical efficiency than the linear Fresnel systems because the mirrors can track the sun and because of the curvature of the mirrors. A limitation of the parabolic trough system is that it doesn't produce fluid temperatures as high some other concentrating solar power technologies, thus causing lower efficiency in electricity production.

Parabolic dish: This system, as the name implies, comprises of a parabolic reflector which reflects the solar insulation on its focal point, where a central receiver is installed. The parabolic dish solar concentrator tracking system can track the sun, concentrate a relatively high heat flux on the receiver—compared to the other concentrated solar power systems, and they produce very high temperatures capable of being used in mini power generation and process heating applications. The downside of the parabolic dish system however is in that they are limited to power generation in a very small scale because of the size limitation of each dish.

Central Solar tower: The central solar tower system consists of reflecting mirrors (heliostats) placed around an elevated central receiver, at heights up to 90m. With several heliostats concentrating solar

irradiation on the receiver, the central tower receiver can concentrate very high fluxes on the receiver, with the flux concentration limited by factors such as the material temperature limits. Central towers are capable of producing very high fluid temperatures and generating comparatively, very large amounts of electrical energy. Central tower plants however need high temperature limit components such as receiver, tubing and heat exchangers and design to contain the very high temperatures that are realizable in the system.

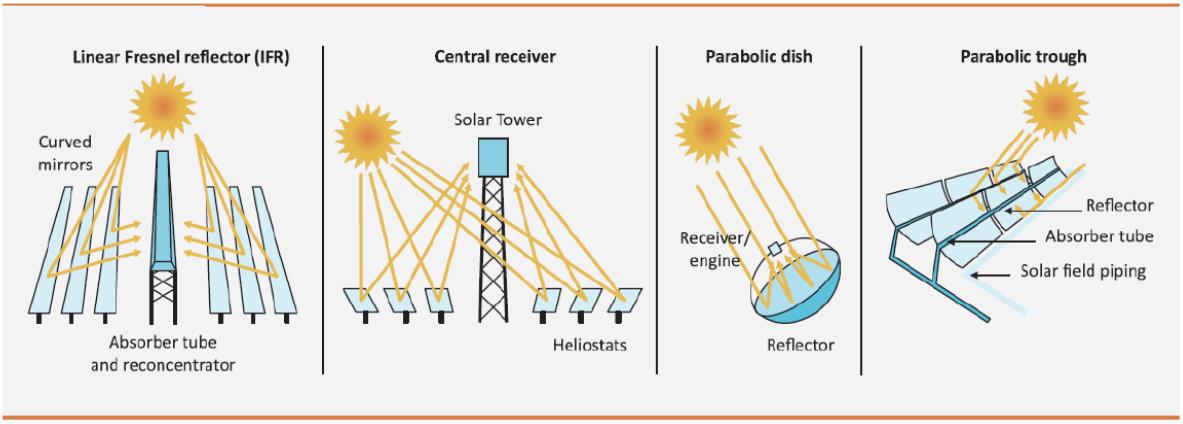

Figure 1: Concentrated solar power technologies (source: Mehos et al [1[)

CSP Central Receiver Technologies

Power-tower CSP systems are more advantageous when compared to the parabolic trough and linear Fresnel plants because they can achieve higher temperatures. In a power tower system, several reflecting mirrors known as heliostats (Figure 2) are arranged about a central tower, over 90m high.

Figure 2: Crescent Dunes Solar Energy Project in Tonopah, Nevada (source: SolarReserve.com)

The central power tower holds the central receiver. Direct normal irradiation incident on the mirrors is reflected and concentrated on the central receiver at about a thousand times the intensity of the incident rays. The receiver serves as a heat sink: a heat transfer fluid (HTF) flowing through the receiver captures the heat and increases in temperature. This high energy fluid is then used to power a turbine directly or by exchanging heat with another fluid. Alternatively, the fluid can be stored in storage tanks (thermal energy storage) for up to 10 hours or more depending upon design and the desired temperature of the fluid on demand as lower temperature fluid leads to lower cycle efficiency [6]. Presently, common central receiver systems utilize either pressurized water or nitrate molten salt as the heat transfer fluid.

CSP Potential Pathways

The US Department of Energy CSP Solar Energy Technologies Office (SETO) defined three potential pathways for the next generation of CSP plants based on the form of the thermal carrier in the receiver: molten salt, particle or gaseous [1]. The SETO Program is developed with aggressive targets to achieve

lower component costs and higher system efficiencies toward making CSP development and implementation cost competitive with other existing renewable energy infrastructure. Prior analysis by the DOE had selected the supercritical carbon di-oxide (sCO_2) Brayton cycle as the best-fit power cycle for increasing CSP system thermal-to-electric conversion efficiency [1]. The Brayton cycle with sCO_2 offers comparable advantages to the steam Rankine cycle because the system is lighter and less complex modularly as a result of the higher density of sCO_2.

All the potential pathways have technological advantages and concerns. A brief review of the pathways and research done on them is presented in this section.

a. Molten-Salt Receiver Pathway:

In the molten salt receiver pathway, pre-heated molten salt is circulated through a central receiver, absorbing heat concentrated from the heliostat field (Figure 3a). The heated salt exchanges thermal energy with the power cycle fluid in a heat exchanger, and the cold fluid is afterwards discharged to a cold tank for re-circulation. The molten-salt technology using nitrate salts in tubular external receivers is the current state-off-the-art CSP technology and operates at hot-salt temperatures of approximately $565°C$. Known commercial molten salt power towers which use sodium/potassium nitrate (solar salt) as the heat transfer fluid and thermal energy storage (TES) medium include: Gemasolar (Spain ,19MW_e, 15 hours TES) and Crescent Dunes (Tonopah, Nevada, 110MW_e, 10 hours TES) [1]. Such plants however fall short of the SETO efficiency goals, which require that technologies work at temperatures between $650°C$ and $750°C$.

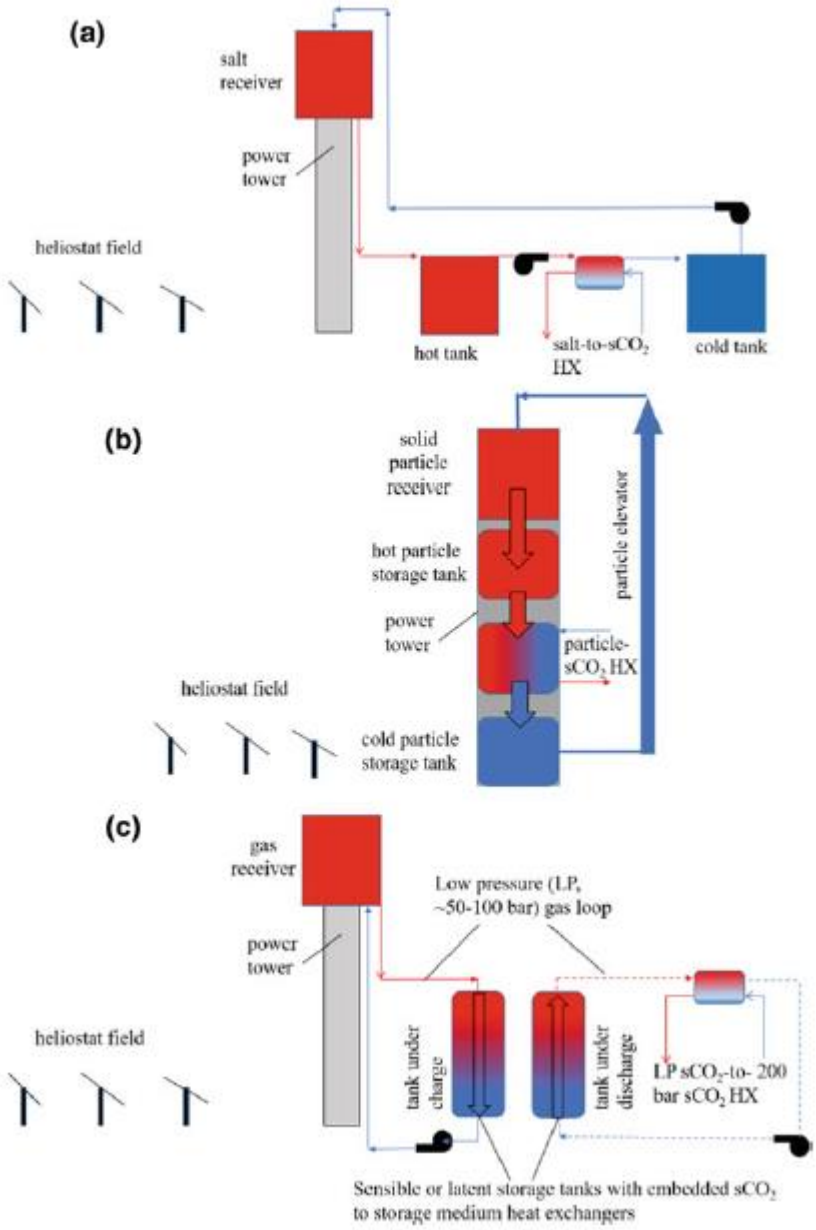

Figure 3: Schematics of three pathways to solar-sCO2 power plant technology. A. High-temperature molten salt receiver pathway. B. solid particle receiver pathway and c. gas receiver pathway. Adapted from Narayanan et al. [2].

The solar salt technology is a very mature technology with more recent work being done to optimize flow patterns and to propose better thermal management. Wagner [7] in his numerical study of molten-salt

utility scale receivers proposed eight different receiver flow-path configurations with divided flow path configurations (Figure 4, [1-4]) and single flow path configurations (Figure 4, [5-8]). Rodriguez-Sanchez et al. [8] further analyzed the external molten salt receiver during its annual operation, including crossovers to the single and multiple flow paths suggested by Wagner [7]. The authors conclude that the most efficient and reliable flow path in a molten-salt external receiver is one with two modes of operation: a crossover just before the midpoint of the path when the solar flux is low or no crossover when the DNI (Direct Normal Irradiance) is high, and the peak flux is still asymmetric.

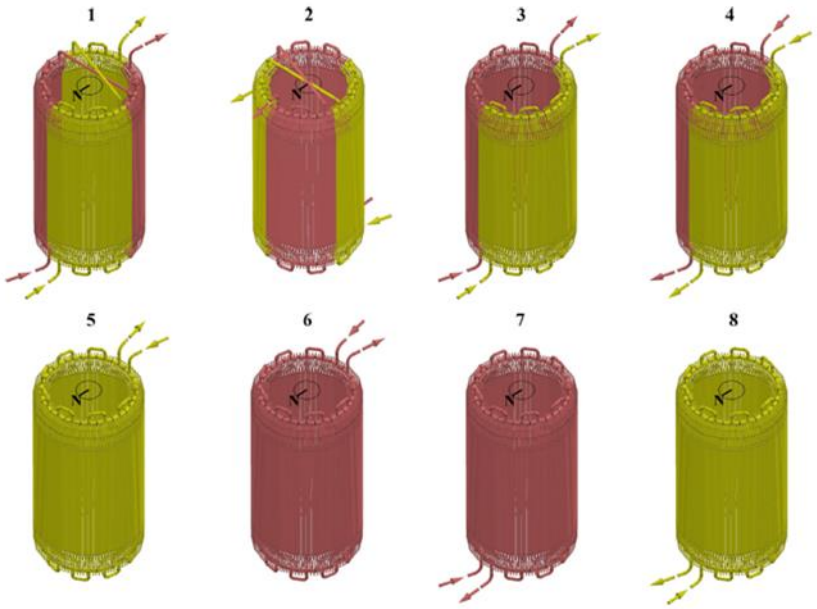

Figure 4: Receiver scheme for the eight flow pattern configurations suggested by Wagner [7]

Research and development on higher temperature salts are underway. In the development of molten salt systems, the major identified technological gaps and challenges according to the DOE SETO report [9] include: salt chemistry, materials selection, pumps, valves, heat exchangers, plant sensors, thermal energy storage systems and component test facilities [9]. Wait [10] developed a Haynes 230-alloy (a nickel-chronium-tungsten-molybdenum alloy) receiver capable of directly storing sensible heat in molten salt HTF at 720°C, using a thin-walled rectangular flow channels made of alpha-silicon carbide. This design

incorporates an oxidation-resistant nano-particle solar absorbing coating which could operate at 800°C, hence making it corrosion resistant at that temperature, with a thermal efficiency of 92.7%.

b. Particle Receiver Pathway

The particle receiver design uses solid particles that are heated, unlike the conventional receivers which employ fluid flowing through tubular receivers (Figure 3b). The solid particles in the receiver are heated either directly or indirectly. The heated particles may afterward be stored in an insulated tank and used to heat a secondary working fluid for the power cycle. In this configuration, the flux limitations associated with tubular central receivers, such as high stresses resulting from the temperature and pressure of the containment fluid, are significantly relaxed since the solar energy can be directly absorbed in the particles. A number of different particle heating methods exist including direct heating of the particles in free-falling, obstructed, centrifugal, and fluidized configurations, as well as indirect heating of the particles in enclosed configurations such as gravity-driven flow through tubes and fluidized particle flow in tubes and other enclosed receiver designs [11]. Wagner [12] developed a receiver that can heat fluid from 450˚C to 650˚C in a double cavity receiver design. This receiver configuration situates absorber panels within an external surrounding cavity to form an array of unit cells (Figure 5). The arrangement of horizontal panels into vertical stacks thus limits unrestricted flow along vertically-oriented hot surfaces, thermally isolates the upper unit cells from the surrounding environment and reduces natural convective loss from the proposed receiver configuration. Gaps and challenges associated with the particle power-tower technology include: particle loss, receiver and feed bin challenges, particle storage, particle heat exchanger, particle lift and conveyance [1].

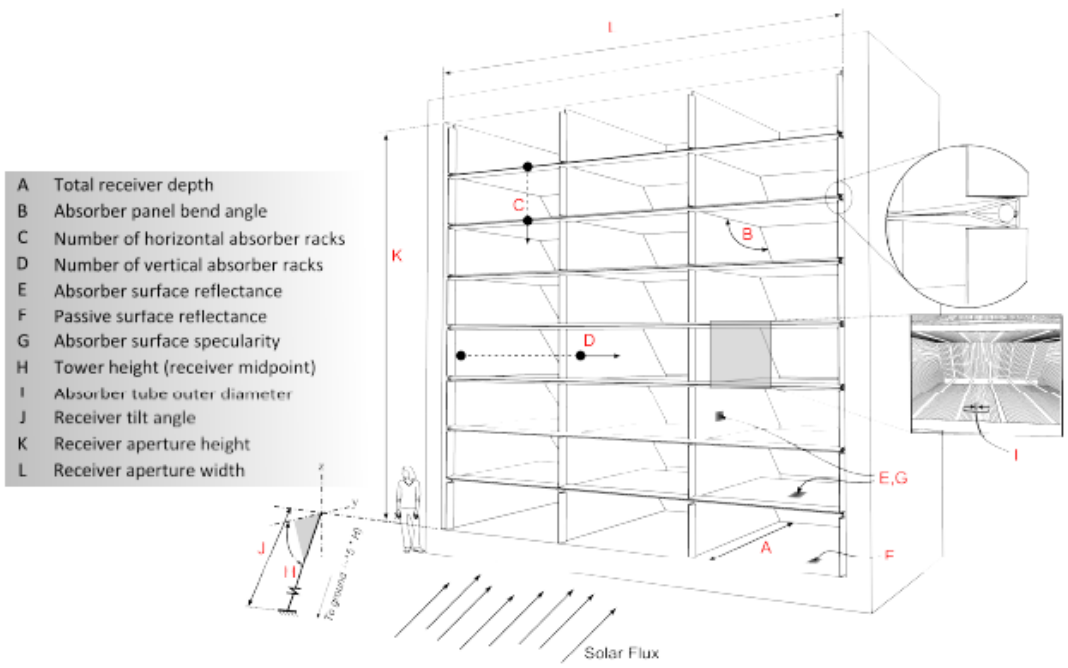

Figure 5: Cavity receiver conceptual design with key design parameters highlighted. Source: Wagner [12]

c. Gas Receiver Pathway

The gas receiver pathway consists of a stable heat transfer fluid, in a closed loop, circulated through the receiver with relatively small flow channels (small-diameter tubes, microchannels or other geometries) and exchanging transferring energy to and from the thermal energy storage (Figure 3c). The fluid in the receiver is heated to temperatures sufficient to generate the target of 700°C supercritical CO_2 after heat exchange into the power cycle. Potential gas-phase (GP) heat transfer fluids include sCO_2, helium, argon, or mixed GP fluid. The hot fluid can be stored in thermal energy storage, which decouples the thermal energy collection through the receiver from the power generation system. Significant advantages of the gas-phase heat system include stability over a broad temperature range, compatibility with existing high-efficiency receiver designs, primary heat-exchanger simplicity (gas-to-sCO_2 unit) and potential for decoupling the thermal storage technology from the fluid composition, thereby providing an opportunity for advanced energy storage concepts [1].

Several research activities have taken place in the development of gas receiver pathway technology. Brayton Energy developed an internal finned-plate receiver design as part of the US DOE SunShot initiative that provides high heat transfer to the gas with structural integrity and tensile strength for high pressures, by leveraging its experience with plate-fine-style recuperating heat exchangers for gas-turbine applications [1]. Brayton Energy's network of densely packed fins (Figure 6) serves to provide both structural support to the cell—thus allowing the shell wall thickness to be thin—and they enhance the internal heat transfer from the external surface to the internal flow of sCO_2.

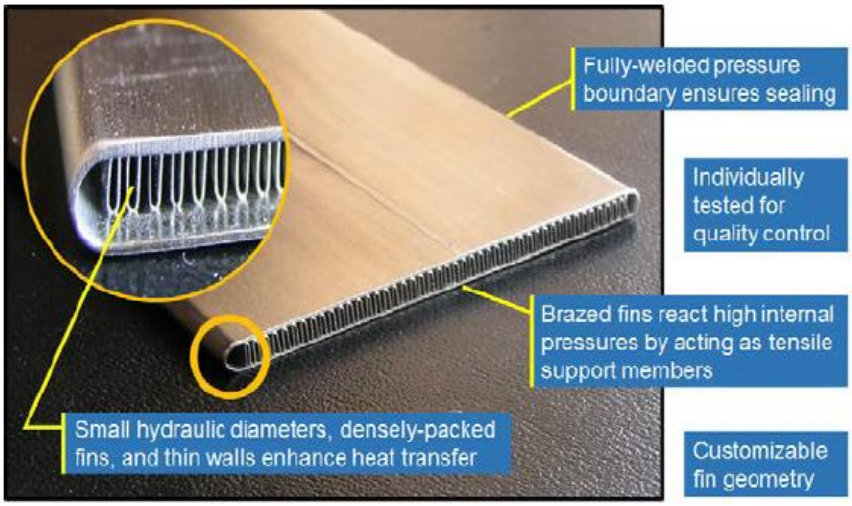

Figure 6: Example of Brayton Energy internal supported sCO_2 receiver unit cell. (Source: Mehos et al. [1])

Mehos et al. [1] however identify that the system also comes with identified important challenges which include:

1. Inferior heat-transfer characteristics of gaseous working fluids, which can cause concerns about receiver material durability and transient response.
2. Selection of appropriate pressure and temperature targets to balance the containment material performance. For example, the stress resistance of high-temperature alloys is significantly

reduced at material temperatures above 700°C, and these factor into the maximum receiver fluid outlet temperature.

3. Flow-path complexity because the header and distributor design need to tailor the mass flow path based on the expected receiver flux to keep the outlet flow stream temperature within operation limits.

MSTR Microchannel Receiver Development

Recent interest in sCO_2 cycles has brought about an interest in the use of microchannel receivers, scaled in a numbered-up approach.(Figure 7). In one design, the receiver consists of several flat receiver modules envisioned to be arranged atop a central receiver. In an open configuration, the arrangement could be cylindrical). Each module consists of unit cells which contain microscale flow features; these unit cells are connected in parallel. The modules have fluidic headers to route hot and cold streams of sCO_2 into the unit cells. In the current way of fabricating micro-pin-array receivers (MPAR), laminated microchannel devices (μLPAR) are used, in which the capacity of a unit operation is increased by adding more laminae. The logic behind this approach is that by arranging modules of the receiver in parallel, the understanding of the performance of each module as a function of incident flux would lead to the prediction of the performance of a complete commercial-scale solar receiver. The advantage of such a configuration is that the flow, being divided into different parallel paths results in lower pressure drop because of the reduced velocity in each path and shorter flow length. The micro-pin-array receiver (MPAR) is fabricated from the nickel superalloy Haynes 230 using a microlamination approach where the pin array is chemically etched in a sheet and diffusion bonded to a flux plate (Figure 8a).

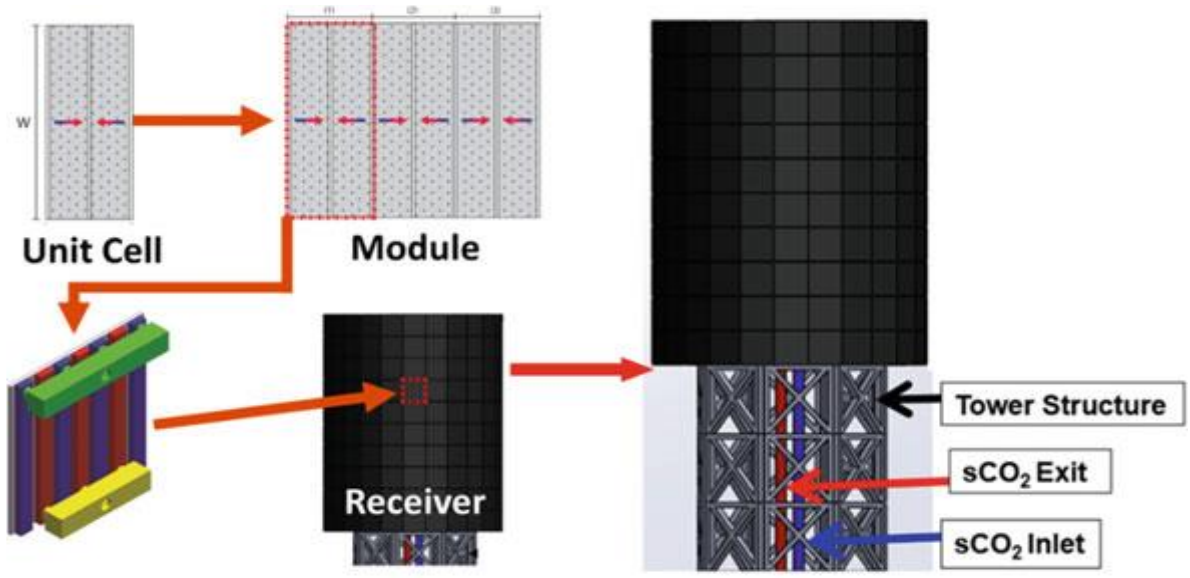

Figure 7: Representation of the microchannel receiver in an open central power tower configuration. Source: Narayanan et al. [2]

Fluidic headers are affixed to the back side of the bonded plates to form a module. A limitation of the microlamination technique is that the etch depth during chemical etching is low, thus causing the pin height dimension, and thus channel height to be limited. This limitation leads to a constraint in the unit cell length to allow for functioning within the pressure drop limit (typically 2% of line pressure). Laboratory scale experiments were performed by L'Estrange et al. [3] using small 2cm x 2 cm unit-cell devices containing arrays of micro-pins Figure 8(a). The authors used a laboratory concentrator (consisting of a single 6kw xenon arc lamp) located at the focal point of a truncated ellipsoidal reflector.

(a)

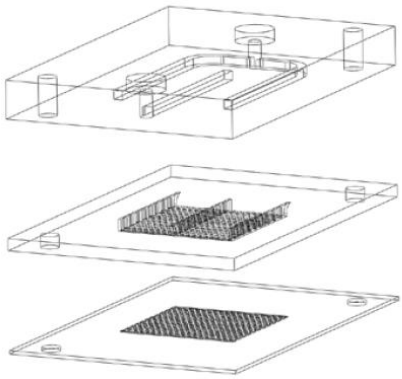

(b)

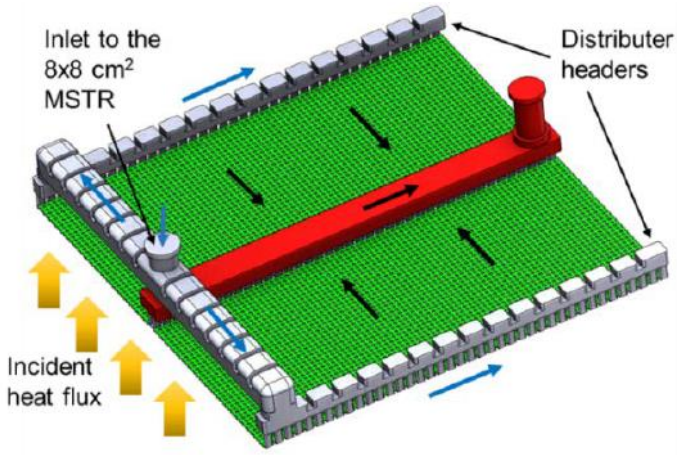

Figure 8: a) Exploded view of a 2x2cm micro-pin-array receiver (MPAR), referred to as MSTR by Narayanan et al. [13] and b) 8cm x 8cm scaled up version of the MPAR showing the inlet header, the distribution headers, the unit cells (flow microstructures) and the outlet header .source: Narayanan et al. [13].

The results of this research demonstrated the potential of such devices to absorb heat fluxes greater than 100W/cm^2 within operating limits of temperature and pressure, and at high thermal efficiency values of greater than 90%. Furthermore, Zada et al., [4] conducted a numerical study to demonstrate the feasibility of numbering up microscale receivers for megawatt applications. In this system, the authors postulated the receiver system as consisting of the lowest level architecture: unit cell which consists of staggered array of micro-pins with two inlet headers and one central outlet header, the module which is defined as a multiple of unit cells connected in parallel, and the external receiver which is made up of

multiple modules stacked in a cylindrical patter. In the modelling, a pressure drop constraint was used to solve the flow for heating the heat transfer fluid from 550°C to 650°C at an incident flux of 110W/cm^2. The authors assumed an average surface temperature for each unit cell, and the authors assumed a uniform flux in the vertical direction of the receiver. The results of this study, which is based on flux circumferential variation results from DELSOL simulations in Barstow California, show that the efficiency of the system had a value of 88% in the southern hemisphere (as the southern hemisphere mirrors receive the least solar irradiation) and 91% thermal efficiency in the northern hemisphere (the northern hemisphere receives the maximum view factor of the sun at the highest DNI at solar noon).

More simulation studies were conducted by Hyder and Fronk [14], to investigate further the thermal and hydraulic performance of multiple parallel micro-pin arrays for concentrated solar thermal applications with sCO_2. The authors developed a hydraulic model which constrained the flow using conservation of mass, and equality of pressure drop from inlet to outlet. The author's objective was to determine the maximum allowable unit cell size and header dimension, and to study the influence of varying flux on flow distribution. The results of this research showed the ability to heat sCO_2 from 550°C to 720°C at an incident flux of 140W/cm^2 with less than 4bars of pressure drop. In this study, the unit cell length based on the receiver parameters is given as 4cm. Narayanan et al. [15] performed on-sun characterization of a microchannel sCO_2 receiver in a parabolic dish set up. The authors tested an 8cm x 8cm microchannel sCO_2 receiver, with an inlet fluid temperature of 130°C. For incident flux ranging from 8 to 80W/cm^2, receiver and thermal efficiencies in excess of 91% and 96% respectively were realized.

Receiver efficiency is defined as

$$\eta_{rec} = \frac{dq_{fluid}}{dq_{incident}} \tag{1.1}$$

Where dq_{fluid} is the power absorbed by the receiver heat transfer fluid, and $dq_{incident}$ is the power incident on the receiver. The thermal efficiency is defined as

$$\eta_{th} = \frac{dq_{fluid}}{\alpha_\lambda \cdot dq_{incidient}} \quad (1.2)$$

Where α_λ is the absorptivity coefficient of the receiver.

Several challenges exist, beyond pressure drop limitations, in the development and scaling up of micro-pin array receiver technology. Etching of nickel based alloys has significant environmental impact, thus limiting the available domestic vendors engaging in the manufacturing process. Furthermore, in the current way of manufacturing the MPAR with Haynes 230, creep, fatigue or thermal stresses are not considered thus making the material's viability for use in an sCO_2 receiver questionable. In addition, McNeff et al. [16] have highlighted failure modes in the design and fabrication of a prototype µLPAR. The authors categorized these failures in detail into a) failure due to the TLP bond re-liquefying during the high temperature vacuum brazing and post-processing, b) failure due to manufacturing defects where the cross section and bonding area are reduced, as well as carbon contamination attributed to the graphite hole punching tool, and c) failure related to the inability of the receiver design to accommodate manufacturing defects related to the TLP bonding and wire EDM.

In researching and discussing the feasibility of a micro-pin-array receiver for use in a concentrated solar power central tower, it is important to know that none of the aforementioned studies addressed the following factors:

1. Local variation of properties of fluid within each pin array and across the entire receiver.
2. Impact of vertical variation of the flux on the receiver performance.
3. Impact of temporal change in the sun position on the receiver performance for an optimized solar field.

Research Objectives

In work to date, the research on micro-pin array receivers (MPAR) for implementation in a CSP field has been scant. As highlighted earlier, due to the limitation in etch depth during chemical etching, the micro-pin-array unit cell has a relatively small height which results in the realizable unit cell length being constrained by the allowable pressure drop (2% of line pressure). For a full scale receiver, a short length unit cell will mean a more complicated headering system, as more unit cells will be needed to make up a module.

As a result, the first objective of this study was to explore ways in which the length of the unit cell can be increased to reduce the complexity of the headering system using additively manufactured micro-pin array receiver (AM^2PAR). This study draws on knowledge generated by the existing micro-pin-array heat exchangers in a joint project between UC Davis and Carnegie Mellon University, to assess whether an AM^2PAR can incorporate longer unit cells for the same pressure drop as a microlaminated design, thus reducing the complexity of the headering system [personal communication]. In addition to unit cell length increase, employing an additive manufacturing approach lends to monolithic design of pin array and headers, eliminating issues with brazing and bonding which are encountered in a microlamination design.

Secondly, the previous research works on the micro-pin array receiver have not explored the combined effect of the time variation of heat flux during a day, and the spatial variation of flux over the entire receiver surface on the performance and implementation of the micro-pin array receiver. This research conducts a case study on a specific field during a summer day, to understand the impacts of spatial and temporal non-uniformity in flux on a uniformly built receiver using a quasi-steady state model.

Receivers are built in view of target exit temperatures of fluids that will serve as inlet fluid to the power cycle. Several factors, such as the incident flux on the receiver and the material operating limits, inform the maximum allowable temperature from the receiver. This study explores the possibility of achieving a

target fluid outlet temperature of 720°C, and the implications of the outlet temperature on the overall performance and durability of the central receiver system.

Lastly, an analysis code is developed to obtain the efficiency of a test receiver with an input of surface temperature and fluid inlet and outlet temperatures. This model can be used to analyze results from on-sun tests wherein the flux distribution cannot be readily measured. The uncertainties in receiver efficiency using this method and its sensitivities to various input parameters are also discussed.

CHAPTER 2
UNIT CELL NUMERICAL MODEL DEVELOPMENT

Grid Discretization

The flow network in a micro-pin-array receiver which is made up of unit cells and modules is described below.

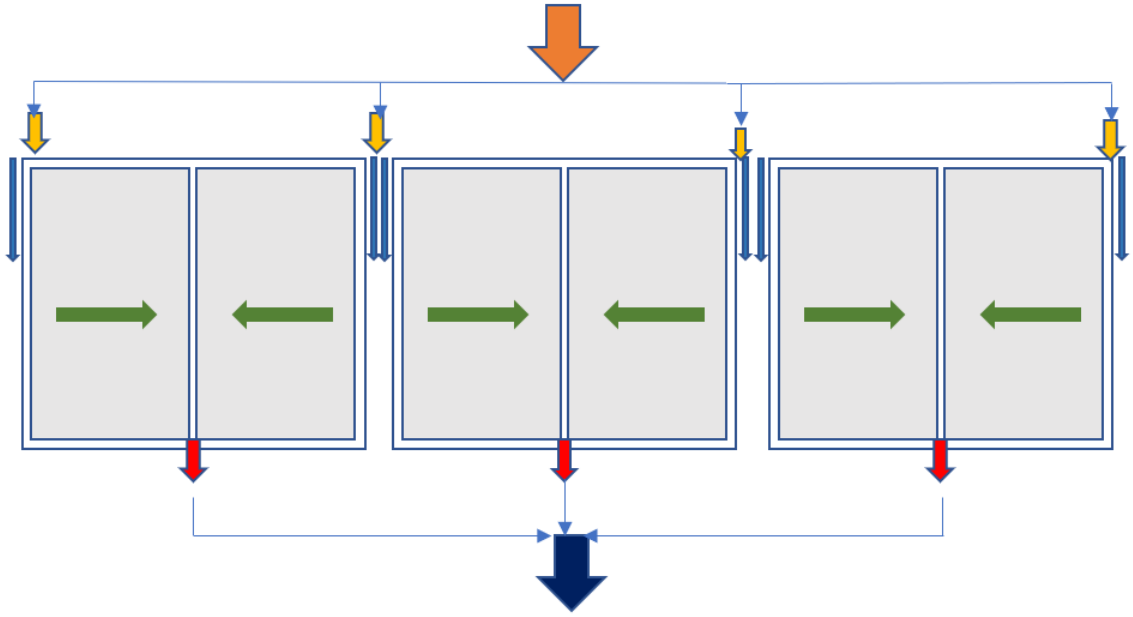

Figure 9: Flow network in a micro-pin-array receiver (MPAR) with 3 unit cells, 4 inlet headers and 3 outlet headers.

Figure 9 shows a receiver module flow network for a module made up of three unit cells. The orange arrow represents the module header. The flow from the module header is distributed into the unit cell headers (yellow arrows). Each unit cell is made up of 2 flow pin-array sections; the flow splits into the opposite ends of the unit cells, which contain integrated headers. The fluid flow is through the unit cell headers, into the unit cell pin arrays (green arrows) and exits the pin

array through outlet headers in the unit cell center (red arrow). The flow is then collected into a single module outlet header (blue arrow). The description of the modeling approach for the pin array is presented in the following section; details of the header design are relegated to future work.

In this study, how an incident solar flux non-uniformity could lead to flow non-uniformity was of interest. Such flow non-uniformity could exist due to variation in temperature dependent properties such as viscosity and density. In order to account for the spatial variation of properties throughout the unit cell of the receiver and the resultant variation in mass flow rate and temperature from inlet to outlet, a 2-dimensional discretized grid (Figure 10(a)) was used. In Figure 10a, the mass flow splits into the different rows (blue arrows) and collects at the exit path (red arrows). Thus, with a horizontal flow path assumed in this simulation, variation in flow rate occurs across the different rows and there is no variation in mass flow along each row; the flow in each row is determined by the viscous resistance in the horizontal flow path. Furthermore, for each control volume, a thermal resistance network (Figure 10 (b)) coupled with an energy balance equation is applied to resolve the flow between two control volumes. In these two dimensional grids, each control volume is assumed to have uniform properties calculated at the face of the control volume—temperature, viscosity, density etc. The temperature of each control volume is determined as the average of the temperature at the edges/faces.

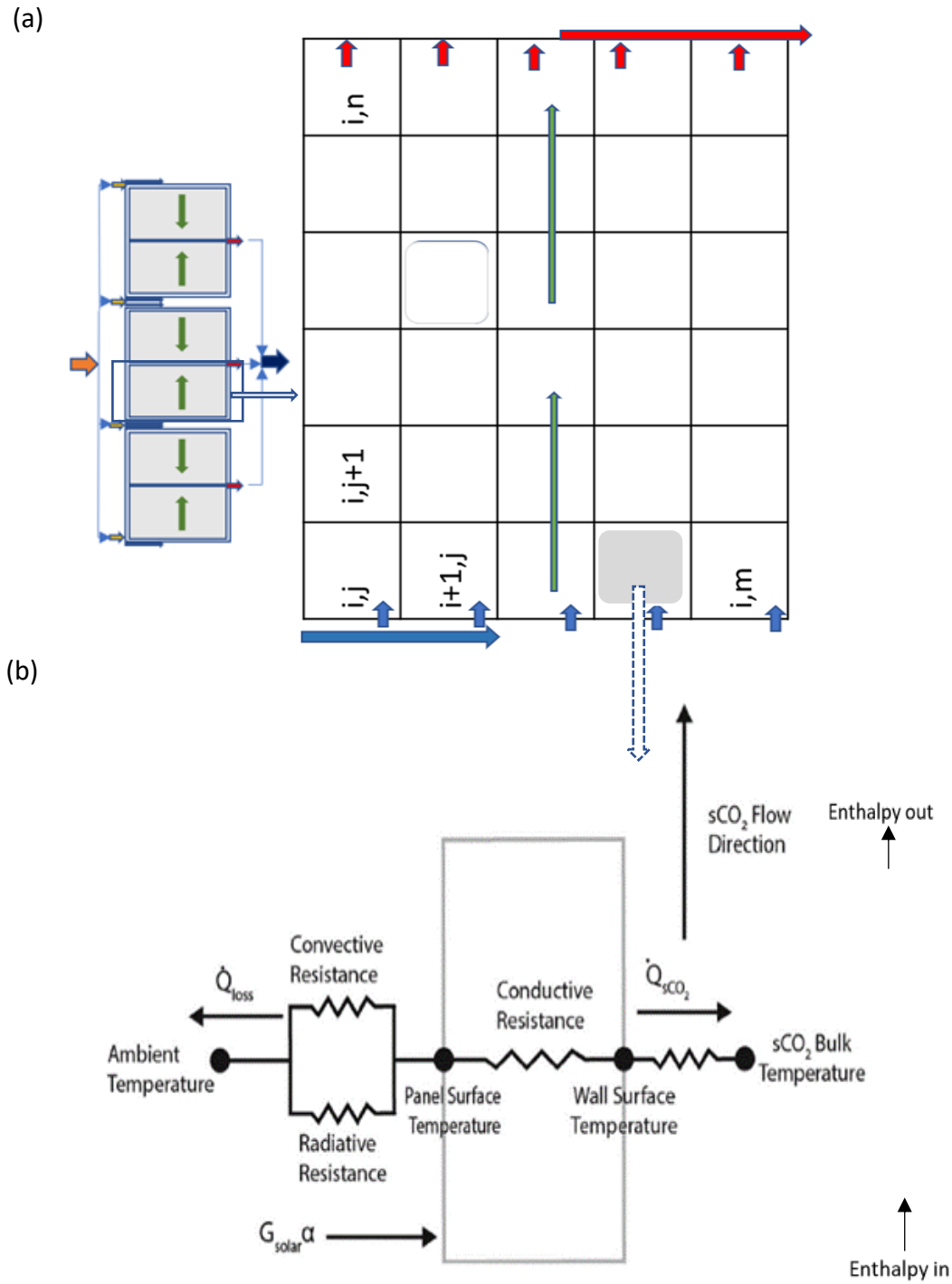

Figure 10: (a) 2-D discretization of the unit cell into control volumes (b) thermal resistance model from [13] which couples with an energy balance equation that solves for each of the control volumes.

Modelling Approach

The numerical model solves for each control volume, shown in Figure 12(a), the energy balance equation coupled with a 1-D resistance model developed in [4]. The model requires an input temperature to the first element of each unit cell. A flux distribution is therefore needed as an input parameter, where the flux will be averaged to a single value within each unit cell. For the energy balance, the heat transfer to the fluid is assumed to be by conduction through the receiver surface, and convection to the fluid. Heat losses from the system are reflective losses, external convection losses, and radiation losses.

To simplify the modelling process and numerical analysis, the following assumptions are made:

1. The mass flow and heat transfer are in a steady state.
2. There is no maldistribution of flow due to design, from the module or unit cell headers. Hence, only the effects of flow maldistribution due to variation in properties among the "j" direction strips is considered.
3. Each control volume has uniform fluid and surface temperature.
4. Fixed heat transfer coefficients are used for external convection heat transfer.
5. Radiation and convection losses are between the surface and the ambient environment that is kept at a fixed temperature (dry bulb temperature).
6. Supercritical CO_2 is treated as an incompressible fluid.
7. Effects of axial conduction in the receiver substrate and fluid are negligible.

The energy balance equation for each control volume (see Figure 12a) is given as:

$$dq_{in} = dq_{fluid} + dq_{convection} + dq_{radiation}$$

$$IC_{i,j} \cdot (dy \cdot dx) \cdot (1 - \rho_{\lambda}) = m_i \cdot \left(h_{i,j} - h_{i,j-1}\right) + h_{conv_{i,j}} \cdot (dy \cdot dx) \cdot \left(T_{so_{i,j}} - T_{inf}\right) + \epsilon \cdot \sigma \cdot dy \cdot dx \cdot \left(T_{so_{i,j}}^4 - T_{inf}^4\right) \quad (2.1)$$

Where IC is the incident heat flux, ρ is the reflectivity coefficient, and ϵ is the emissivity of the receiver surface which is assumed to be a constant. The enthalpies, h at the nodes are used to determine the energy balance in the control volume, while the external convective heat transfer coefficient h_{conv} is assumed to be a constant throughout the receiver, with T_{so} being the local surface temperature of the receiver, and T_{∞} the ambient temperature. For a given mass flow rate, the unknowns in the above equation are $h_{i,j}$ and $T_{so_{i,j}}$.

The heat absorbed by the fluid is given by:

$$dq_{fluid_{i,j}} = m_i \cdot (h_{i,j} - h_{i,j-1}) \quad (2.2)$$

The temperature at a node can be obtained from the enthalpy value divided by the specific heat:

$$T_{i,j} = \frac{h_{i,j}}{C_{p_{i,j}}} \quad (2.3)$$

If the bulk fluid temperature of the node is given by $T_{i,j}$, and the bulk fluid temperature of the preceding node is given by $T_{i,j-1}$, assuming an adiabatic base of the receiver, the heat absorbed by the fluid is equal to the heat transmitted through the receiver. Hence:

$$dq_{fluid_{i,j}} = \frac{T_{so_{i,j}} - 0.5 \cdot \left(T_{i,j} + T_{i,j-1}\right)}{dR\_t_{i,j}} \quad (2.4)$$

Where dR_t is the heat transfer resistance (K/W) in a control volume between the receiver surface and the bulk fluid. By equating (2.2) and (2.4), the bulk fluid temperature of a node is given by:

$$T_{i,j} = \frac{T_{so_{i,j}} - T_{i,j-1} \cdot (0.5 - dR\_t_{i,j} \cdot m_i \cdot C_{p_{i,j}})}{0.5 + dR\_t_{i,j} \cdot m_i \cdot C_{p_{i,j}}} \quad (2.5)$$

The temperature field of the fluid and the surface are obtained by resolving the unknown terms in temperature and resistance. The internal convective resistance in Eq 2.5 is given as

$$dR\_t_{i,j} = \frac{1}{\eta_{0_{i,j}} \cdot h_{int_{i,j}} \cdot A_t} \quad (2.6)$$

Where h_{int} is the internal convective heat transfer coefficient. The overall efficiency of the finned surface, η_0 is given as:

$$\eta_{0_{i,j}} = 1 - \frac{NA_f}{A_t}(1 - \eta_{f_{i,j}}) \quad (2.7)$$

where A_t is the total surface area of the finned surface exposed to convection.

$$A_t = NA_f + A_b \quad (2.8)$$

A_f is the surface area of a single fin = Perimeter x Length(height), N = number of pins in the control volume and η_f is the pin efficiency, given as

$$\eta_f = \frac{tanhmL}{mL} \quad (2.9)$$

where $m^2 \equiv \frac{h_{int}P}{KA_c}$ with $A_c = \pi t^2$, $P = 2\pi t$, and L is the pin height assuming perfect insulation at the pin end.

The internal flow heat transfer coefficient utilized in this simulation is obtained from experimental studies in microscale pin-array heat exchangers [17]. The authors experimentally characterized heat transfer and pressure drop of single-phase fluid flow by varying the pitch and aspect ratios in eight micro-pin-fin arrays. The pins studied in the experiments were diamond shaped with respect to the flow, and the authors developed Nusselt number correlations using two different fluids: PF-5060 and liquid nitrogen, thereby

accounting for the effects of Prandtl number on heat transfer. Then Nusselt number correlation was given as:

$$Nu = 0.039 \times \left(\frac{S_l - D_h}{D_h}\right)^{-0.19} \times Re_{Lc\_Amin}^{0.837} \times Pr^{0.557} \quad (2.10)$$

Here, the above Nu parameter was developed on the assumption of no vortex shedding, applicable over a range $Re_{Lc\_Amin} = 40 - 2300$ and $\mathrm{Pr} = 1.9 - 12.1$.

D_{lc_Amin} is the hydraulic diameter obtained based on the minimum flow cross sectional area within the pin arrays, which is dependent on the pin height, pitch, and pin width/diameter. Furthermore, D_h is the hydraulic diameter based on the pin fin size: in this case, it is simply the diameter of the circular pins.

The Reynold's number based on the minimum flow hydraulic diameter is thus given by

$$Re = \frac{\rho \times V_{max} \times D_{lc\_Amin}}{\mu} \quad (2.11)$$

And the internal heat transfer coefficient is obtained from Nu as

$$h_{int} = Nu \times \frac{k_{bulk}}{D_{lc\_Amin}} \quad (2.12)$$

Where k_{bulk} is the thermal conductivity of the fluid estimated at the mean bulk fluid temperature. A detailed comparison of heat transfer coefficient in micro channels has been addressed in [17].

Pressure drop is an important parameter that determines the sizing of the circulator pump utilized in the receiver loop of a CSP system. Pressure drop in a receiver system can occur from several locations including the headers, the flow line and the unit cells. However, the pressure drop within the unit cell is the largest contributor due to flow through mm-scale passages. Hence, in this work, the pressure drop within the unit cell alone is considered. Limited data are available in literature for supercritical CO_2 flow with micro pin arrays in the range of Re considered in the receiver application. The pressure drop utilized

in this application is obtained from an unpublished experimental correlation based on prior work by our group [Rasouli, personal communication] in microscale heat exchangers with PF5060 as the working fluid. The friction factor is defined as:

$$f = 9.2 * \left(\frac{H_{pin}}{D_h}\right)^{-0.43} \times \left(\frac{S_t - D_h}{D_h}\right)^{0.07} \times \left(\frac{S_l - D_h}{D_h}\right)^{0.07} \times Re_{Lc\_Amin}^{-0.15} \quad (2.13)$$

The pressure drop is given as:

$$\Delta P = f \times N_{row} \times \frac{1}{2} \times \rho \times V_{max}^2 \quad (2.14)$$

Where Vmax is given as the maximum velocity the fluid experiences while travelling through the pin array minimum flow area.

A detailed compilation of the pressure drop correlations from other studies has been provided in [15]. It must be noted that more research is needed in the area of pressure drop in micro pin arrays with sCO_2. However, recent results from experiments with air [Rasouli, personal communication] demonstrate further confidence in the applicable range of the above friction factor correlation, as shown in Figure 11.

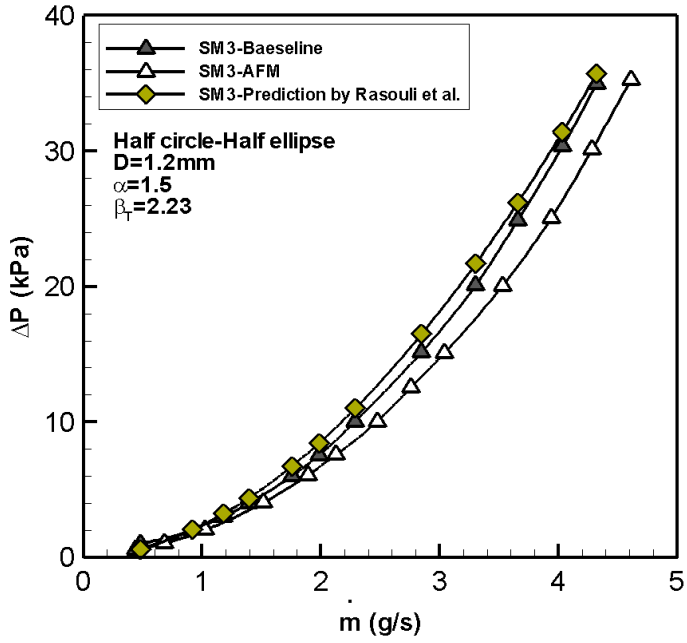

Figure 11: comparison of the sCO_2 correlation by Rasouli et al. with results from pressure drop experiments with air.

In Figure 11, results of pressure drop experiments with the MPAR are compared against friction factor correlation by Rasouli et al. SM3-Baseline is the as build pin array, SM3-AFM is the unit after post-processing with abrasive flow machining. The prediction by Rasouli correlation (green diamond legend) matches the as-built pin array correlation, with a mean error of 6.7%; thus the correlation serves as a conservative estimate of pressure drop. An important parameter that is used to evaluate the performance of the receiver is the thermal efficiency. The thermal efficiency is defined as the ratio of the heat absorbed by the working fluid to the heat absorbed by the receiver.

$$\eta_{th} = \frac{q_{fluid}}{\alpha \cdot q_{incident}} \tag{2.15}$$

Where $q_{fluid} = \sum dq_{fluid_{i,j}}$, $q_{incident} = \sum IC_{i,j} \cdot dx \cdot dy$ and α is the surface absorptivity. In this efficiency calculation, the losses due to reflection are not included.

Numerical procedure

In this work, the equations described in the prior section have been used to study flow with several limiting constraints including:

1. Pressure drop constraint: A pressure drop constraint is applied to determine the limiting temperatures and mass flow rate for a given pressure drop. This consideration is relevant to determining the circulating pump rate to utilize in a CSP plant system, towards keeping the pressure drop within an allowable range. In this study, a pressure drop of 4 bar (2% of the line pressure – 200 bar) is applied as the pressure drop constraint.
2. Fluid temperature constraint: The fluid temperature constraint involves setting the output temperatures of the fluid in a simulation. This constraint gives resulting values of mass flow and pressure drop that would occur if a target fluid outlet temperature is imposed, for a given length of a receiver. Hence, as a design problem, the required length

of the receiver may not be known a priori; the fluid temperature constraint set over different iterations of receiver lengths will give important operating flow parameters: mass flow rate and pressure drop in the system. In this study, a fluid temperature constraint of $720°C$ outlet is used to determine the design length for the receiver system based on a nominal heat flux value of 100W/cm^2.

3. Surface temperature constraint: A significant factor in the implementing a receiver is the material temperature limit. Because the hottest point of the receivers will be at the surface—being the heat source boundary in the receiver—setting a surface temperature constraint based on the material creep life limit determines the realizable fluid outlet temperatures from the receiver within the allowable surface temperature limit. In this study, a maximum surface temperature constraint of $770°C$ is imposed on the external cylindrical receiver to determine the flow operation parameters of the system under the imposed heat flux conditions.

The flow chart (Figure 12) describes the iterative procedure of determining the mass flow rate, pressure drop and the surface temperature distributions for a case of a fixed inlet and outlet temperature (fluid temperature constraint) of an MPAR receiver, which are values based on the SETO Solar receiver goals (550°C inlet and 720°C outlet). These temperature constraint inputs, alongside the parameters of the receiver (such as the length, the pin height, width, and pitch), the operating pressure, and the constant thermal parameters (ambient temperature, convective heat transfer coefficient, emissivity and reflectivity constants) are input into the code. The code calculates the hydraulic diameters and establishes the heat input boundary condition from the heat flux input array. A mass flow rate is instantiated, from which flow properties (Nu, Re and

the internal heat transfer coefficient are calculated). Thermodynamic properties for a control volume are estimated based on the temperature of the first CV.

After calculating the required heat transfer and flow parameters, the code solves iteratively for the surface temperature using a fixed point iteration scheme. The value of the surface temperature is thereafter applied to an empirical relation that determines the fluid temperature at the next node. This process of iterating the surface temperature and calculating the fluid temperature of the $j+1^{th}$ node continues until the last control volume. The code calculates the error between the estimated temperature of the fluid at the last node, and the input output temperature.

Thereafter a process step (Figure 12) is applied to reduce or increase the mass increment or decrement based on the error value. The loop ends when the difference in the calculated outlet temperature is less than 0.03%. The outputs from the code are the mass flow rate, pressure drop, fluid temperature distribution in the flow, surface temperature distribution, and the thermal efficiency of the receiver. The numerical code for this study is executed in Python© 3.8, through Jupyter© notebooks—a web-based IDE capable of running multiple python codes simultaneously. Coolprop© 6.3 property data base is used for the fluid and thermodynamic properties, in which the properties of all fluids are based on Helmholtz-energy explicit equations of state[[18]. This code is modified in other iterations of it (in the further chapters) to apply 1) the pressure drop constraint, and 2) the surface temperature constraint when dealing with the implementation of the MPAR in an external receiver—where multiple modules (consisting of unit cells) are made up into a cylindrical receiver.

(a)

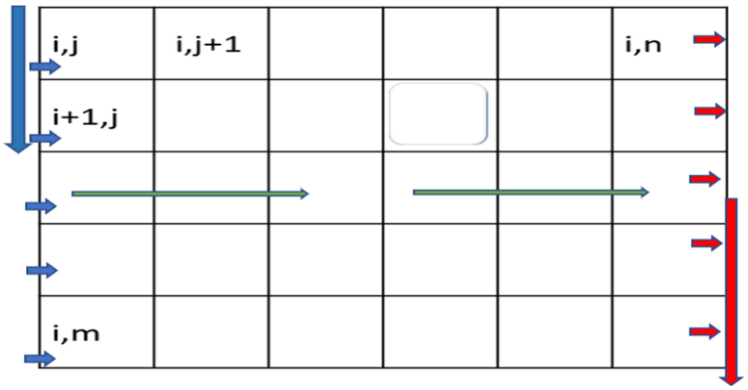

(b)

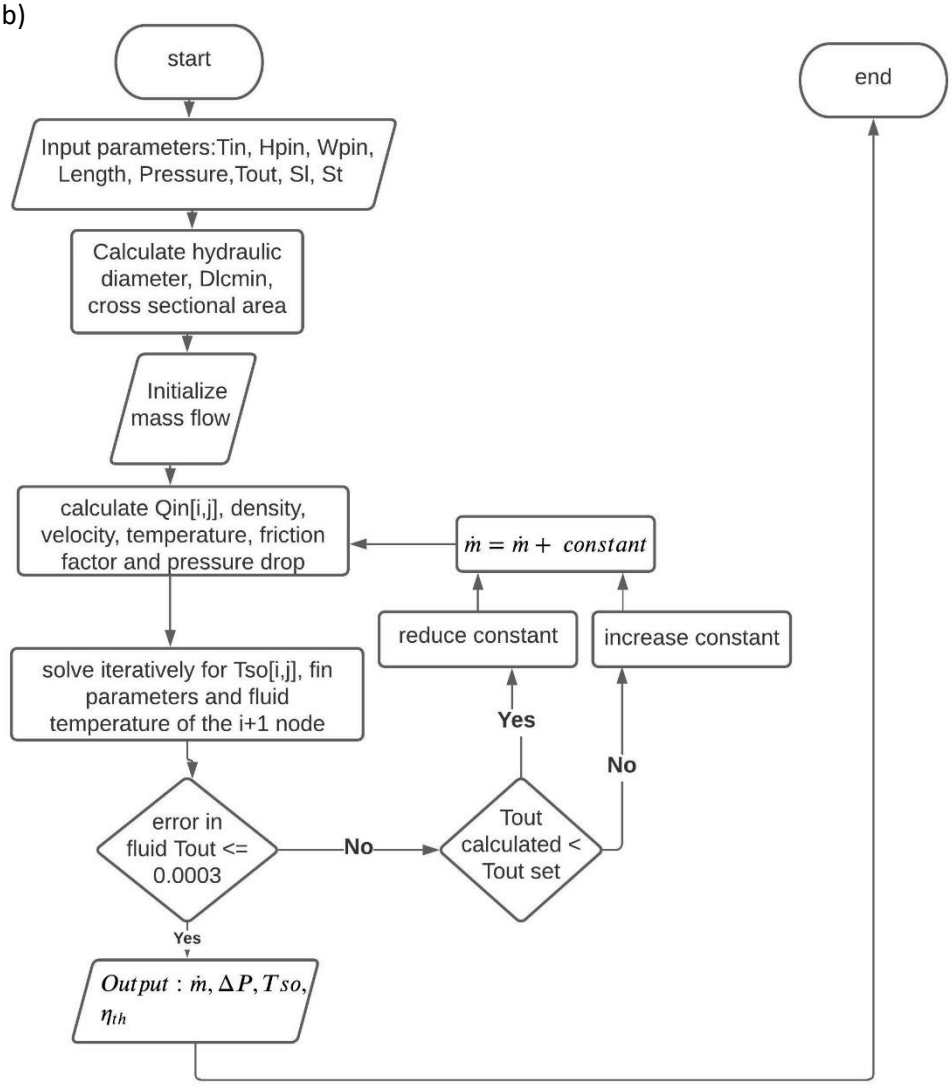

Figure 12: (a) schematic showing the control volume 2 dimensional discretization from inlet to exit (b) flow chart describing the procedure of calculating the thermal and hydraulic parameters of a flow given a fixed inlet and outlet temperature.

CHAPTER 3
UNIT CELL RECEIVER RESULTS

The methods described in the previous chapter have been used to study two different dimensions of a MPAR based on the two available techniques to manufacture microscale receivers:

1. Microlamination (μLPAR): In this method, the pin array is chemically etched in a sheet and then diffusion bonded to a flux plate. Fluidic headers are affixed to the back side of the bonded plates to form a module. In the MPAR, chemical etching limits the design flexibility, requiring shallow pin heights (thus constrained to small ratio of pin pitch to depth) to achieve the necessary pin spacing for mechanical integrity at high pressure since the channel height/width cannot be independently varied. The shallow pin heights result in a smaller flow area, and to minimize the pressure drop, smaller unit cells need to be networked together. For a full-scale receiver, this short unit cell length will result in a more complicated headering system, as more unit cells will be needed to make up a module.
2. Additive Manufacturing (AM^2PAR): In this method, a geometry is created precisely by building layers upon layers of Ni superalloy. The specific AM process considered is a laser powder bed fusion method, where layers of powder are deposited, and a laser scans the design pattern progressively in the build direction. Additive manufacturing has more freedom on the dependency of pin spacing and pin depth (i.e., pin aspect and pitch ratios), and thus allows for larger aspect ratio pin arrays. Additionally, AM allows for flexibility in manipulating pin dimensions from module to module. As a result, some modules could be manufactured to have longer pins, whilst others are made to have shorter pins. This attribute will be shown to be important in designing a Ni superalloy receiver that can meet the creep limit over the lifetime.

An MPAR design for a specific receiver dimension (for example 1m x 1m module), would be better de-risked by having a less complicated header design, which is possible if the unit cell lengths are longer. Hyder and Fronk [14] conducted simulations using the microscale geometric measurements (pin diameter = $300\mu m$, transverse pitch = $600\mu m$, longitudinal pitch = $520\mu m$) with the length of a unit cell, which consists of two pin arrays, given a value of 8cm.

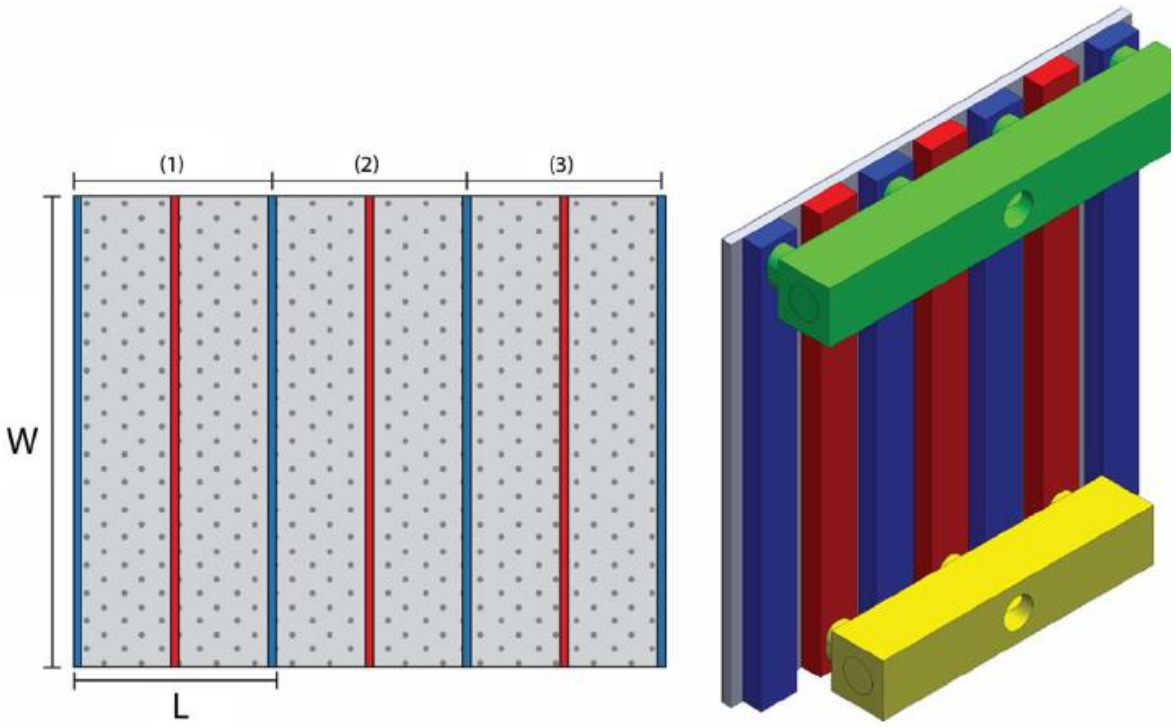

Figure 13: Top view (left) and bottom view(right) of an MPAR module with three unit cells (6 pin arrays).

Thus, a 0.96m long module would require 12 unit cells. The configuration of a unit cell, which involves splitting the flow into two equal halves (2 pin arrays) and collecting the flow at the center means that a unit cell is made up of 2 inlet headers and 1 outlet header (Figure 13). The 0.96m-long module would therefore contain a minimum of 25headers (13 inlet headers and 12 outlet headers). The larger the number of headers in a system, the more complicated the system becomes. The goal of this section is to

study the different ways in which the header dimension can be reduced, by adopting manufacturing methods which allow for more flexible pin heights, and thus lower pressure drop.

Additively Manufactured Vs Microlaminated Receiver (AM^2PAR Vs µLPAR) Unitcell Lengths

Parametric runs of the model were conducted to study the differences in the thermal and hydraulic performance of a µLPAR compared to an AM^2PAR receiver. In the previous chapter, a numerical model developed to solve the flow within a micro-pin array receiver was presented. To conduct this study, dimensions of receivers based on already manufactured receivers being utilized in prior and concurrent research studies were utilized.

Table 1:Pin dimensions of micro-pin array receivers based on manufactured prototypes of micro-pin fin arrays used in prior and concurrent research studies by our group.

	Hpin(mm)	**Wpin(mm)**	**Sl (mm)**	**St(mm)**
µLPAR	0.3	0.35	0.7	0.7
AM^2PAR	1.8	1.2	2.13	2.46

In the measurements from Table 1, all the parameters have the AM^2PAR design to be less than 4 times the µLPAR, besides the height of the pin which is a multiple of 6 times the microlaminated design. Recall that the limitation in microlaminated receiver design is in having shallow pin heights due to isotropic etching, hence the wide difference.

To compare the thermal and hydraulic performance of the µLPAR and AM^2PAR receiver unit cells, a simplified model as described in Figure 14 was employed with a uniform flux of $100W/cm^2$ is used. The flow is bounded by the inlet temperature and constrained by an exit fluid temperature condition of 550°C and 720°C respectively (based on DOE SETO initiative temperature targets) [9].

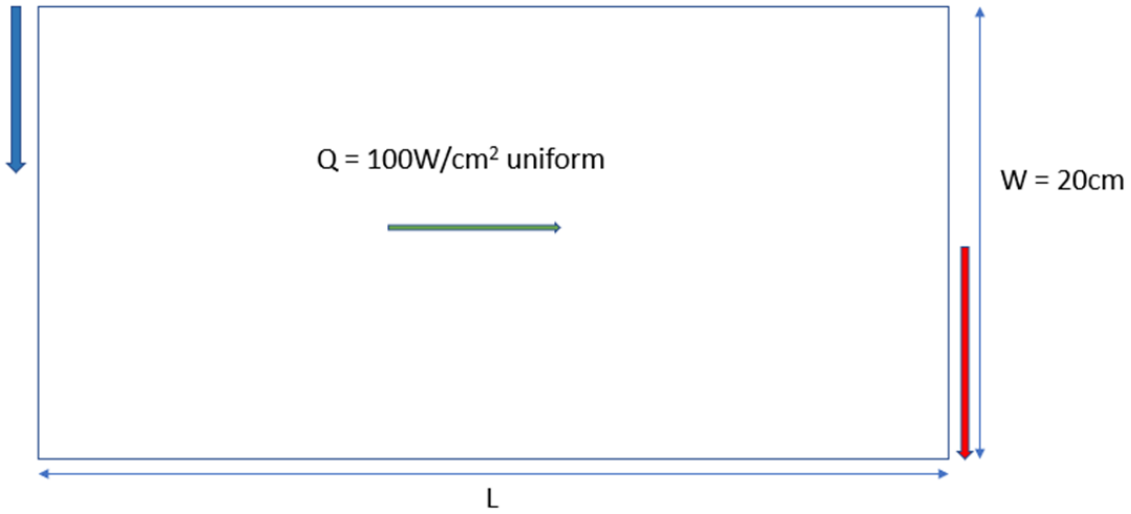

Figure 14: This model shows a uniform flux applied on a single pin array. A uniform flux all through, implies that there is no vertical variation in fluid and thermophysical properties, but there is variation along the flow path (horizontally) as the fluid heats up. Hence such a model can be simplified into a one-dimensional analysis. An array of lengths (ranging from 2.5cm to 30cm) are simulated to determine the relationship between the length of a unit cell and the associated pressure drop for a given outlet temperature constraint.

The width of the unit cell is limited by the available manufacturing capabilities of additive manufacturing equipment (EOS M290 [19]) at the time of conducting the simulations. With respect to the energy model developed in the previous chapter, convective and radiative heat loss are assumed to be at the same dry bulb temperature (T_{inf} = 39°C) and a convective heat loss value of 8.8 W/m^2-K value is used based on flow over a flat plate at an average windspeed of 17m/s. All other fin parameters are employed in the model as described in the preceding chapter.

AM^{2}PAR vs µLPAR Pin Array Length Parametric Studies

In this section, a parametric study is conducted by varying the pin array unit cell length to understand the impact of this change on maximum surface temperature, thermal efficiency and pressure drop for both µLPAR and AM^{2}PAR. In the design of a receiver, a combination of maximum pressure drop limit, inlet temperature and desired outlet temperature and the desired operating temperatures govern the receiver pin array length utilized for a fixed imposed flux. The first step in the simulation process is to determine the mass flow and the pressure drop that will occur if the receiver is designed to heat fluid from 550°C to

720°C at a uniform incident flux of 100 W/cm^2. Figure 15 shows the results of the pressure drop in the unit cell pin array as a function of the length for both the µLPAR and AM^{2}PAR for the specified temperature and flux constraints. The maximum permissible length of the pin array is the length at which the maximum target pressure drop (less than 2% of 200bar, i.e., 3.5 bar in this study) is obtained. This datum line is indicated in Figure 15.

For a given heat flux value, the total heat rate on the unit cell pin array increases with an increase in the design length of the receiver, which leads to a corresponding increase in mass flow to attain the same temperature rise. Hence as shown in Figure 15, the pressure drop increase is a result of both an increase in mass flow rate and the number of rows of pins in the array with an increase in length.

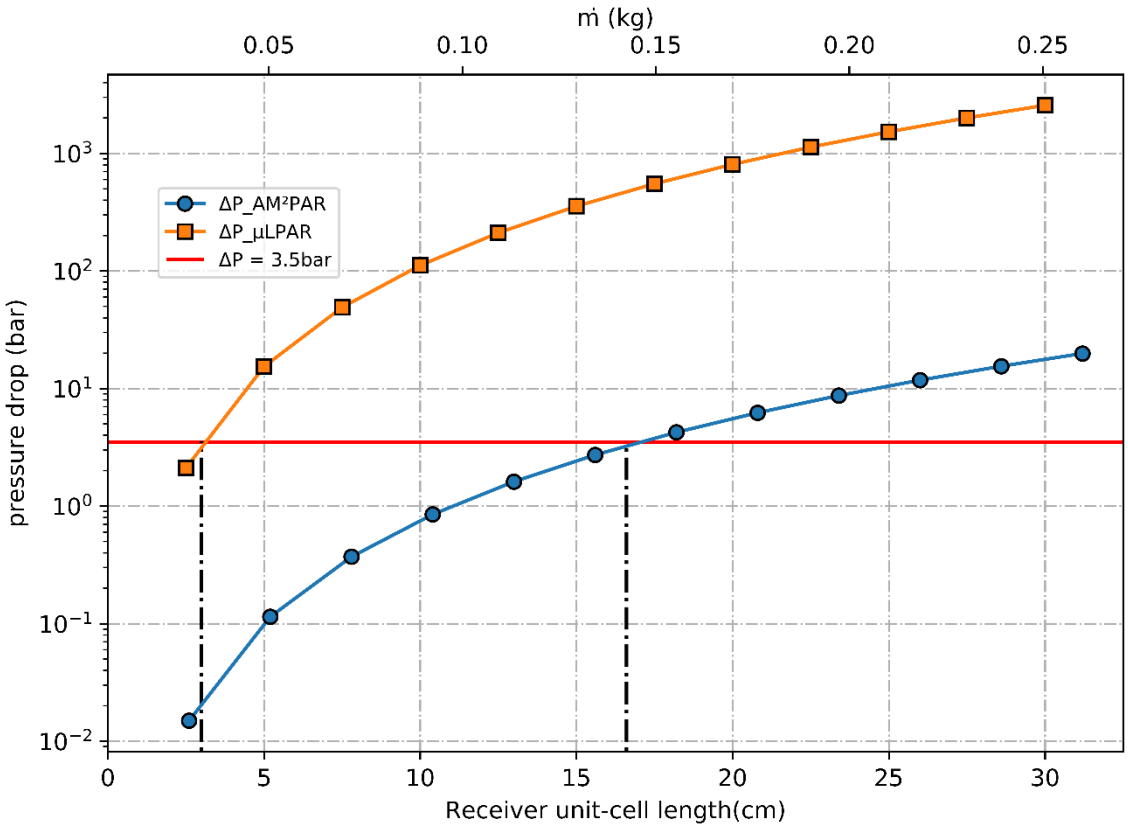

Figure 15: Pressure drop vs unit cell length for receiver unit cell lengths ranging from 2.5cm to 30cm.

As noted in Table 1, the pin height of the microlaminated receiver design is a factor of 6 smaller. Thus for the same length of pin array, the pressure drop in the AM^{2}PAR unit cell is two orders of magnitude lower than the μLPAR design. In Figure 15, the dashed vertical lines indicate the respective maximum permissible lengths of the unit cell receivers for which a pressure drop of 3.5bar is attained: 3.3cm for μLPAR, and 16.6cm for AM^{2}PAR, respectively. These unit cell lengths serve as the basis of the design of the modules that would be combined in parallel to make up a central receiver. The length of a unit cell of the additively manufactured design, having a longer pin, is 5 times that of the microlaminated design. This reduction in the number of unit cells per unit area of the AM^{2}PAR implies that for a receiver module, which is made up of unit cells connected by headers, much fewer unit cells as well as headers would be needed to make up the system, as compared to the microlaminated receiver design.

It is important to however study the thermal parameters to understand the thermal performance, and to consider whether any drawbacks exist in utilizing the AM^{2}PAR. Figure 16 shows the thermal performance of μLPAR and AM^{2}PAR unit pin array with lengths ranging from 2.5 cm to 30 cm. The ordinate on the left represents the maximum surface temperature, and the ordinate on the secondary axis represents the thermal efficiency. The maximum surface temperature on the receiver surface occurred at the fluid exit location, where the fluid is the hottest.

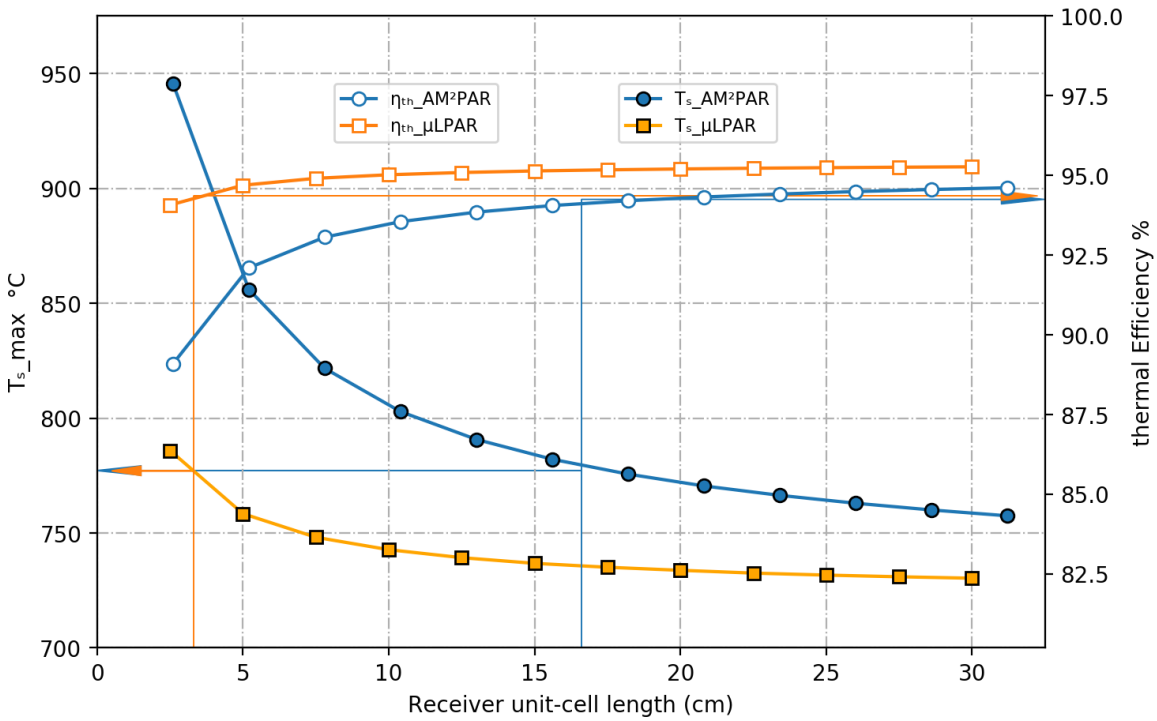

Figure 16: comparison of the thermal performance of additively manufactured and microlaminated receiver unit cells.

Thin arrowed lines from the plot indicate the maximum surface temperatures for each of the receiver maximum pin array lengths based on pressure drop constraints (see Figure 16).

The plot in Figure 16 shows a trend of increasing thermal efficiency for both receiver designs, with an increase in length. This phenomenon is explained by the increase in total heat on the receiver surface (as heat flux is constant in the simulation), with length. Since the temperature change targeted is constant, the increase in total heat on the unit cell surface is proportional to the increase in the mass flow rate required. The corresponding result is an increase in the internal convective heat transfer coefficient, causing more heat to be absorbed from the surface, thereby decreasing the receiver surface temperature (as seen in the same figure) and hence increasing the thermal efficiency.

In addition to the observed trends in thermal efficiency and maximum surface temperature, it is imperative to compare the thermal performance of the AM^{2}PAR and µLPAR receivers. The plots in Figure 16 show that for a given length, the microlaminated receiver has a higher thermal efficiency than the additively manufactured receiver. Furthermore, the maximum surface temperatures for the µLPAR receivers are lower than that of the AM^{2}PAR receivers. This plot is explained by the fundamental definition of a microchannel, where for a given Nusselt number, a lower diameter (or height) results in a higher heat transfer coefficient. Thus, an increased efficiency is realized for the microlaminated unit cell receivers as a result of their smaller heights—and a lower surface temperature is produced as a result.

As noted previously, however, the proper comparison of the two receiver is based on the maximum pressure drop criterion (3.5 bar in this study.) Thin vertical lines in the plot indicate the desired design point (3.3 cm) of the µLPAR receiver, and the desired design point (16.6 cm) of the AM^{2}PAR receiver. The horizontal lines trace the maximum surface temperatures realized (to the left axis) and the overall thermal efficiency of the receiver unit cell (traced to the right axis). The plot in Figure 16 shows that the thermal performance of the additively manufactured and microlaminated design compare closely at the respective design points of each of them—as indicated by the overlap in the arrowed lines. At 3.3cm design length, the µLPAR has a thermal efficiency of 94.45%, while at 16.6cm design length of the AM^{2}PAR, the thermal efficiency is 94.06% (0.4% difference in thermal efficiency between both designs). Also at their respective design lengths, the µLPAR and AM^{2}PAR have a maximum surface temperature of 777.03^{0}C and 777.17^{0}C respectively. Thus, in as much as the µLPAR receivers tend to be better in terms of thermal performance at identical lengths, because of the higher heat transfer coefficient due to their shorter channels, the pressure drop criteria limits the length of the µLPAR. This length restriction results in a situation where the longer AM^{2}PAR unit cell has comparable heat transfer performance with the advantage of less header

complexity: longer unit cells require more mass flow to achieve the same fluid temperature difference at the inlet and exit, thus leading to higher heat transfer coefficients.

AM²PAR vs µLPAR Receivers - Local Variation Comparison At Maximum Pin Array Lengths

In this section, a case study investigates the local variation from the inlet of the micro-pin array unit cell to the exit, between the AM²PAR and the µLPAR receiver. The comparison is made by considering the maximum pin array lengths based on pressure drop constraint—3.3cm for the µLPAR design with mass flow rate = 27g/s and mean Re = 7000, and 16.6cm for the AM²PAR design with mass flow rate = 139g/s and mean Re= 28000. Figure 17 shows the variation of local bulk mean fluid temperature, T_fluid, surface temperature, Ts, and local heat transfer coefficient, htc, as a function of the non-dimensional distance from inlet to exit of the pin array for both µLMPAR and AM²PAR. In the plots, the 0th index represents the first cell after the inlet cell, whilst the 1.0 index represents the last cell. It is worthy of note that the heat flux incident on both receivers is constant at 100W/cm^2, and the total heat rate incident on the AM²PAR pin array is about 5 times the heat rate that is incident on the µLMPAR.

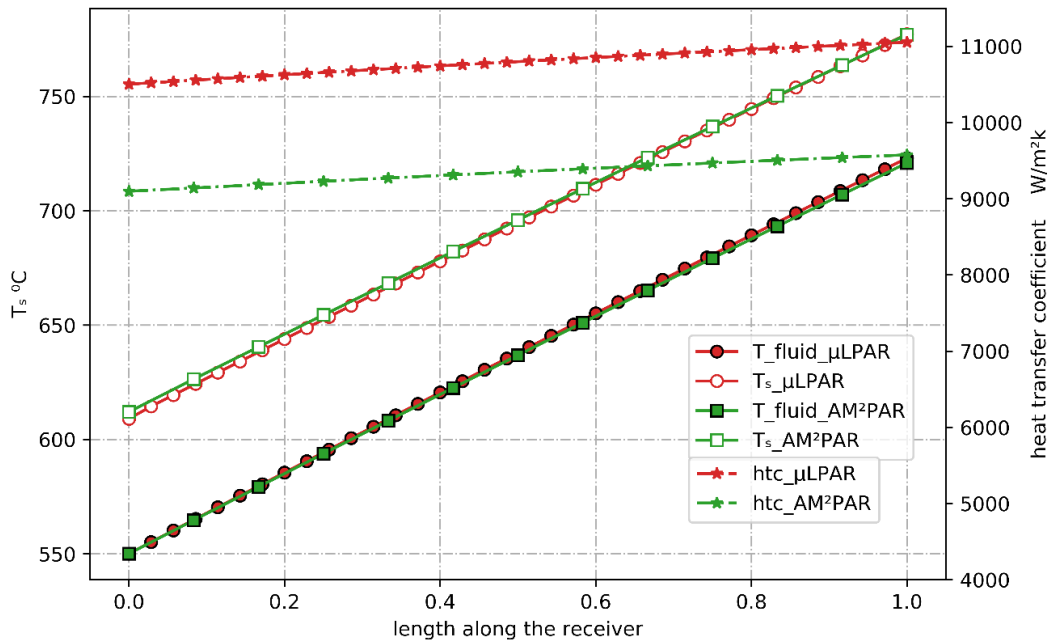

Figure 17: Comparison of the local surface and bulk fluid temperatures (primary ordinate) and heat transfer coefficient (secondary ordinate) of µLMPAR and AM²PAR pin arrays as a function of non-dimensional length.

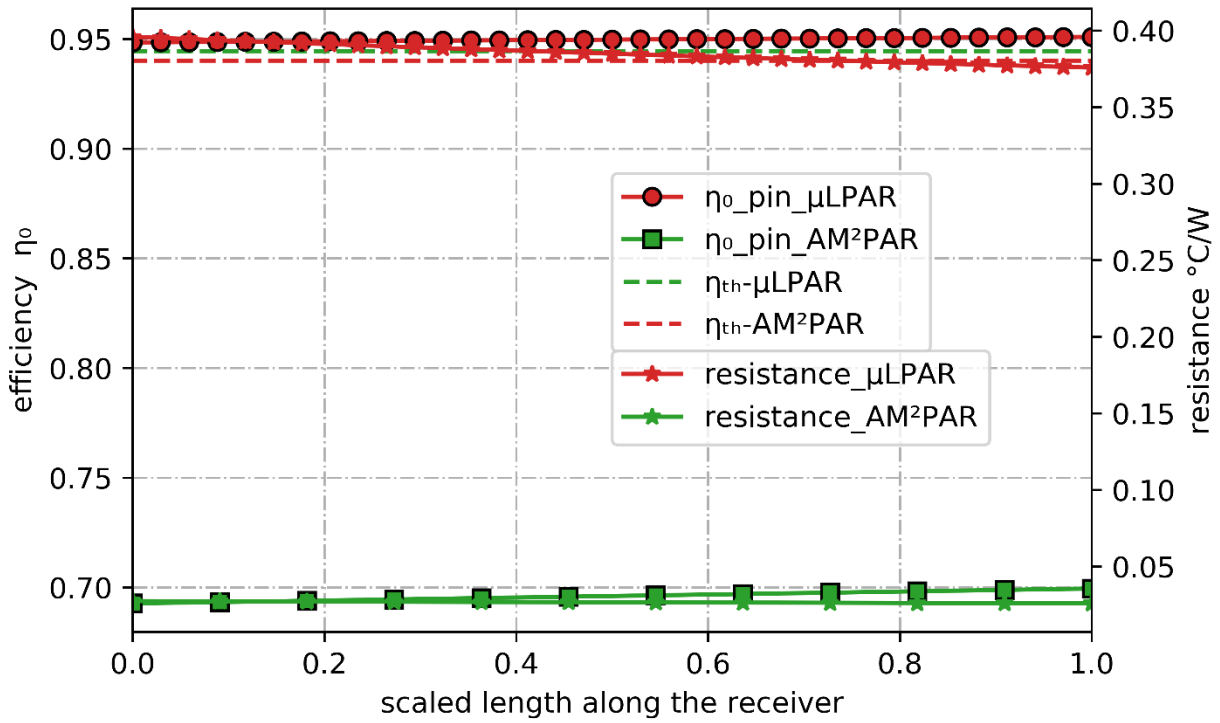

Figure 18: plot comparing internal flow thermal resistance and overall fin efficiency of the microlaminated (3.3cm scaled to 1.0) and additively manufactured (16.6cm scaled to 1.0) unit cell receivers.

As expected, the μLMPAR has a higher heat transfer coefficient as a result of the lower hydraulic diameter of the channel, despite the higher Re in the AM^{2}PAR case. In Figure 18, the other internal flow parameters that influence the heat transfer (overall fin efficiency and the resulting resistance due to the pin size and heat transfer coefficient. The pin efficiency of the AM^{2}PAR receiver pins is calculated to be 26% lower than the μLMPAR pin, however the resistance of the additively manufactured receiver pins is 8 times lower than the microlaminated pins due to an increase in total area for heat transfer, which is the dominant contributor to the heat transfer resistance. In summary, the internal flow parameters show how the total heat transfer area (higher and longer channel) negates the impact of lower overall finned surface efficiency and heat transfer coefficient and is the major correlating factor with the flow-rate that contributes to the comparable thermal efficiency and performance of the receiver.

AM²PAR vs µLPAR Receivers- Variation of Incident Flux

The simulations in the previous sections have been conducted using a uniform heat flux of 100W/cm^2 to achieve a fluid temperature change from 550°C to 720°C across the unit cell. In theory, higher heat fluxes are associated with a higher efficiency, and the heat fluxes the receiver will be exposed to in practical applications would vary from low to high during the diurnal cycle. Thus, a study was conducted to understand the difference in the thermal performance of the receiver in a range of heat fluxes expected to be encountered in practical scenarios. It is important to study the impact of the heat flux on surface temperatures because Nickel superalloys have creep limits. For example, Haynes 282 under a specific pin-array configuration has a temperature limit of about 800°C for a 30-year creep life for a 200-bar receiver design [Ines et al, personal communication].

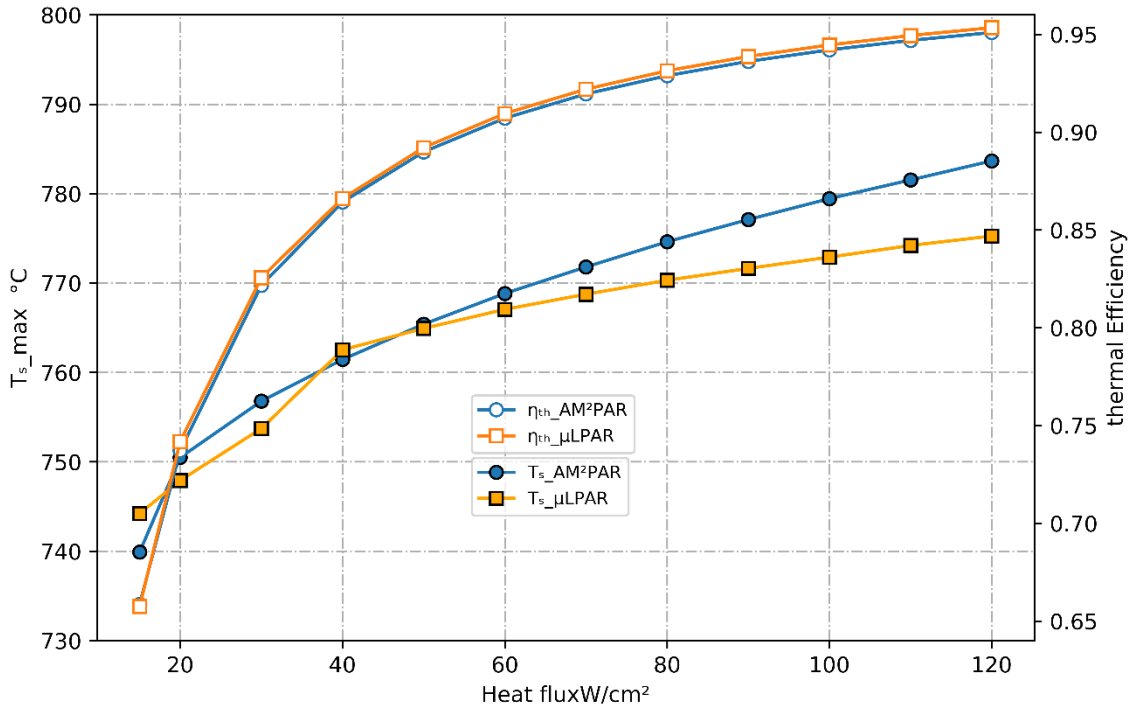

Figure 19: Comparison of the AM^{2}PAR (unit cell length = 16.6cm) and µLPAR (unit cell length = 3.3cm) receivers' thermal performance over a range of heat flux from 20W/cm^2 to 120W/cm^2 for flow temperature increase from 550 to 720°C.

From Figure 19, it is seen that the maximum surface temperatures are higher at higher fluxes because for a constrained output temperature, the increased flux means an increased difference between the surface and the fluid temperature. The thermal efficiencies are as well higher at higher heat fluxes because an increased mass flow rate, and thus a higher convective heat transfer coefficient, which are required to achieve the constrained output temperature cause the increase in heat absorbed by the fluid to be more than the increase in the heat lost to the environment.

From Figure 19, the plot of heat flux against surface temperatures shows a higher surface temperature trend with increased heat flux, and slightly higher surface temperatures for the AM^{2}PAR compared to the µLPAR for fluxes above 40W/cm^2. The surface temperatures of the AM^{2}PAR are higher because the receiver is larger (16.6cm length compared to 3.3cm length) thus the same heat flux and temperature constraints require larger mass flow. However, the heat transfer coefficient increases by a fraction of the total heat input, leading to higher surface temperatures with increasing heat fluxes, and higher surface temperatures for the AM^{2}PAR than the µLPAR receiver. Furthermore, the slightly higher slope of the AM^{2}PAR receiver can be explained by Figure 20 which shows a considerably steeper decrease in the pin efficiency of the AM^{2}PAR with increasing heat flux. As a result, inasmuch as the thermal resistances (Figure 20) decrease with increasing heat fluxes (increasing convective heat transfer coefficients) the thermal resistance of the AM^{2}PAR declines at a slower rate than that of the µLPAR receiver.

Figure 21 shows the comparison of the heat losses and heat transfer coefficient trends with solar flux in the AM^{2}PAR receiver. As the heat flux is increased, a corresponding increase in the mass flow rate is needed to maintain the same fluid temperature rise (in this case from 550°C to 720°C.) This increase in mass flow leads to an increase in the internal heat transfer coefficient in a pseudo-linear form. As a result, the convective heat flow to the fluid in such constrained fluid temperature target is dominated more by the heat transfer coefficient with a 7% increase in surface temperature range.

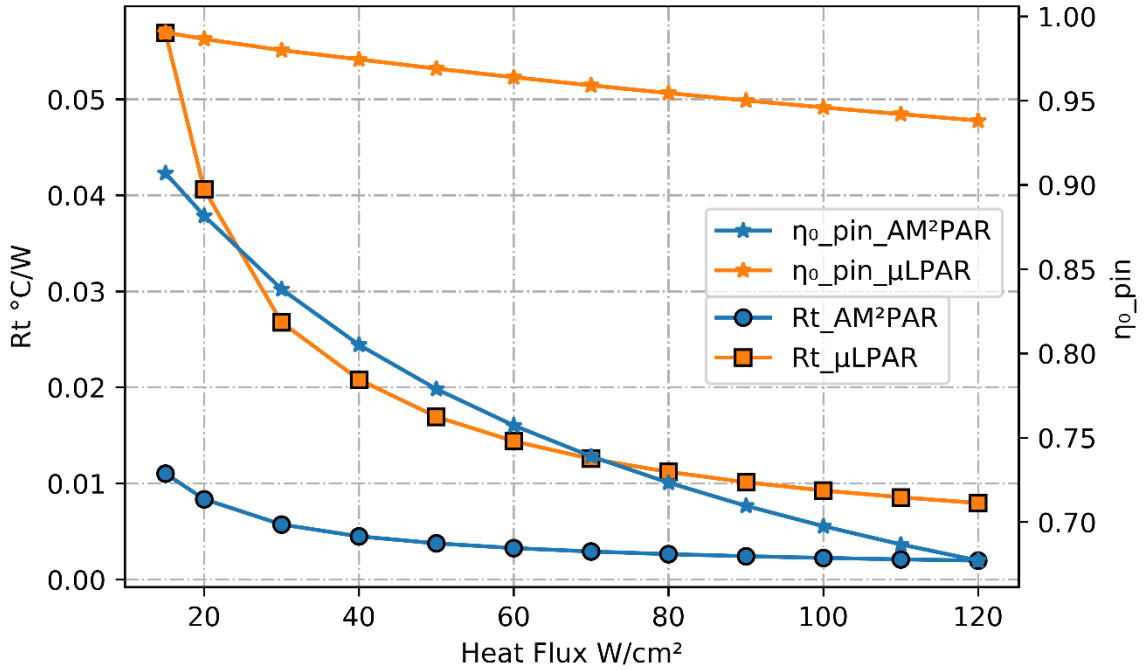

Figure 20: plot comparing the pin resistances and the pin efficiencies of the µLPAR and AM²PAR receivers over a range of simulated heat fluxes, for a target inlet temperature of 550°C and a constrained outlet temperature of 720°C.

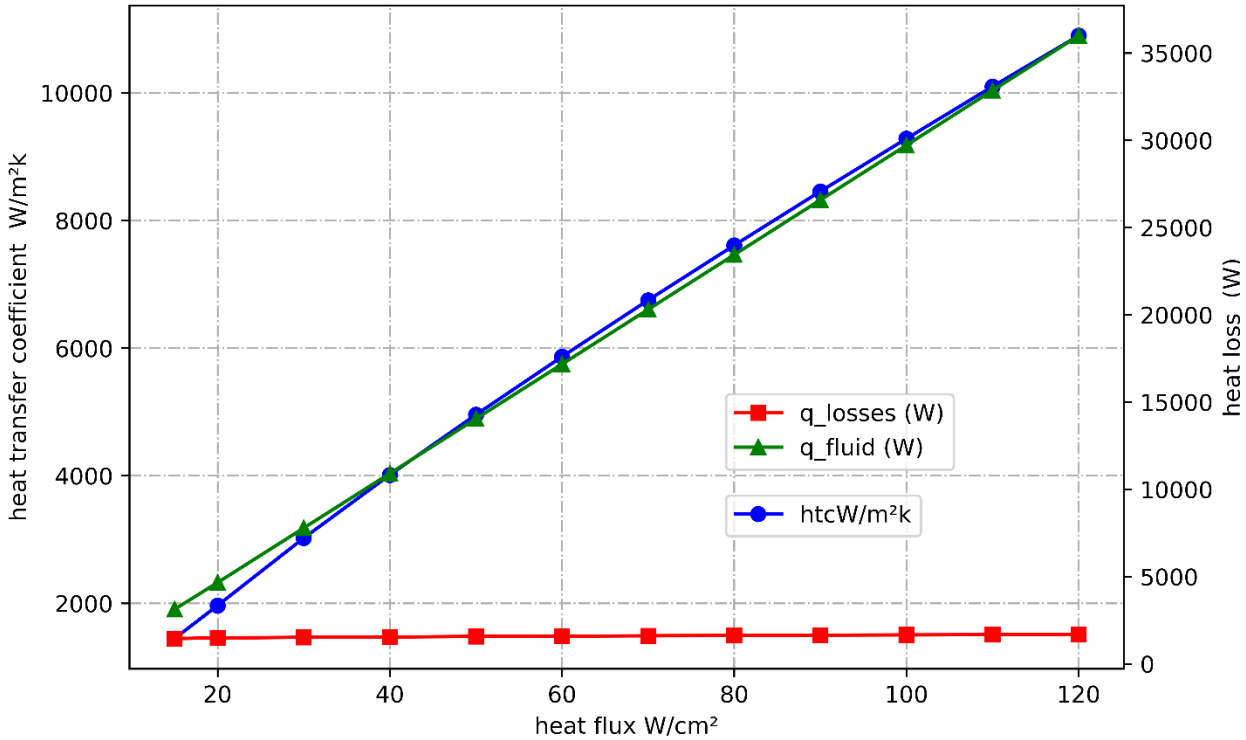

Figure 21: Plot of the convective heat transfer coefficient and the heat losses in an additively manufactured micro-pin-array receiver for a fixed temperature increase of 550 to 720°C.

Hence, inasmuch as there is an increase in heat loss due to increase in incident heat flux, the increase in heat absorbed by the fluid is considerably much more than the increase in heat loss due to convection and radiation, as a result of the higher heat transfer coefficients—as seen in the overlap of the green and blue lines in Figure 21. As a result, the radiation heat loss has a similar magnitude across a wide range of practical heat fluxes as studied, but its relative effect becomes less dominant as the heat flux on the receiver increases—for a target fluid temperature increase.

CHAPTER 4
CENTRAL RECEIVER DESIGN AND MODELLING

The AM^{2}PAR receiver has been compared with the µLPAR receiver in the previous chapter. The overall goal is to integrate the selected receiver design into full-scale receiver for a commercial scale CSP power plant. In this chapter, the determining factors, methods, and analysis towards the integration of the AM^{2}PAR receiver into a CSP plant are discussed. Heat absorbed by the fluid in a receiver is as a result of the incident flux map produced on it. This flux map can be produced—based on the heliostat orientation and control—in theory and in in-situ applications through what is called aiming strategies. A brief introduction on aiming strategies is presented in this chapter; thereafter the power generation considerations of a full scale receiver are presented and used to determine the requirements of the full scale CSP plant being used in this feasibility study. These requirements are used to set up/generate a CSP field through the software SolarPILOT [20] which is a solar field layout and characterization tool developed by NREL. Finally, the application of the flux generated by the solar field through SolarPILOT, and the formulation of the receiver to perform a thermal performance analysis with the flux are discussed.

Heliostat Field Layout and Aiming Strategies On Central Receivers

The heliostats in a central receiver field can be arranged to achieve aiming based on the operational limits of the receiver. These operational limits could be based on flux spillage loss considerations, structural integrity, peak heat flux limitation, thermal optimization considerations and overall cost considerations. Most of the techniques for generating a heliostat field layout and for defining the aimpoints on the receiver are based on algorithms. A comprehensive review and comparison of heliostat field layout algorithms can be found in Barberena et al. [21]. Broadly, the aiming strategy on the receiver can be classified into two categories:

a. Equatorial aiming

b. Non-equatorial aiming.

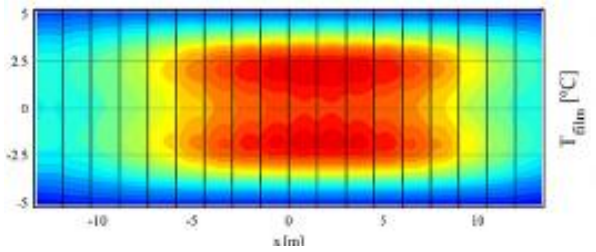

Figure 22: equatorial aiming on a receiver (source: [22])

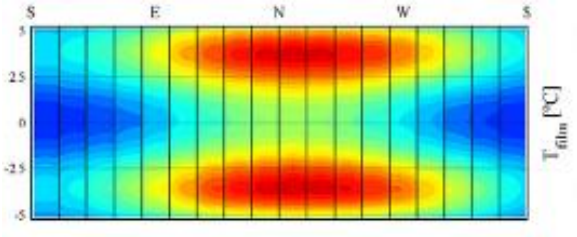

Figure 23: non equatorial aiming on receiver (source: [22])

The equatorial aiming strategy (Figure 22) has higher flux intensity around the center of the receiver, whilst the non-equatorial aiming strategy (Figure 23) has the flux concentrated on the ends of the receiver, by vertically shifting the aim points from the center. The equatorial aiming approach is practically simpler than the non-equatorial aiming approach, however this tends to overconcentrate the heat flux on the center of the receiver. This could lead to hotspots and mechanical integrity failure of the receiver. The non-equatorial (multi-aiming strategy), by vertically shifting aim points unevenly, tends to reconcentrate the heat flux to optimize the thermal performance of the receiver whilst maintaining its mechanical integrity.

Much research on understanding of the relevance of the non-equatorial aiming strategy in molten salt cylindrical receivers, is seen in research by Sanchez-Gonzalez et al.[22], [23],. It must be stated however that the flow path in typical molten salt receivers follow a serpentine up and down pattern, with one end of the receiver being the inlet and the other end being the exit. As a result of this flow pattern, the allowable flux densities in such a receiver will tend to concentrate at the extreme ends, and as such multi-aiming strategies become more convincing. In microchannel receivers however, the flow is distributed to several inlets in circumferential and vertical span of the receiver, and thus the flow pattern does not indicate a preference for an aiming strategy. Moreover, the solar field generated by SolarPILOT which used in this study uses an equatorial aiming strategy, where the flux is evenly distributed on the surface[24].

Solar Flux Mapping on Central Receivers

A central receiver design begins the determination of the geographical location and the number of heliostats to be placed in the given field. Field optimization is thereafter performed by considering the field layout, tower optical height, and receiver dimension. In more detailed selection of the combination of parameters that provides the lowest cost of energy, an annual weather file, a calculation of the allowable incident flux on the receiver as a function of the time of the day and the day of the year, the optical accuracy of the heliostat as a function of wind speed, and costs of the entire system infrastructure including piping would be considered [25].

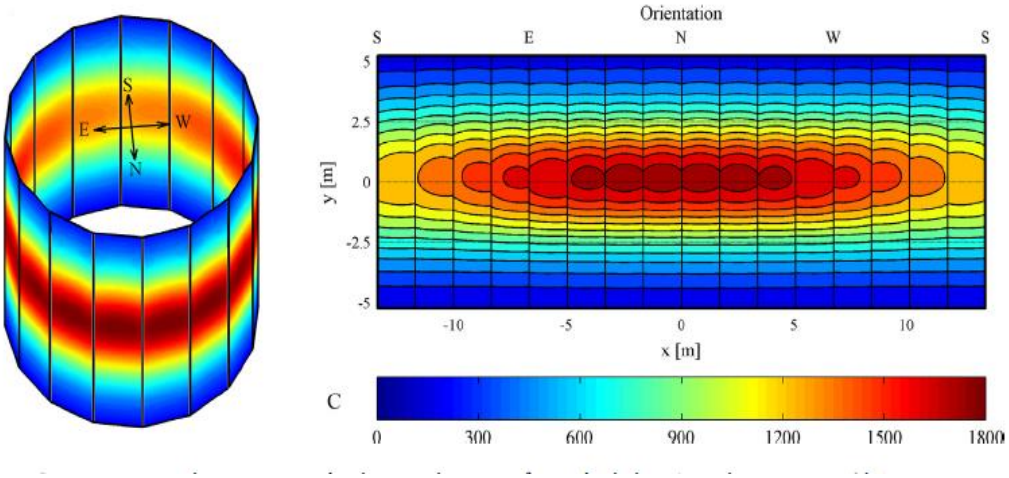

Figure 24: Non uniform flux profile on a central receiver (source: [26])

The flux profile on a central receiver is a critical aspect of modelling the thermal and hydraulic performance of the central receiver. As shown in Figure 24, the flux profile around a central receiver is highly non uniform. The allowable incident flux on a receiver for a given power is an optimization of the effects of decreasing the receiver area which results in an increase in spillage (flux from the heliostat field that misses the receiver), and the thermal gradient established between the front of the receiver (absorbing the flux) and the back of the receiver which is not illuminated[25]. In literature, two major methods of flux mapping have been identified:

a. **Monte Carlo ray-tracing methods (Numerical approach)**: In this method a bundle of random rays is traced from the sun by the application of statistical methods. The more the rays that are traced, the higher the achieved precision. However, this precision increase comes with the penalty of computational cost.
b. **Analytical approach**: This method works with statistical model/function of the heliostat flux density, in which the flux value is directly calculated through the mathematical superposition of

error cones (sun-shape, concentration and mirror errors). Two main mathematical description methods important for resolving the analytical approach are the convolution integral approach and an overall approximation based on Gaussian distribution [27].

The scope of this study does not cover the flux mapping methods and aiming strategy. The study however applies the use of the SolarPILOT software which uses a combination of the Monte Carlo ray-tracing methods and Convolution methods in providing flux maps. Further details of mathematical modelling can be found in [26], [28], [29].

Power Generation Considerations

The central receiver tower plant is made up of a field of heliostats strategically positioned to concentrate solar irradiation on an elevated central receiver. The sizing of a central receiver plant is dependent on the power generation goal of the plant. In developing a CSP plant system, consideration is given to the annual variability of the sun's intensity, and the overall efficiency of converting the sun rays into thermal energy. In a heliostat field, the sun rays strike the heliostats and are specularly reflected onto the receiver. The ideal total power incident on the receiver is the sum of the superimposed solar irradiation reflected by the heliostats on the central receiver. The power generation capacity of a field therefore is driven by the number of heliostats on the field, the overall optical efficiency of the heliostats, and the receiver absorption efficiency. An optimized receiver typically operates at high receiver efficiencies (about 90%), however the optical efficiency of the heliostat field contains many contributing factors that result in a lower efficiency value compared to the receiver absorption efficiency, which reduces the total power incident on the receiver surface. The optical efficiency of the field which impacts the heat incident on the receiver is given as:

$$\eta_{opt} = \eta_{at} \times \eta_{ref} \times \eta_{s\,\&\,b} \times \eta_{cos} \tag{4.1}$$

Where η_{opt} is the optical efficiency, η_{at} is the atmospheric attenuation efficiency, $\eta_{s\ \&\ b}$ is the shadowing and blocking efficiency, η_{ref} is the reflection efficiency and η_{cos} is the cosine efficiency. These efficiencies are described below:

i. Atmospheric Attenuation Efficiency

Atmospheric attenuation loss results from energy of the reflected rays from the heliostats being scattered and absorbed by the atmosphere. The atmospheric transmission efficiency majorly depends on the distance between the heliostat and the receiver, as well as the prevailing weather conditions.

ii. Shadowing and Blocking Efficiency

Shadowing results from the casting of a shadow by one heliostat onto a neighboring heliostat. Blocking on the other hand is a result of heliostats in the foreground blocking a heliostat's reflected flux. Both shadowing and blocking efficiency can be mostly corrected through rigorous optimization of the solar field.

iii. The Cosine Efficiency

The cosine efficiency is a consequence of the angle between the incident solar beam radiation, and the normal vector to the surface of the heliostat. The cosine efficiency thus depends on the position of the heliostat relative to the sun. The cosine loss is one of the most significant losses in the heliostat field[20].

iv. Reflection Efficiency

The reflection efficiency of the field is the amount of irradiation the heliostat can reflect unto the receiver relative to the amount of solar irradiation incident on it.

The primary inputs that drive the heliostat field development are the total power generation capacity intended for the field, and the annual averaged DNI value.

$$Heat\ incident\ on\ receiver = no.of\ heliostats \times area\ of\ heliostats \times average\ \eta_{opt} \quad (4.2)$$

These data inputs, alongside secondary inputs such as the land area, land boundaries and the tower height thus determine the number of heliostats needed in a field and the configuration of the field through a complex algebraic optimization procedure.

Other factors that can be considered include thermal energy storage capacity, however the scope of this work does not cover thermal energy storage applications; and the direct enthalpy of the fluid from the receiver is assumed to be available for power generation.

The receiver heat flux is usually addressed in terms of "heat flux" rather than the total heat quantity. A higher flux receiver is desirable because less heat-exchange area is needed for a given amount of power, and a reduction in area reduces heat loss as well as the cost of the receiver [30]. The flux limit of receivers for central tower power applications are determined based on the material properties (thermal stress and low-cycle fatigue considerations), target fluid exit temperatures, and the fluid properties. State-of-the-art commercial molten salt technologies could operate in flux ranges from about 25W/cm^2 (250 suns) to 100W/cm^2 (1000 suns) [2], [6], [30]. Hence the total area of the receiver is determined by solar power from the heliostats and considerations of the maximum as well as average heat flux incident on the receiver.

This study considers the design of a solar field for 200MW power generation in the Daggett-Barstow region in California. The NREL developed research tool, SolarPILOT, has been utilized for plant development and optimization in this study.

Field Development and Optimization with SolarPILOT

SolarPILOT is a computer software tool that generates a solar thermal field geometry, characterizes the performance of the field—including the optimization of the heliostat field by generating heliostat layout, characterization of the efficiency of the heliostat field and the receiver absorption, and generation of the heat flux maps on the receiver. SolarPILOT implements the Hermite series analytical flux density model on individual heliostats, and also implements the Monte Carlo ray tracing method to provide a more accurate optimal characterization of the heliostat field [20].

A complete description of the mathematical models implemented in SolarPILOT can be found in [20]. This study is intent on performing sectional analysis on the central receiver; hence this section addresses the utilization and implementation of the SolarPILOT model to yield the results that serve as inputs for the numerical simulation of the central receiver.

i. SolarPILOT Simulation Inputs and Optimization

The simulation study in this work took a case study of a hot summer day in Daggett-Barstow, for a parametric study of the solar conditions over a typical day of operation identified from SolarPILOT. The solar field input and optimization is achieved by executing the following steps in SolarPILOT:

1. **Climate/Location:** The location for this simulation was selected to be Daggett-Barstow. The Typical Meteorological Year (TMY) data file for this location was downloaded from SolarPILOT software database to obtain the longitudinal and latitudinal coordinates; hourly data of the Global Horizontal Irradiance (GHI), Direct Normal Irradiance (DNI), Diffuse Horizontal Irradiance (DHI) and the dry bulb temperatures (Tdry) for a subset of the day between 7am and 6pm.

Table 2: TMY data for Daggett-Barstow during a hot summer day in July (source: SolarPILOT software).

Source	Location ID	Time zone	State	Country	Latitude	Longitude		Elevation	City	
TMY3	723815	-8 GMT	CA	USA	34.85	-116.8		586	Daggett Barstow	
Year	Month	Day	Hour	GHI	DNI	DHI	Tdry	Pressure	Wind speed	Wind direction
1989	7	2	7	528	867	59	26.1	946	7.2	310
1989	7	2	8	725	922	72	27.2	946	6.2	310
1989	7	2	9	887	957	82	29.4	946	4.1	290
1989	7	2	10	997	974	88	32.2	946	5.7	300
1989	7	2	11	1048	981	91	33.9	945	4.1	280
1989	7	2	12	1041	982	90	36.1	945	2.6	320
1989	7	2	13	961	961	86	38.9	944	2.6	270
1989	7	2	14	774	847	92	39.4	943	2.1	150
1989	7	2	15	647	868	74	39.4	942	3.1	60
1989	7	2	16	457	819	59	40.6	942	0	0
1989	7	2	17	235	638	48	39.4	942	5.2	220
1989	7	2	18	58	300	28	37.2	942	6.2	240

2. Layout Setup: The layout setup was done by selecting the receiver design power, design-point DNI value, tower height, and selecting the location boundary. This simulation uses the actual location boundary, and thus the software receives any discontinuities in land boundaries that exist in the field. Actual land boundaries can be obtained, for example, from Google Earth Pro software [http://www.google.com/earth/index.html, accessed 22 November, 2020] and imported thereafter to the layout set up for the software to mark the bounds of the heliostat field. To select the heliostat positions in the field, SolarPILOT estimates the annual performance of each heliostat in the field, ranks their performance and selects the most productive heliostats first [20]. SolarPILOT has several methods for tuning parameters to configure the annual performance estimate simulation set—single point simulation,

annual simulation, limited annual simulation, representative profiles, annual efficiency maps and a combination of two different methods—however most of these methods are computationally expensive for the evaluation of field optical performance as they simulate all daytime hours in the year. The method chosen for this simulation is the "Representative profiles" method which generates averaged weather profiles for the selected days, and in which the sun positions used for performance evaluation are a subset of those that occur throughout the year on particular day and hour combinations [20]. For the purpose of spatial and temporal analysis of heat flux impact, a less computationally expensive simulation such as the "representative profiles" method is very effective as demonstrated in layout simulations by Wagner and Wedlin [20].

3. Receiver Geometry: An external cylindrical receiver was used for this study, with dimensions shown in Table 3. The receiver length and diameter are selected to give an area that minimizes spillage of heat flux (shorter lengths and diameters would cause more spillage), and optimizes the allowable peak flux on the receiver (longer lengths and diameters would cause low peak fluxes incident on the receiver, which are lower than the allowable peak flux, thus reducing the thermal efficiency of the receiver.)

Table 3: Receiver geometry input parameters.

Receiver Length(vertical)	10m
Receiver Diameter	7.96m
Receiver absorber area	250m^2
Allowable peak flux	100W/cm^2

4. Field Optimization: SolarPILOT software performs a numerical optimization of the local position of the heliostats as well as the number of heliostats needed in the field for the desired performance criteria of the field. Optimization parameters that can be combined to satisfy a minimized objective

function include the cost of the field, the height of the tower, and the tower position/coordinates relative to solar field land area boundaries (which are termed as horizontal and vertical offsets of the tower). The results from the optimized function are applied to layout inputs that are utilized in the field performance simulation.

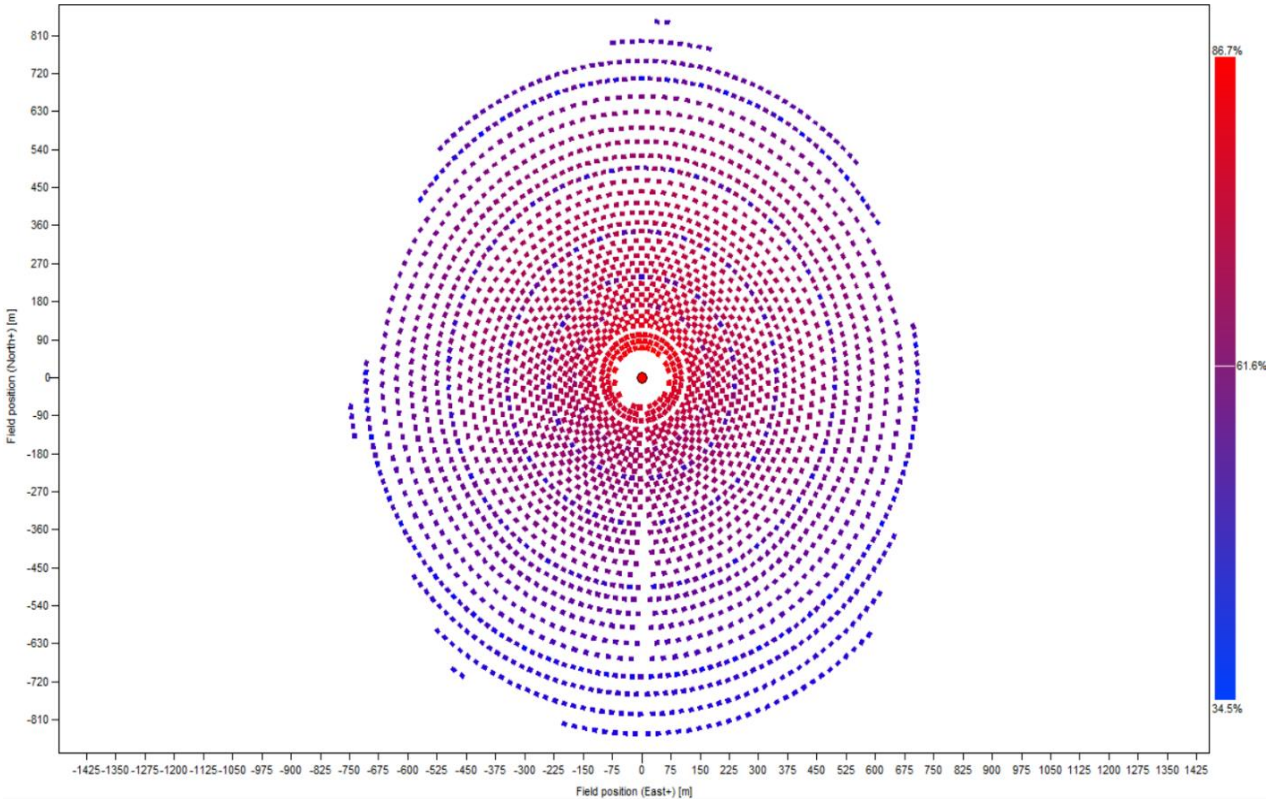

Figure 25: SolarPILOT Heliostat layout after field optimization for Daggett-Barstow field simulation, with the color codes displaying the efficiencies of the individual heliostats.

Figure 25 is a figure of the heliostat field generated by SolarPILOT for the given power generation target and receiver input parameters, with the horizontal and vertical axis showing the field extent (in meters) in the north and east ordinates. To produce this layout, the software generates averaged weather profiles for a select set of days that occur at regularly spaced intervals throughout the year and generates the layout that gives the best annual performance based on the optimization parameters. The red circle in the center indicates the solar power tower which mounts the receiver, and the radial pattern of squares—

colored red and blue—are the heliostats affixed around the central receiver. The figure has the heliostat efficiencies color-coded on the respective heliostats.

From Figure 25, it can be noticed that there is a wide variation in the annual optical efficiencies of the heliostats (which is the average optical efficiency of the heliostats over the select days within the year in which weather conditions are simulated) ranging from 34.5% to 86.7%, with the region around the central tower having a cluster of the highest efficiency heliostats, because these heliostats have the lowest azimuth angles and are closest to the tower—hence lower cosine losses which make up the majority of the efficiency losses in the heliostat fields.

5. **Performance Simulation**: To conduct the study of how the receiver performance is impacted by the field at a given time of the day, an hourly simulation approach was followed. With the optimized field, the performance of the field is conducted by selecting the exact date, month, hour of the day, and the direct normal irradiance (DNI) at the time. The software implements either the Hermite (analytical) simulation or the ray tracing simulation, in addition to calculating the resultant solar azimuth and elevation angle at the given simulation point the flux data. In this study, the simulation for the hourly flux data was conducted for every hour between 07:00 hours and 18:00 hours on the selected summer day.

SolarPILOT Simulation Results

The output from the simulation results gives a summary of the system for the selected simulation time.

Table 4: Flux simulation results summary for a solar noon at DNI value 982W/m^2

	Units	Value
Total plant cost	$	99267920.66
Simulated heliostat area	m^2	318542

Simulated heliostat count	-	2714
Power incident on the field	kW	312808
Power absorbed by the receiver	kW	183192
Power absorbed by the Heat transfer fluid (HTF)	kW	174729
Cloudiness efficiency	%	100
Shading efficiency	%	100
Cosine efficiency	%	78.87
Reflection efficiency	%	90.25
Blocking efficiency	%	97.32
Attenuation efficiency	%	95.04
Image intercept efficiency	%	93.64
Absorption efficiency	%	95.00
Solar field optical efficiency	%	61.65
Optical efficiency (including receiver)	%	58.56
Incident flux	W/cm^2	77.12

Table 4 shows the constituent components that make up the optical field efficiency. The solar field optical efficiency is 65%, and the major draw down in the efficiency is caused by the cosine losses. This summary implies that the heliostat field efficiency is a critical factor that can affect the overall performance of the plant. The cloudiness efficiency in the results is 100% (clear day), however it should be noted that a typical day could have transient clouds. The effect of transient cloudiness is beyond the scope of this work.

In Figure 26 , the output hourly flux maps from solar pilot are shown. In the map abscissa, the eastern coordinate is at $+90^0$, the north at 0^0, the west at -90^0, and the south at -180^0. For example, at 7 hours,

the sun's position is in the east (+90^0), and it is more concentrated on the heliostats in the west of the field. Hence, the receiver region in the west (-90^0) of the field receives the highest concentration of heat flux.

(7hrs)

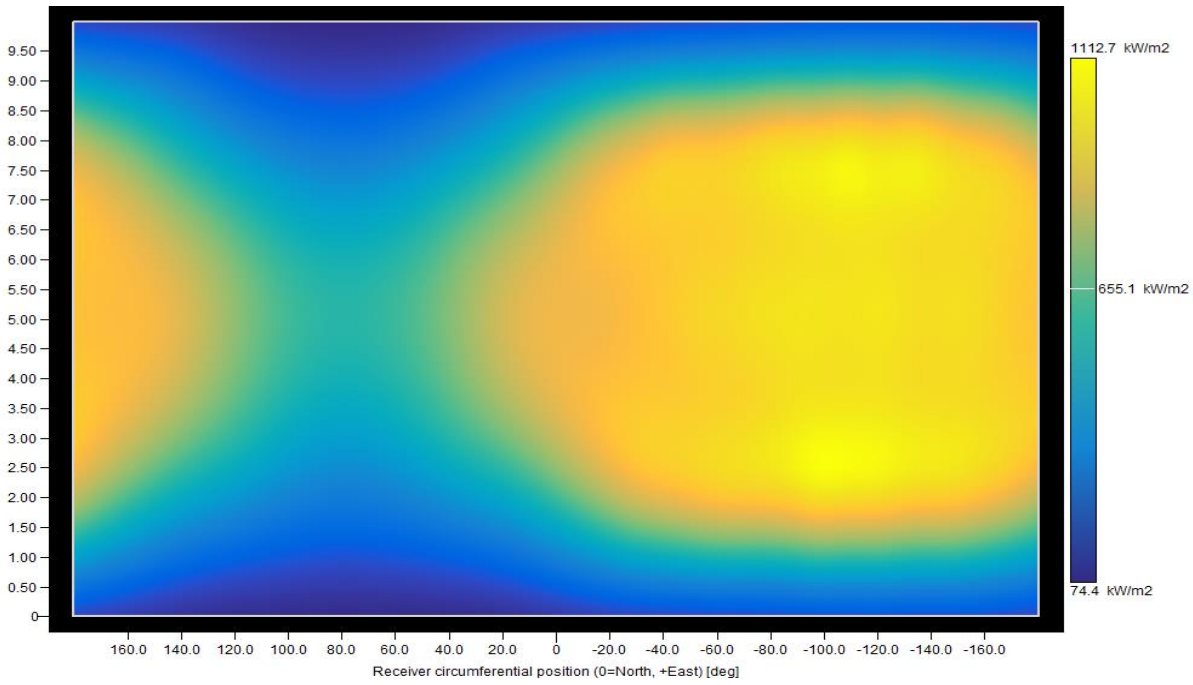

(8hrs)

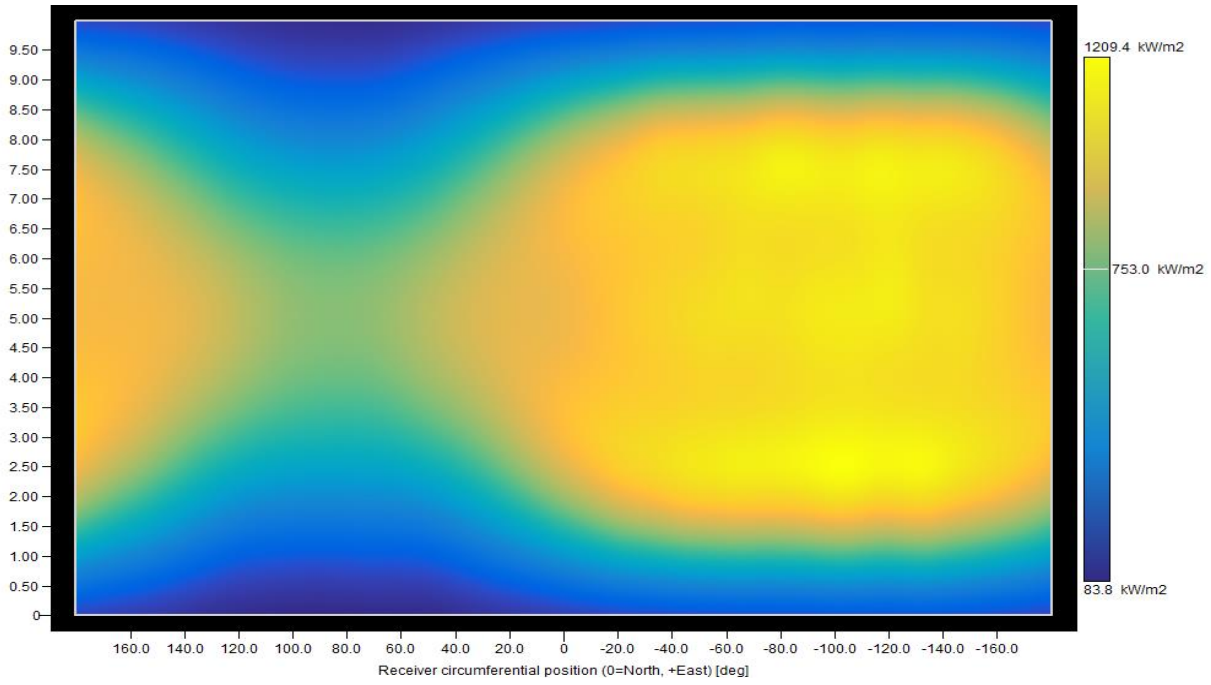
1209.4 kW/m2
753.0 kW/m2
83.8 kW/m2
9.50
9.00
8.50
8.00
7.50
7.00
6.50
6.00
5.50
5.00
4.50
4.00
3.50
3.00
2.50
2.00
1.50
1.00
0.50
0
160.0 140.0 120.0 100.0 80.0 60.0 40.0 20.0 0 -20.0 -40.0 -60.0 -80.0 -100.0 -120.0 -140.0 -160.0
Receiver circumferential position (0=North, +East) [deg]

(9hrs)

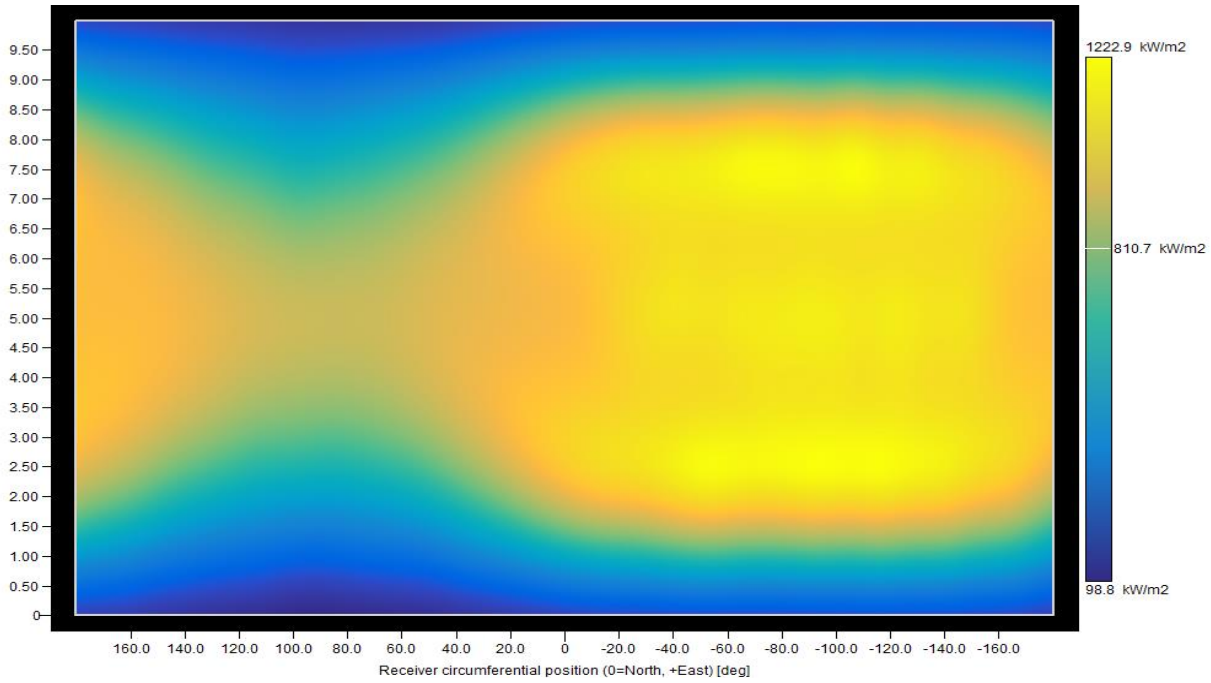
1222.9 kW/m2
810.7 kW/m2
98.8 kW/m2
9.50
9.00
8.50
8.00
7.50
7.00
6.50
6.00
5.50
5.00
4.50
4.00
3.50
3.00
2.50
2.00
1.50
1.00
0.50
0
160.0 140.0 120.0 100.0 80.0 60.0 40.0 20.0 0 -20.0 -40.0 -60.0 -80.0 -100.0 -120.0 -140.0 -160.0
Receiver circumferential position (0=North, +East) [deg]

(10hrs)

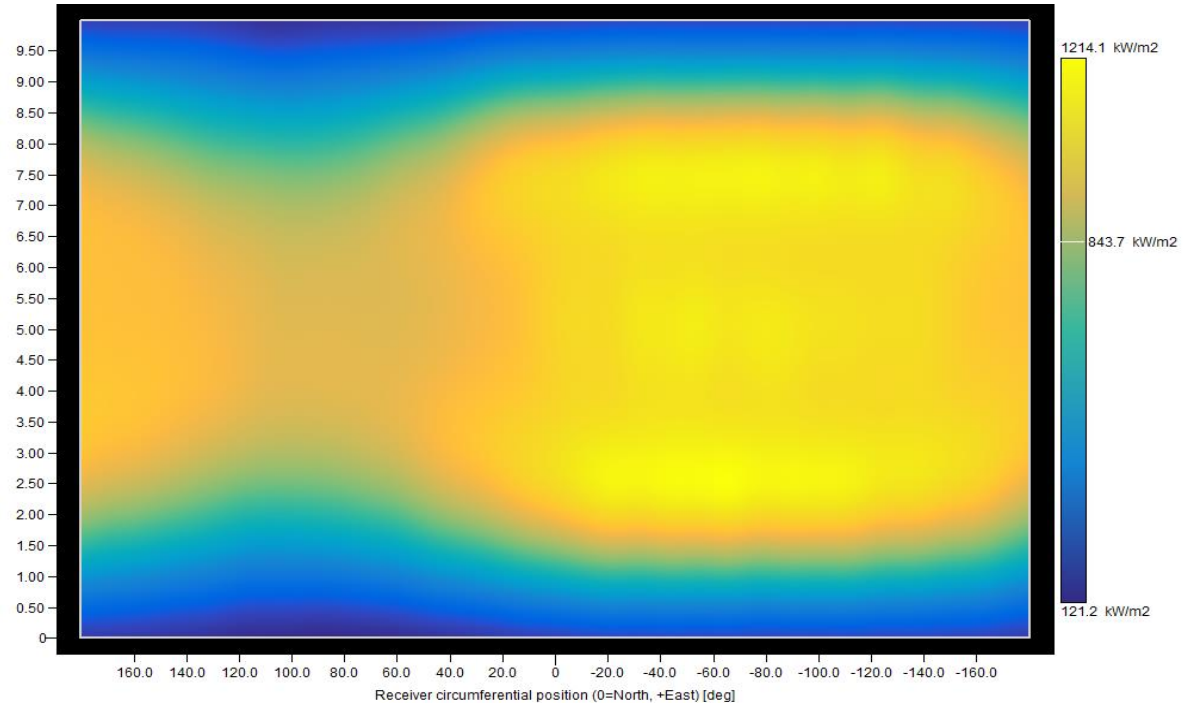
1214.1 kW/m2
843.7 kW/m2
121.2 kW/m2
9.50
9.00
8.50
8.00
7.50
7.00
6.50
6.00
5.50
5.00
4.50
4.00
3.50
3.00
2.50
2.00
1.50
1.00
0.50
0
160.0 140.0 120.0 100.0 80.0 60.0 40.0 20.0 0 -20.0 -40.0 -60.0 -80.0 -100.0 -120.0 -140.0 -160.0
Receiver circumferential position (0=North, +East) [deg]

(11hrs)

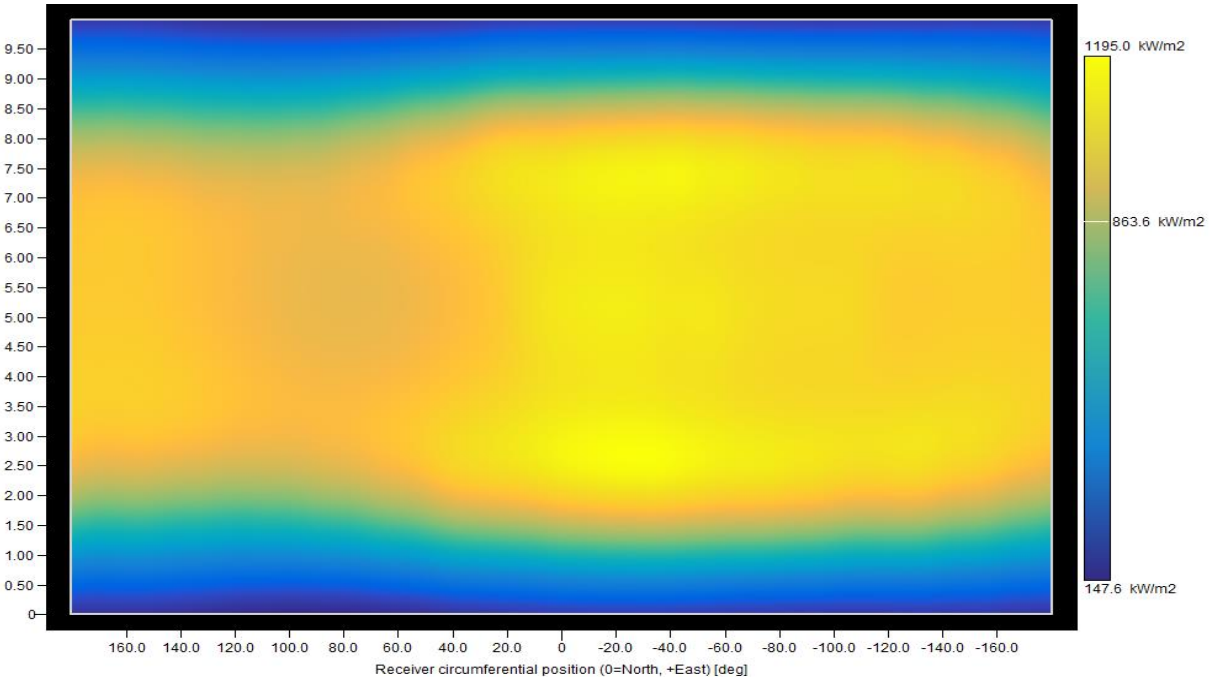
1195.0 kW/m2
863.6 kW/m2
147.6 kW/m2
9.50
9.00
8.50
8.00
7.50
7.00
6.50
6.00
5.50
5.00
4.50
4.00
3.50
3.00
2.50
2.00
1.50
1.00
0.50
0
160.0 140.0 120.0 100.0 80.0 60.0 40.0 20.0 0 -20.0 -40.0 -60.0 -80.0 -100.0 -120.0 -140.0 -160.0
Receiver circumferential position (0=North, +East) [deg]

(12hrs)

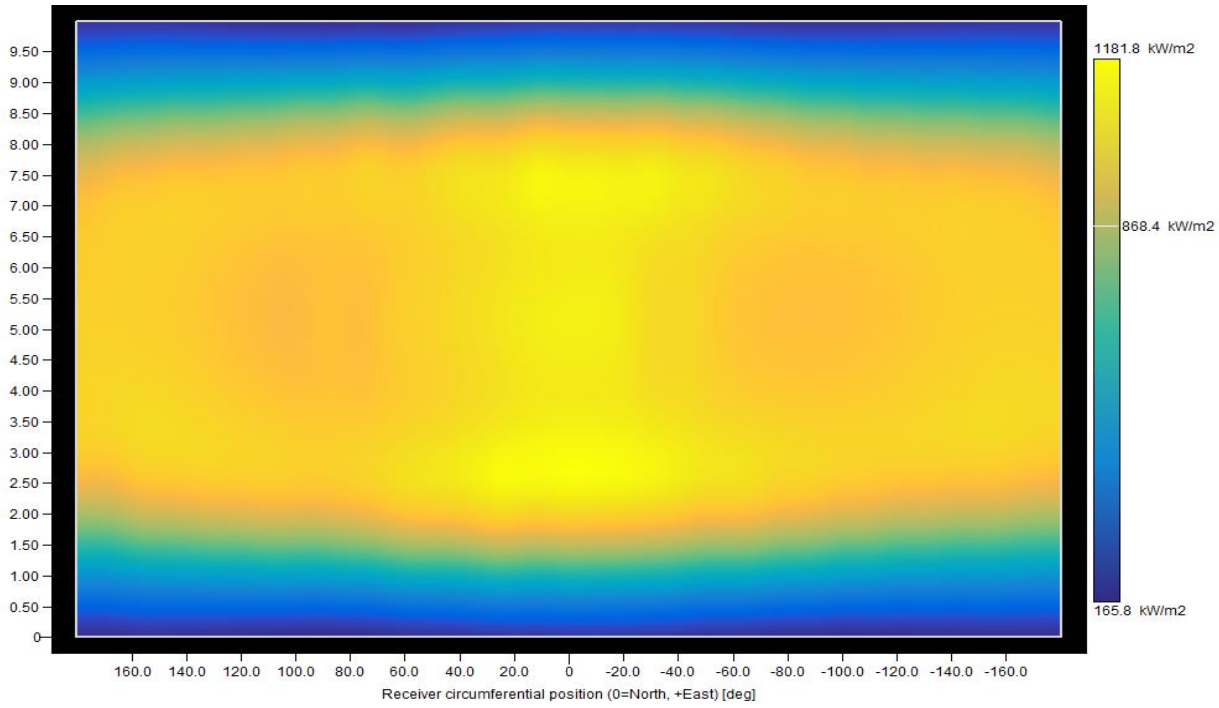
9.50
9.00
8.50
8.00
7.50
7.00
6.50
6.00
5.50
5.00
4.50
4.00
3.50
3.00
2.50
2.00
1.50
1.00
0.50
0
1181.8 kW/m2
868.4 kW/m2
165.8 kW/m2
160.0 140.0 120.0 100.0 80.0 60.0 40.0 20.0 0 -20.0 -40.0 -60.0 -80.0 -100.0 -120.0 -140.0 -160.0
Receiver circumferential position (0=North, +East) [deg]

(13hrs)

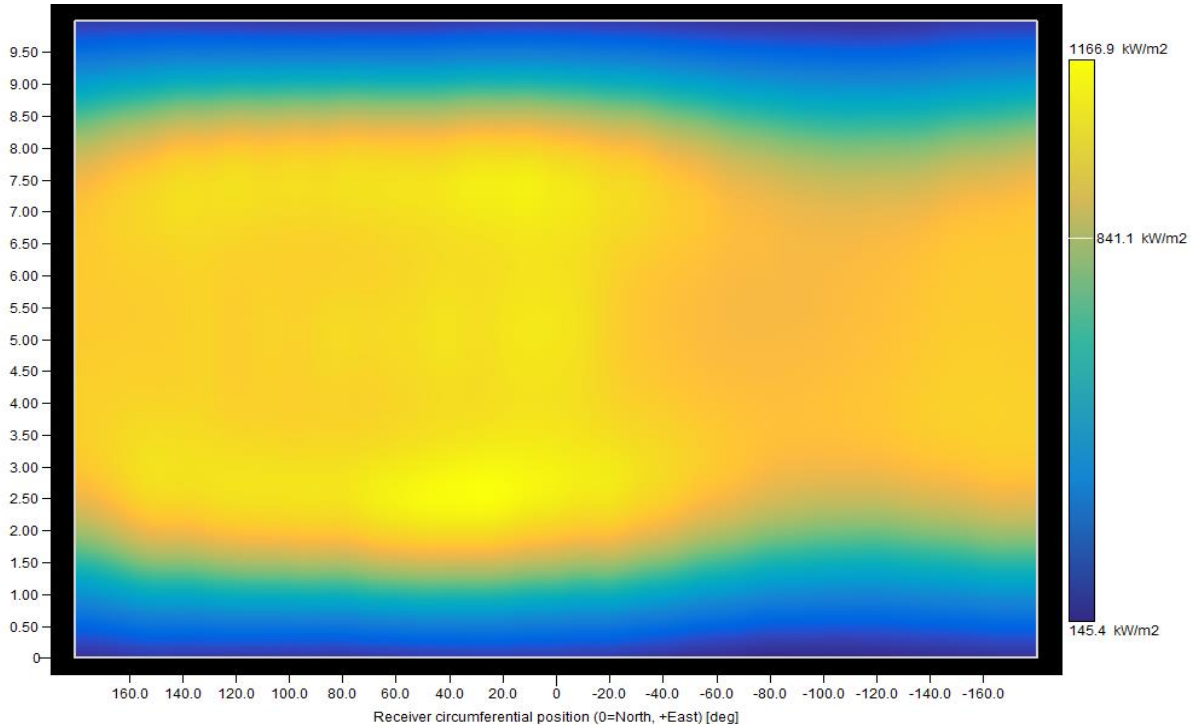
9.50
9.00
8.50
8.00
7.50
7.00
6.50
6.00
5.50
5.00
4.50
4.00
3.50
3.00
2.50
2.00
1.50
1.00
0.50
0
1166.9 kW/m2
841.1 kW/m2
145.4 kW/m2
160.0 140.0 120.0 100.0 80.0 60.0 40.0 20.0 0 -20.0 -40.0 -60.0 -80.0 -100.0 -120.0 -140.0 -160.0
Receiver circumferential position (0=North, +East) [deg]

(**14hrs)**

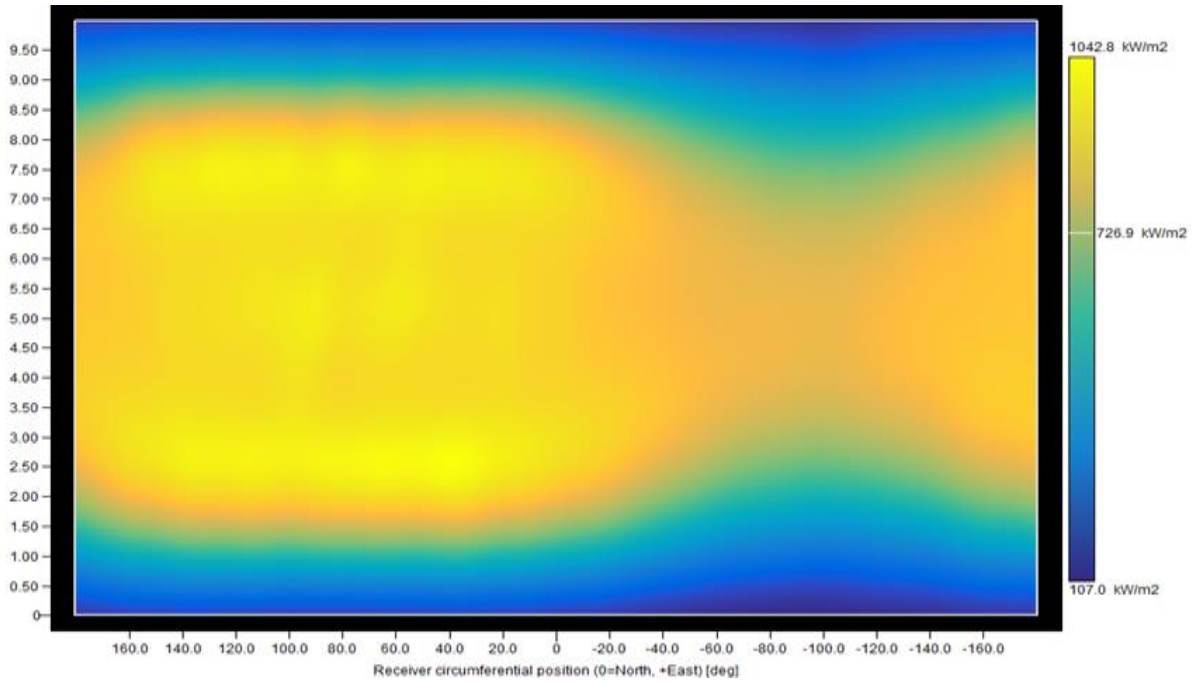
1042.8 kW/m2
726.9 kW/m2
107.0 kW/m2
9.50
9.00
8.50
8.00
7.50
7.00
6.50
6.00
5.50
5.00
4.50
4.00
3.50
3.00
2.50
2.00
1.50
1.00
0.50
0
160.0 140.0 120.0 100.0 80.0 60.0 40.0 20.0 0 -20.0 -40.0 -60.0 -80.0 -100.0 -120.0 -140.0 -160.0
Receiver circumferential position (0=North, +East) [deg]

(**15hrs)**

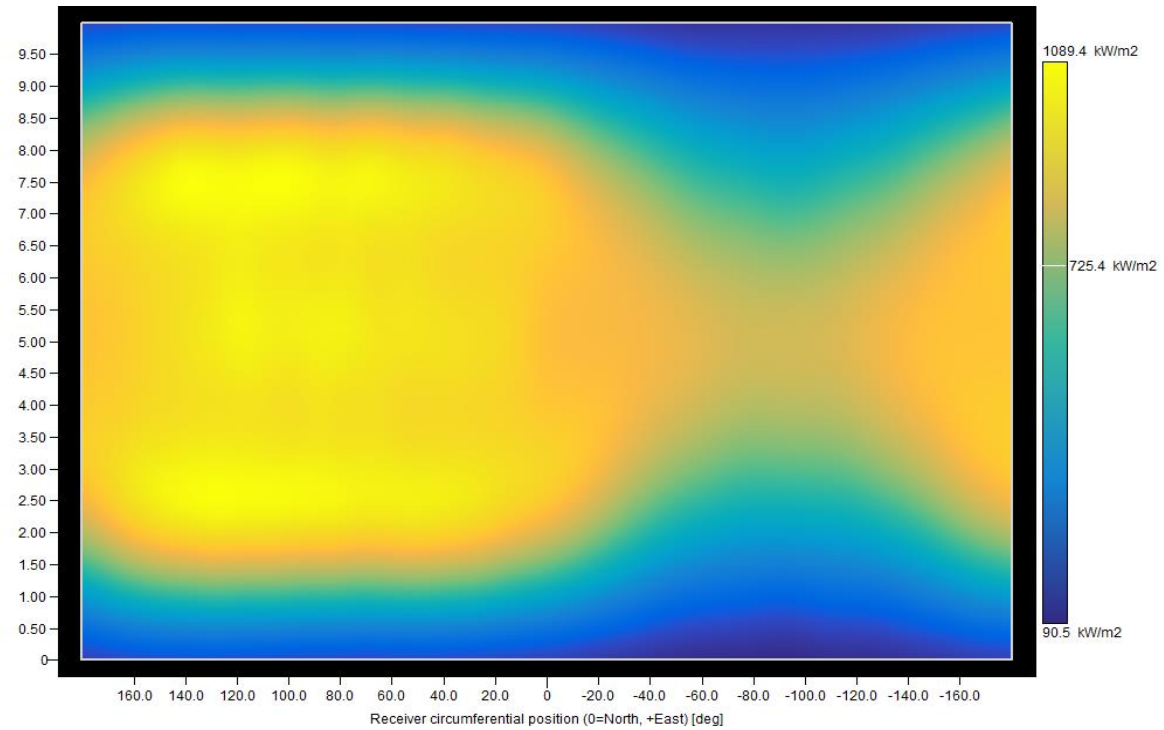
1089.4 kW/m2
725.4 kW/m2
90.5 kW/m2
9.50
9.00
8.50
8.00
7.50
7.00
6.50
6.00
5.50
5.00
4.50
4.00
3.50
3.00
2.50
2.00
1.50
1.00
0.50
0
160.0 140.0 120.0 100.0 80.0 60.0 40.0 20.0 0 -20.0 -40.0 -60.0 -80.0 -100.0 -120.0 -140.0 -160.0
Receiver circumferential position (0=North, +East) [deg]

(16hrs)

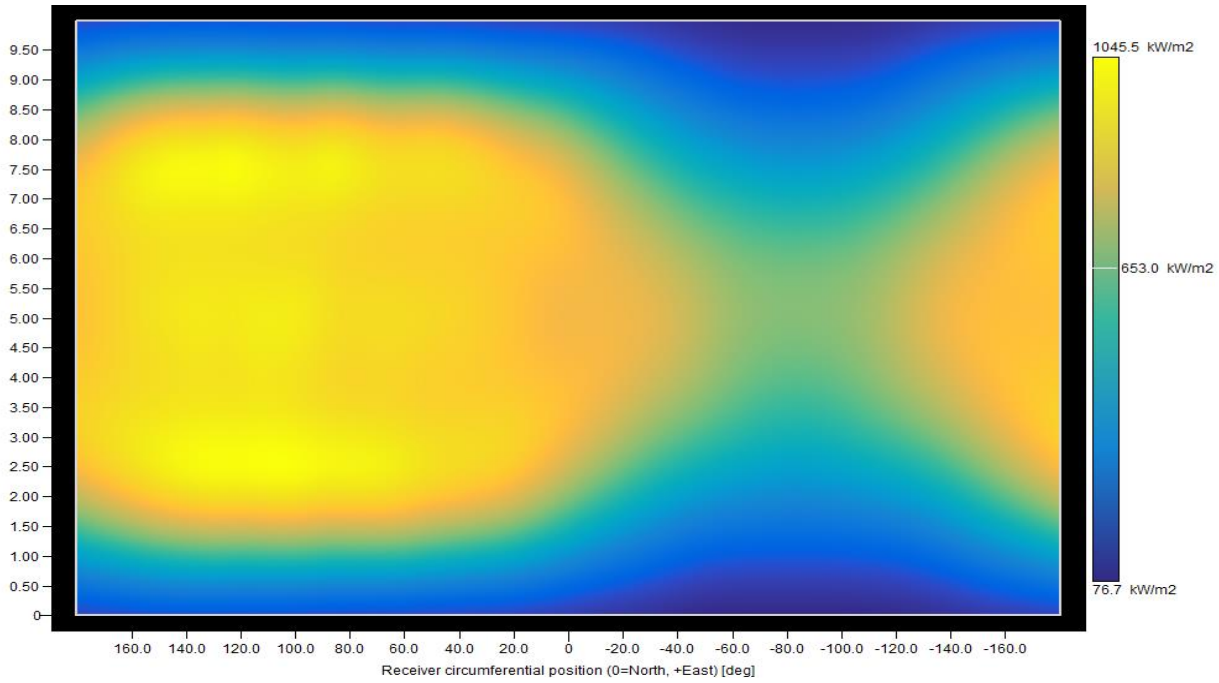
9.50
9.00
8.50
8.00
7.50
7.00
6.50
6.00
5.50
5.00
4.50
4.00
3.50
3.00
2.50
2.00
1.50
1.00
0.50
0
1045.5 kW/m2
653.0 kW/m2
76.7 kW/m2
160.0 140.0 120.0 100.0 80.0 60.0 40.0 20.0 0 -20.0 -40.0 -60.0 -80.0 -100.0 -120.0 -140.0 -160.0
Receiver circumferential position (0=North, +East) [deg]

(17hrs)

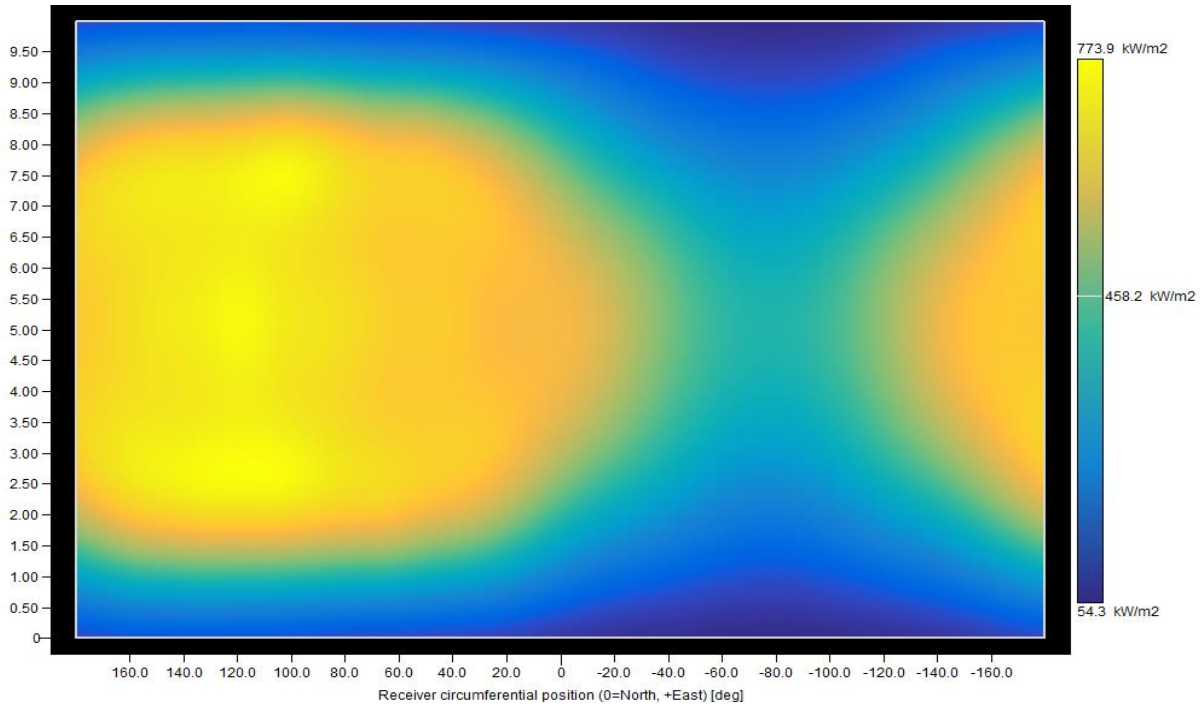
9.50
9.00
8.50
8.00
7.50
7.00
6.50
6.00
5.50
5.00
4.50
4.00
3.50
3.00
2.50
2.00
1.50
1.00
0.50
0
773.9 kW/m2
458.2 kW/m2
54.3 kW/m2
160.0 140.0 120.0 100.0 80.0 60.0 40.0 20.0 0 -20.0 -40.0 -60.0 -80.0 -100.0 -120.0 -140.0 -160.0
Receiver circumferential position (0=North, +East) [deg]

(18hrs)

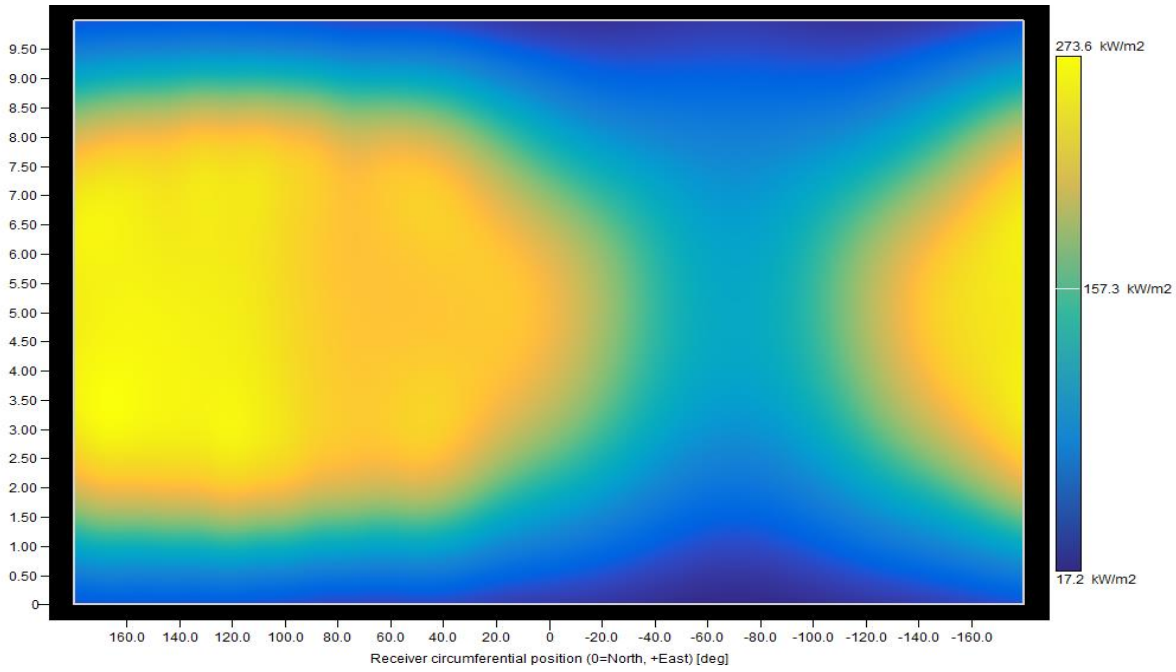

Figure 26: SolarPILOT flux maps for several times (sun positions) in the simulated day.

Figure 26 shows the evolution of the sun's relative position to the central receiver field throughout the day. The results show that the heat distribution over a uniform receiver is spatially and temporally non-uniform. Hence it is important to assess the combined effect of spatial and temporal non-uniformity in the flux distribution on the performance of the receiver.

Unit Cell And Module Integration

The micro-pin-array receiver (MPAR) has been described as being composed of unit cells which are combined in parallel to form a module. In the previous chapter, a performance characterization of two different unit cell receivers were made (AM^{2}PAR [16.6cm flow length section], and µLPAR receiver [3.3cm flow length section]), in which the AM^{2}PAR receiver was noted to have the advantage of being longer for a similar thermal and hydraulic performance between both receivers.

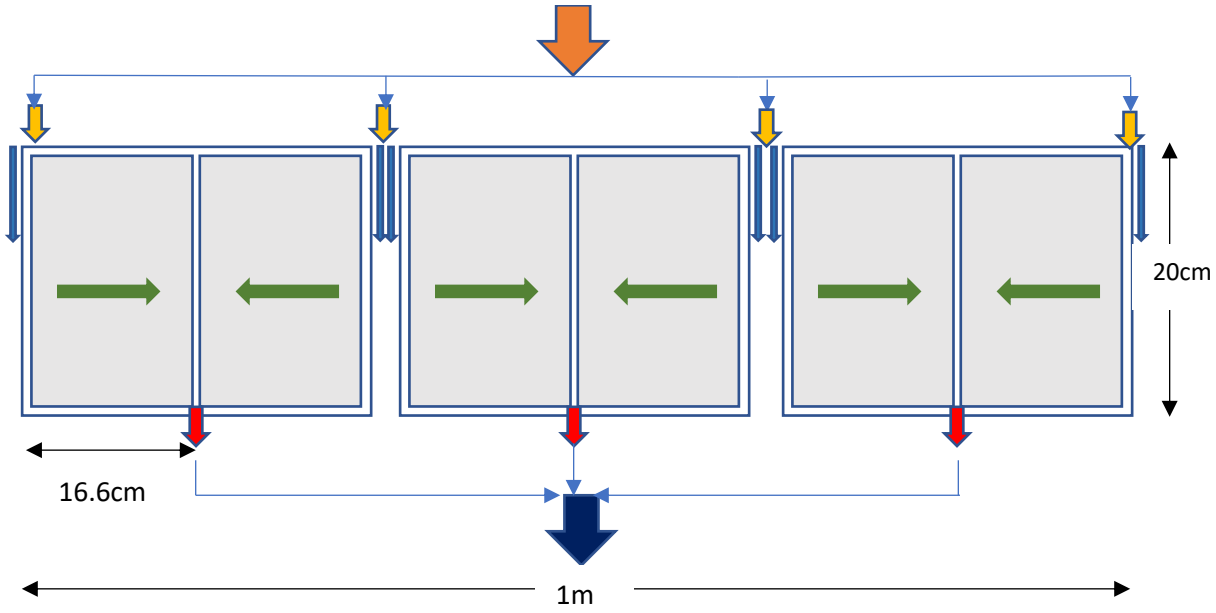

Figure 27: Sketch of the unit cell pin arrays combined to form a ~1m long by 0.2m wide module.

Hence, the central tower external receiver in cylindrical form will be made of several AM^{2}PAR modules connected in parallel. Modularization of the receiver is dependent on the header design constraints and the manufacturability constraints available. In addition, the number of headers that collect flow from the unit cells is preferred to fewer (about 3) so as to reduce the system complexity.

As calculated in the previous chapter, the flow section length for the desired pressure drop in the additively manufactured receiver is 16.6cm, hence a module which contains 3 unit cells will have a length of approximately 1m (Figure 27). Hence the module of the external receiver has an area of 0.2m x 1m. For a 250m^2 total receiver area, the central receiver will be made up of 1250 modules. The module width used in this study is 0.2m; it must however be highlighted that rapid advancement in additive manufacturing is making the module sizes larger, and modules can be manufactured with 0.5m widths. The advantage of this modular arrangement is that the pressure drop is drastically reduced as the flow divides into parallel sections resulting in a lower flow rate within smaller length sections. Another advantage of this modular

arrangement is that each module can be designed with variable pin dimensions if needed; the need for such a location-specific design will be made clear in the following chapter.

Numerical Modelling Parameters

In solving for the thermal and hydraulic performance of the receiver, the receiver is discretized into 900 x 250 grid sections in SolarPILOT to account for an even determination of the property evolution within the receiver, whilst maintaining computational efficiency. The heat maps (Figure 26) demonstrate more variability in vertical section than in horizontal section, and hence one would reason that more nodal points should be in the vertical section. However, the flow in the receiver is in the horizontal section and thus there is more interest in the sectional change of the flow within such short length span as the fluid and surface temperature changes in a range of about 150°C. The flux output result from SolarPILOT is used as a heat flux input parameter in the code to solve for the thermal and hydraulic characterization of the flow.

The flow over the receiver is modelled after the flow over a cylinder for the purpose of addressing forced convection currents. Given the receiver diameter of 7.96m, and an average windspeed of 5.7m/s in the considered case study, the Reynolds' number is 9.95×10^5, which places the flow in a turbulent regime. Hence an average heat transfer coefficient for external convention can be assumed over the surface of the receiver. Heat loss from the receiver is largely due to radiation (estimated 90% of total loss) and minimally due to convection (estimated 10% of the total heat loss) at a wide range of practical windspeeds; hence not much accuracy is lost nevertheless by estimating an averaged heat transfer coefficient over the receiver surface.

The flow chart in Figure 28 describes the numerical sequence for solving the flow in the discretized micro-pin array central receiver. The code simulates a single inlet flow line that brings sCO_2 at an inlet temperature of 550°C into all module headers, and into the unit cells before collecting at the outlet

module headers. It is assumed that the pressure drop across the entire central receiver should not exceed at a fixed value of 4 bar (2% of a 200 bar line pressure). In this study, the flow into parallel modules and unit cells will not have the same outlet temperature for the following reasons:

1. The mass flow rate will be different across the unit cells.
2. The heat flux is distributed non-uniformly over the surface of the receiver.

The temperature realizable at the outlet of the receiver is a function of the pressure drop, which is directly correlated to the fluid flow rate. At high flow rates, and hence high pressure drops, the temperature change of the fluid for the same heat flux is lower. Therefore, the code tunes the pressure drop—by increasing or decreasing—until the target outlet fluid temperature of 720^{o}C is reached. As a result of the overall non-uniformity of flow rates and flux over the receiver, some modules will have exit temperatures less than 720^{o}C and some modules will have exit temperatures greater than 720^{o}C.

To summarize, this section has shown the development of a Solar thermal power plant with SolarPILOT, for a power generation capacity of about 250MW. The heat flux maps have been generated for a typical summer day in Daggett-Barstow, which will be imposed on the cylindrical AM^{2}PAR receiver. The numerical algorithm presented in the flow chart is used to obtain operational parameters such as the surface temperature distribution, fluid temperature distribution, and thermal efficiencies, at the various operating hours of the receiver. The results are presented in the next chapter and are explored to understand the feasibility of solar power generation with the AM^{2}PAR external receiver and the impact of spatial and temporal variation of solar flux on the receiver.

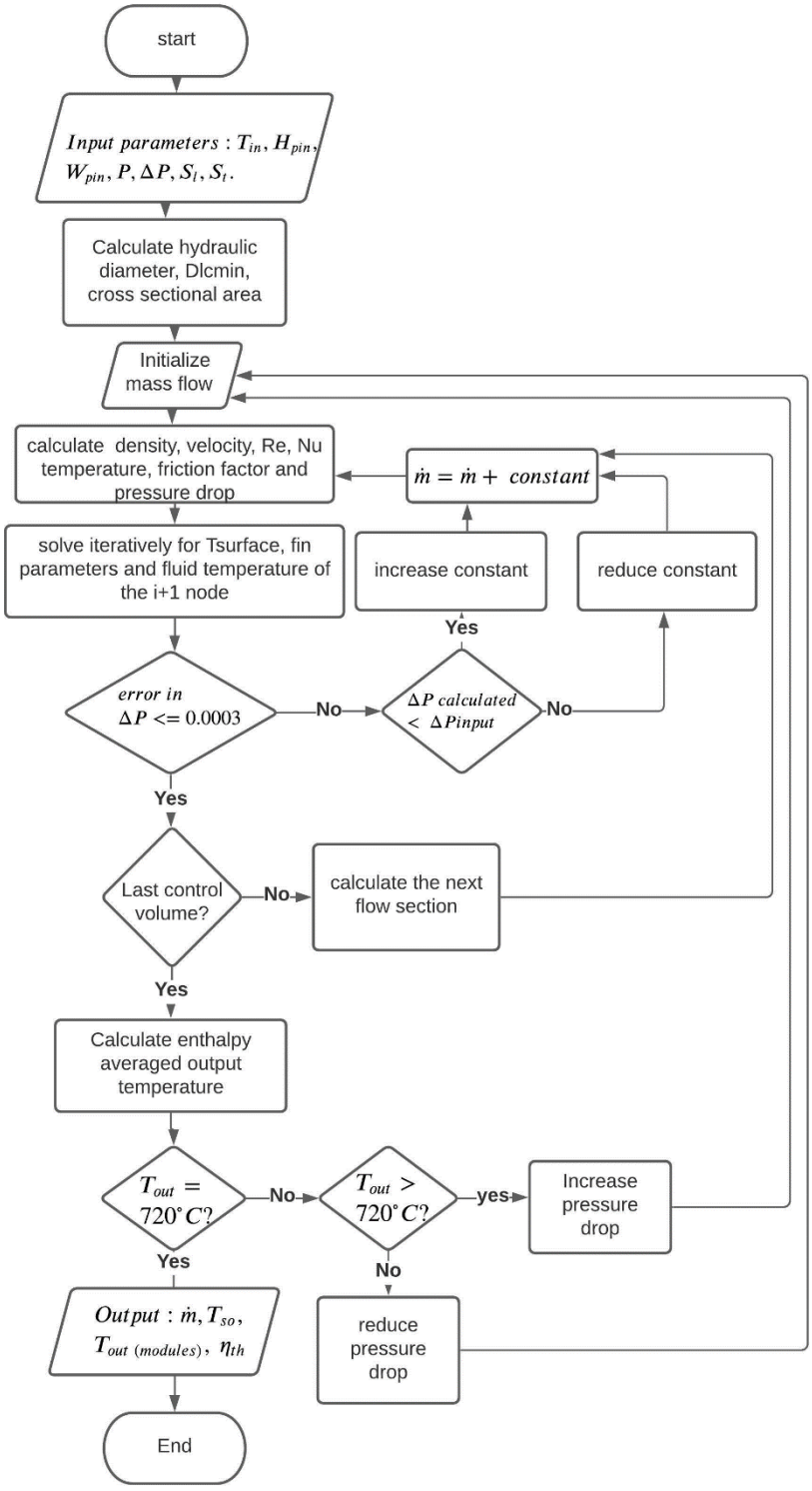

Figure 28: Flow chart showing the numerical sequence of solving the micro-pin array external receiver with a target output temperature of 720°C.

CHAPTER 5
CENTRAL RECEIVER SIMULATION RESULTS AND DISCUSSION

The practical application of the micro-pin-array receiver is subject to its performance under spatially and temporally varying insolation. This variation necessitates the study of the micro-pin-array receiver performance subject to varying heat flux conditions. The performance of the central receiver can be represented with descriptive parameters such as efficiency, fluid outlet temperature etc. In Chapter 4, a solar field layout was generated and characterized using SolarPILOT, and a heat flux map was generated on the central receiver; a numerical code was implemented to solve for the characterization of the sCO_2 AM^2PAR receiver performance. This study presents the simulation results and seeks to understand the thermal and fluid dynamics within sections of the receiver under the varying heat loading conditions, to understand the crucial design and operation parameters for the successful implementation of the micro-pin-array receiver in a CSP field.

Solar Flux Impact on the Surface Temperature and Efficiency (Spatial and Temporal)

As the sun's azimuth angle varies during the day, the concentration of heat flux from the heliostat field on the solar receiver varies. The flux maps obtained from SolarPILOT (Figure 26) are imposed as the heat flux boundary conditions in the numerical model of the central receiver to obtain information on the distribution of important parameters such as surface temperature, pressure drop, and efficiency for the central receiver. Simulations were conducted for a receiver with uniform dimensions as represented in Table 5.

Table 5: Receiver structural and fluid operating parameters for numerical simulation

Parameter	**Value**
Operating Pressure	192 bar
Fluid Inlet Temperature	550 °C

Fluid outlet Temperature	720 °C
Receiver Top Layer thickness	0.4 mm
Unit cell pin height	1.8 mm
Unit cell pin diameter	1.2 mm
Longitudinal pitch	2.13 mm
Transverse pitch	2.46 mm
Unit cell width	20 cm
Unit cell pin array length	16.6 cm
Number of unit cells in a module	3 (2 flow units per unit cell)
Module length (2 flow units * number of unit cells)	99.7cm
Number of modules in receiver	1250

In the first simulation case, the receiver of 1250 modules is modelled with uniform dimensions throughout (height of pin array, width of pin array, length of pin array and pin dimension. For the case study summer day in July, simulations were run with the representative flux profiles from 07:00 hours to 18:00 hours.

In Figure 29, the solar flux, module maximum temperatures, and the efficiency heat maps of the receiver are shown in 2-hour intervals. The resulting profiles have been represented with their cardinal point coordinates with the cylindrical external receiver unfolded into a sheet. Each row of the map represents a time-of-the-day simulation. The flux map on the left column in Figure 29 represents the map of flux on all the grids of the receiver obtained from SolarPILOT simulations (see Chapter 4, Figure 26). The maximum module surface temperature (middle plot) however does not represent the entire grid; it rather is a map

of maximum temperatures that occur in each of the 1250 modules. The module efficiency (right plot) likewise represents a map of the average efficiency of all the modules at the given time intervals.

Interestingly, the maximum temperature map closely follows the flux map because the maximum surface temperatures as well as the maximum fluid temperature from a module have a direct proportionality to the heat incident upon the receiver if there is no significant maldistribution from the headers. As shown in Figure 30, which represents a mapping of the mass flow distribution throughout the receiver, the fluid flow through the receiver is highly uniform without considering effects of flow maldistribution due to header design. The fluid flow is slightly higher (about 7% calculated) in regions of lower temperatures because the fluid in these regions has lower viscosity, resulting in higher fluid flow for the same imposed pressure drop as the regions with higher surface temperatures.

Accordingly, the efficiency maps of the modules (third column) of Figure 29 have a similar distribution to the heat flux and temperature maps, with low efficiencies in the outer region with lower heat fluxes. These low efficiencies observed are because while the surface temperatures are lower than the average by about 10% (temperatures in kelvin), the heat absorbed by the fluid (q_{fluid}) in these regions is reduced even further; hence the reduction in q_{fluid} is far more significant than the reduction in heat loss (q_{loss}). Thus, the heat loss (due to convection and radiation) contributes significantly to the efficiency of the modules in sections with low heat regardless of the lower operating surface temperatures.

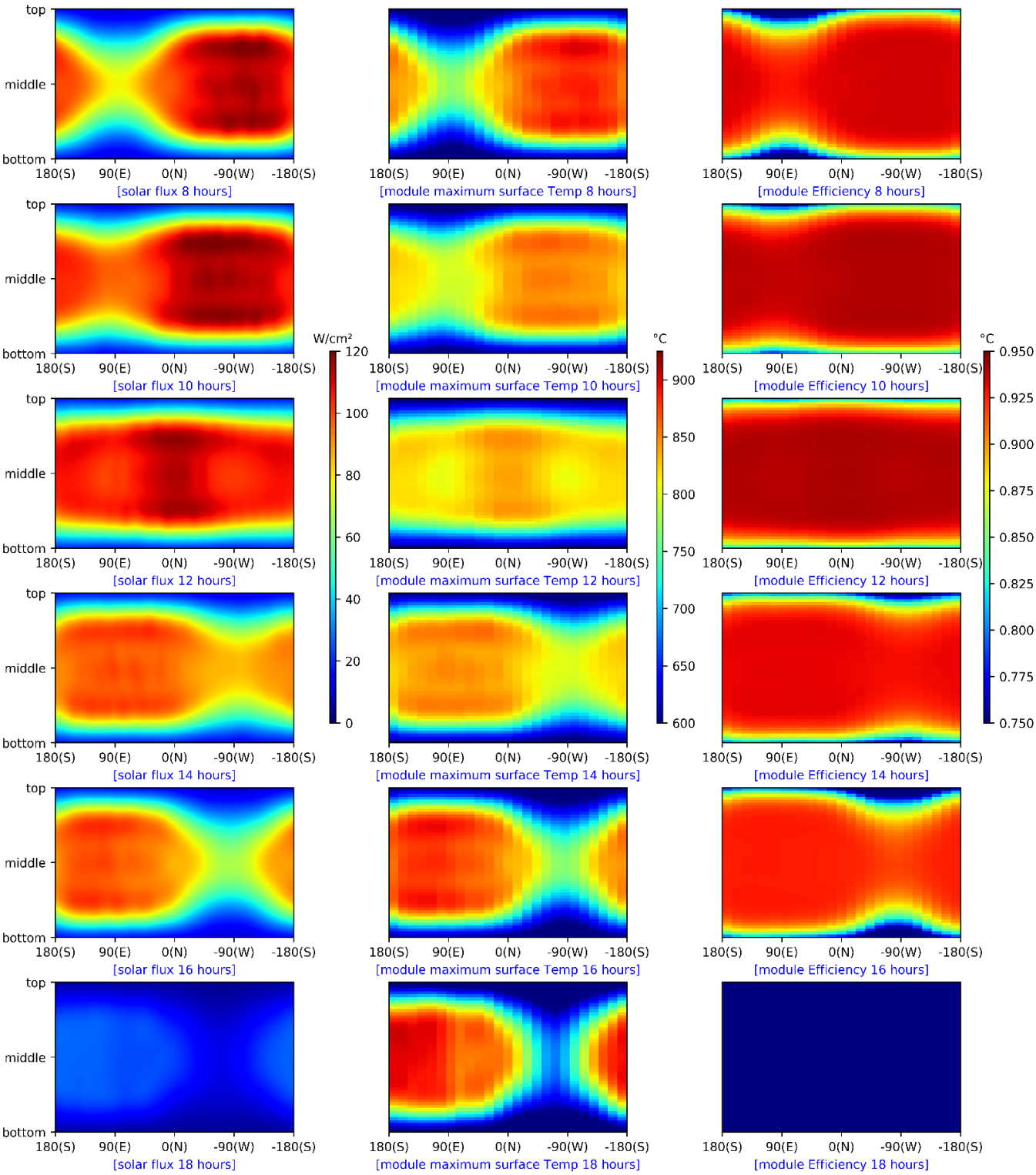

Figure 29: heat maps of solar flux (left column) maximum module surface temperatures (middle) and module efficiency (right column) between 8 hours and 18hours.

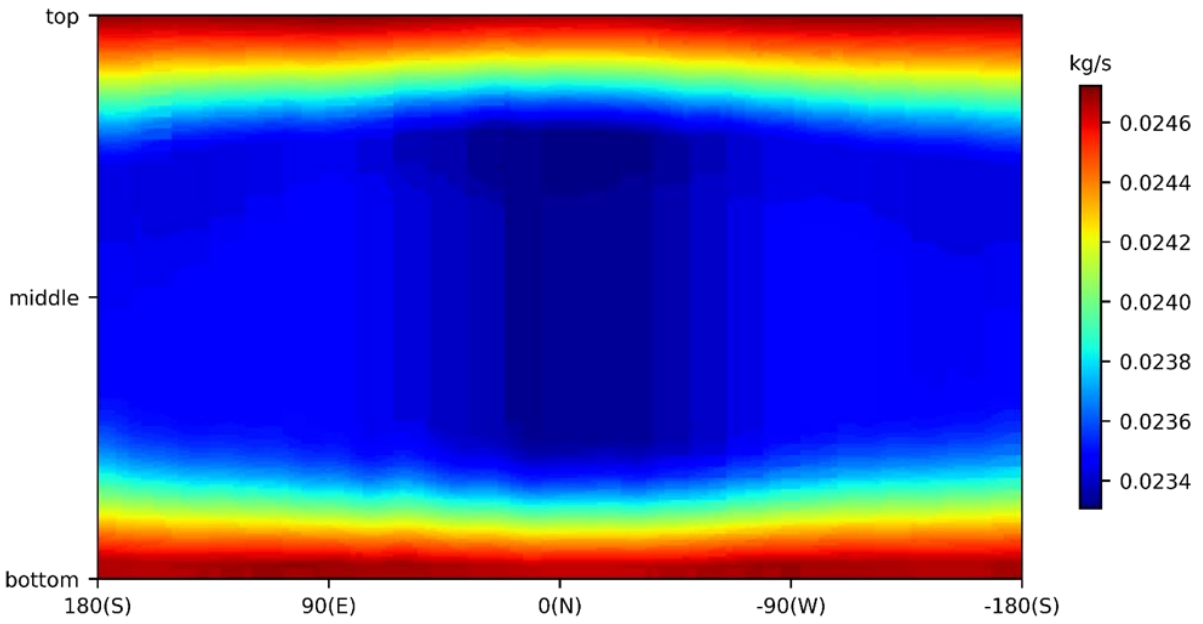

Figure 30: map of mass flow of sCO_2 in each grid row of the unit cell

Fluid and surface temperature distribution at solar noon

A case study of solar noon is of great interest because the solar irradiation on the earth's surface is most intense around that time of the day. The plots in the preceding section have shown the maximum temperatures obtained in the modules of the receiver, and Figure 31 shows the surface temperature distribution over the entire receiver surface. The pattern of the surface temperature distribution is not very perceptible because there is large variation between short flow regions. The continuous gradient between inlet and outlet fluid temperatures over the 1250 modules establishes a similar variation in the surface temperature patterns.

In Figure 32, the map of the outlet temperature of the fluid from each module is shown. The map of outlet temperature shows a similar pattern to the flux map—as higher heat input leads to more temperature rise in the fluid. The receiver thus has sections with outlet temperatures as low as 575˚C in the outer top and bottom regions, and sections with outlet temperatures as high as 800°C in the central regions, to produce an average fluid outlet temperature of 720°C. This wide temperature variation is a significant impact

resulting from the spatial non-uniformity of flux on the central receiver surface. Such uneven temperature distribution can have adverse effects on the creep life of the receiver at the high temperature locations.

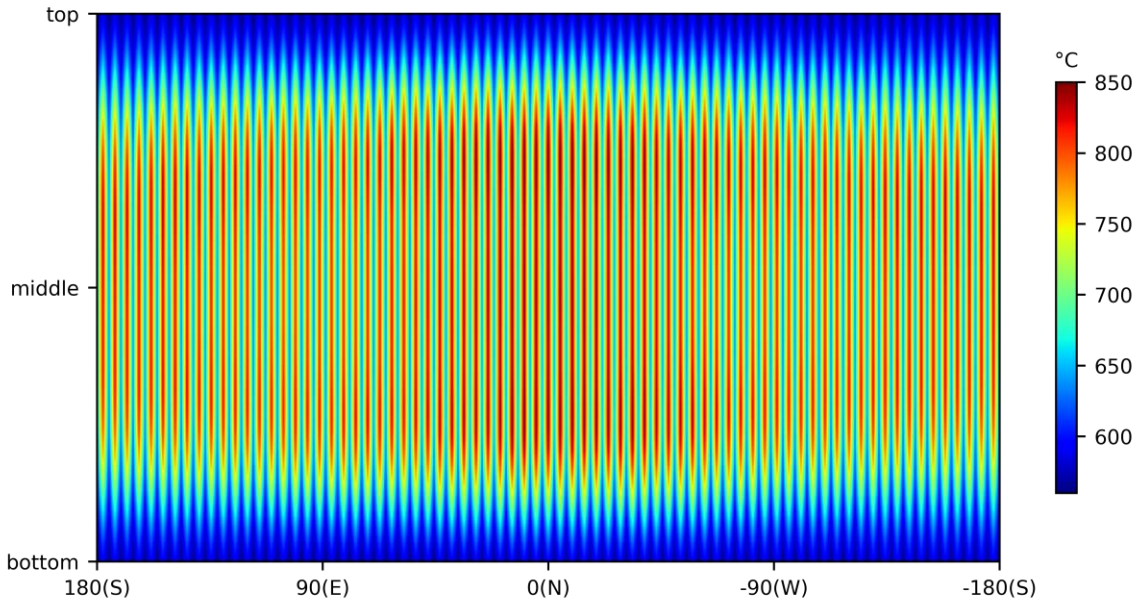

Figure 31: Surface temperature distribution over the receiver at solar noon on a hot summer day.

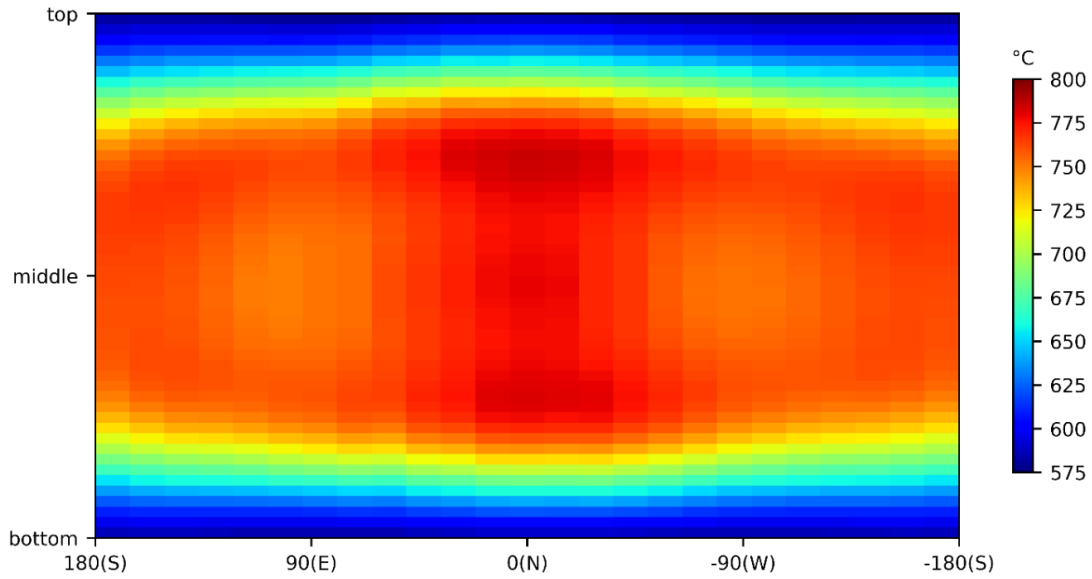

Figure 32: Map of fluid outlet temperatures from each of the 1250 modules simulated ranging from 575^{0}C to 800°C for solar noon for a bulk fluid outlet temperature of 720°C.

Analysis of the Impact Of Non-Uniform Flux Distribution on the AM^{2}PAR Central Receiver

To understand the impact of the non-uniform heat flux on a central receiver surface, a benchmark case study has been defined as "ideal case". To obtain the ideal case, the flux distribution for the hot summer day is averaged to get the mean flux on the receiver at every simulated hour. This mean flux is imposed on the receiver, and the outlet temperature from all 1250 modules will hence be the same. The ideal case thus has a uniform flux on the receiver which is about 70% of the peak flux of the non-uniform flux distribution at the same case study hour. The heliostat field is optimized for noon time and hence the flux distribution over the receiver is the most uniform at that time. In both the ideal and the real receiver ("UPH_AM^{2}PAR" implying that all pins have a uniform pin height) scenario, the mass flow rate is iterated to provide the same target temperature of the fluid of 720^{o}C for an inlet fluid temperature of 550 ^{o}C at all hours.

Figure 33 is a plot showing how the maximum surface temperatures and the thermal efficiencies compare for the ideal case and the real receiver (UPH_AM^{2}PAR) over the fluxes at the simulated hours. In Figure 33, the variation between hours of the maximum surface temperature in the ideal case is about 40°C which is nearly half the variation between hours of the maximum surface temperatures in the UPH_AM^{2}PAR. The wide variation between the maximum surface temperatures in the ideal case and the real case is also observed: the minimum hourly difference between the surface temperatures, which occurs at noon, is 75^{0}C. The thermal efficiency of the receiver is always also higher in the ideal case because the effect of radiation losses is reduced with a more uniform heat distribution on the receiver. However, the efficiency difference between both cases is 13.19% at the minimum thermal efficiencies (mean flux of 16W/cm^2 at 6pm), and 0.75% at the maximum thermal efficiency (mean flux of 86.8W/cm^2 at 12pm). In summary, the ideal case in Figure 33 demonstrates that the major impact of the non-uniform distribution of flux on the receiver is in the peak surface temperatures in addition to a reduction in efficiency.

In Figure 34, the hydraulic performance of the receiver in both cases is compared. The mass flow rates through the receiver and the pressure drops across the micro-pin-arrays to cause the inlet fluid to rise from a temperature 550°C to 720°C are compared. A strong overlap exists between the pressure drop and mass flow curves for both cases, with the slight variations in both curves—the mean difference in pressure drop between both curves is 3.1%, which is a lower magnitude compared to the maximum surface temperature difference in Figure 33 . The plot infers that the power requirement to gain the desired pressure drop is the same in both cases, thus strengthening the point of the maximum surface temperature being the major consequence of the solar flux non-uniformity over the receiver.

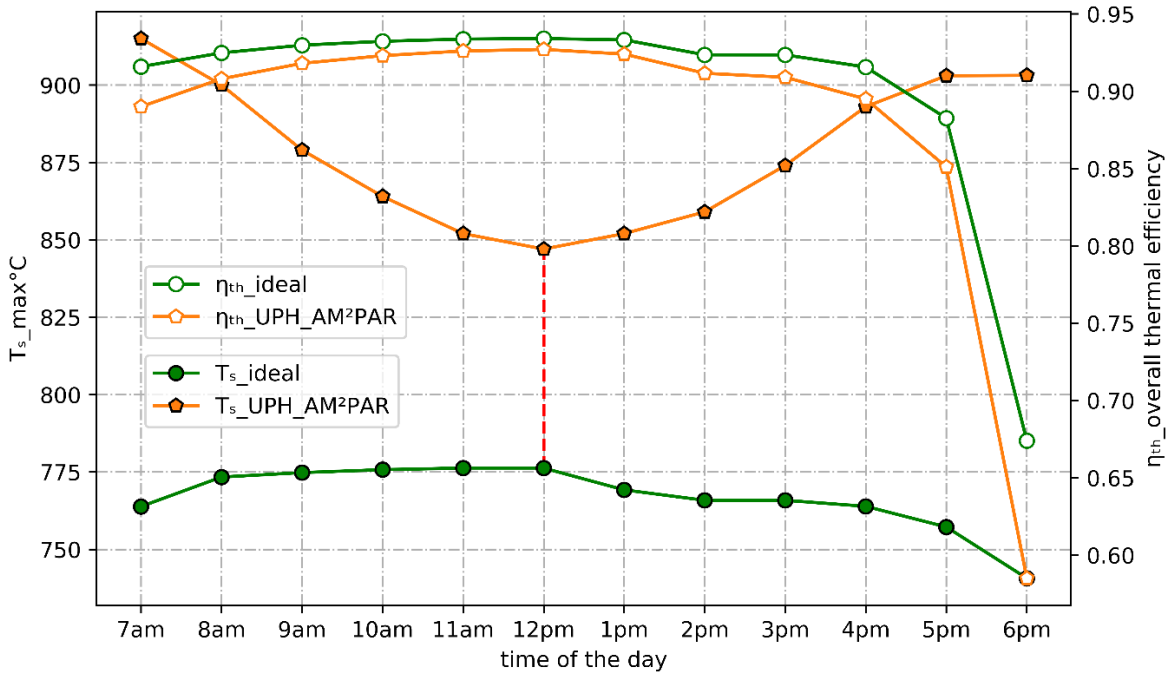

Figure 33: plot of the maximum surface temperature and thermal efficiency of the receiver in the ideal and real scenario (UPH_AM2PAR) as a function of hour of a typical day in July.

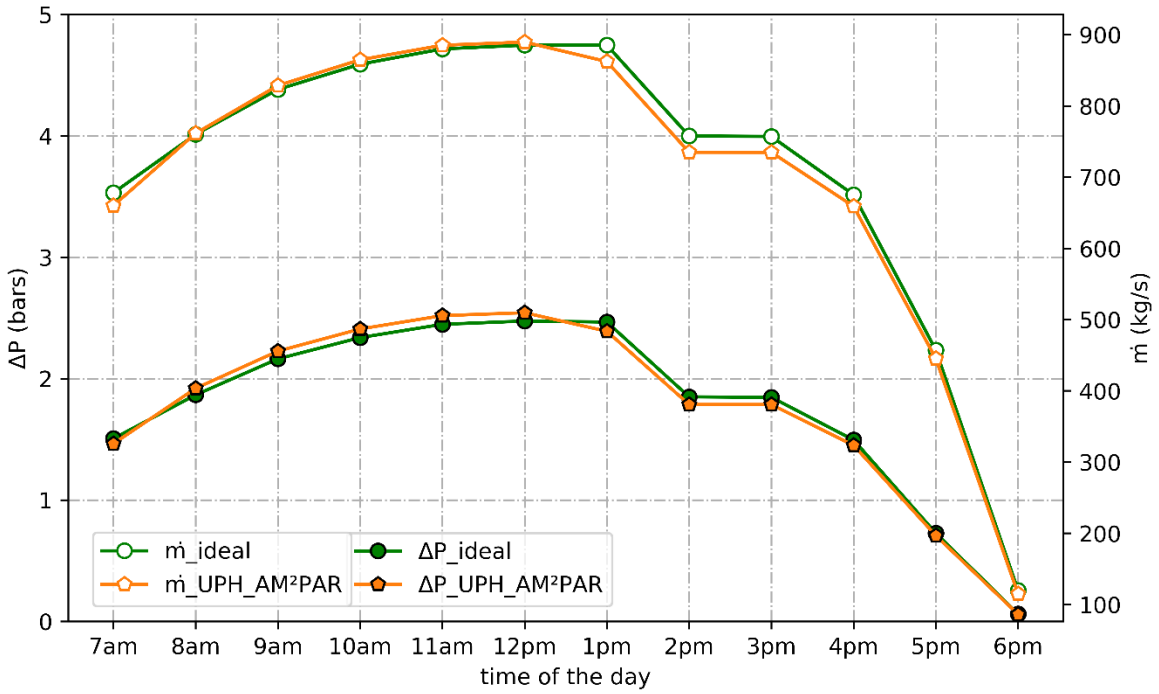

Figure 34: comparison of the pressure drop and the total mass flow rate in the ideal and the real case (UPH_AM²PAR) receiver

Design For Thermal Optimization of the Receiver: Novel Design Concepts

To mitigate the peak temperatures realized in the AM²PAR central receiver at all hours, active control and novel design concepts are required for the receiver architecture. Active control concepts include the use of valves to split the flow in different directions. In this section, a novel passive design concept that can aid in minimizing local high temperatures on the receiver surface is explored, namely, the Variable Pin Height (VPH) AM²PAR. This concept evolves from one of the advantages of Additive Manufacturing, in that the manufacturing method allows for flexibility in geometry. This flexibility is applied by varying the architecture of modules that are installed in the receiver.

The central drawback with a central receiver with uniform unit cell dimensions is that the flow rate through each unit cell is approximately uniform, to within 9 percent (Figure 30) for a fixed imposed pressure drop. This would mean that the exit temperature of fluid from a module in a low flux region would be far lower than the mean of 720°C, necessitating the exit temperature in higher flux regions to

be significantly in excess of this value for the average fluid temperature from the central receiver to be at 720^{o}C. This in turn, causes the maximum surface temperature in these modules to exceed the creep limit of the material. In the VPH-AM^{2}PAR concept, there is the same pin dimensions within a unit cell, and within a module; however, there is a variation in the height of the pins from one module to another. Specifically, pin heights in modules in low flux regions are reduced in order to decrease mass flow through these modules such that the exit temperature is closer to the central receiver average temperature, since all modules are connected in parallel. Consequently, the modules in the higher flux regions have a lower surface temperature. A drop in the mass flow for an imposed pressure drop in these smaller pin dimension sections would result in a decrease in total convective heat transfer to the fluid within the module; however, the corresponding reduction in the pin dimensions leads to a larger Nusselt number. These competing effects result in a relatively unchanged heat transfer coefficient. An iterative process is applied in the determination of the vertical variation of pin heights in the modules of the receiver. In Figure 35, the average circumferential flux of the receiver is plotted over the vertical span of the receiver. The iterative procedure involves mapping the flux distribution with a pin height distribution, with the goal of obtaining a narrower variation of fluid outlet temperature from all the modules; thus, the corresponding surface temperatures as well as outlet fluid temperatures will be increased in low flux areas where the peak surface temperatures are below the average and reduced in high flux areas where the peak surface and fluid outlet temperatures are above the average. Working akin to a heat spreader device, the variable height receiver reduces the maximum temperatures whilst at the same time raising the minimum temperatures of the surfaces. By referencing the solar noon (peak power) flux map, the process starts with reducing the pin heights in a horizontal array of modules where the flux average is below the mean and increasing the pin heights in areas where the flux average is far above the mean flux.

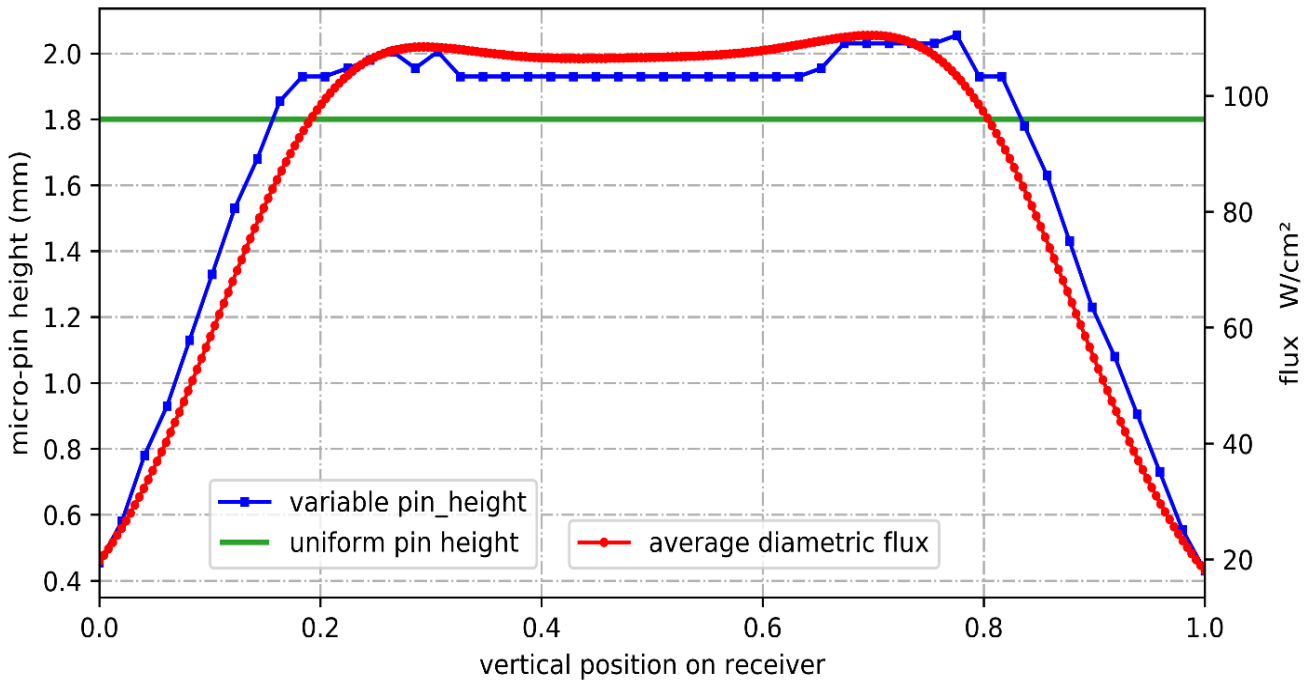

Figure 35: plot to show the pin height distribution over the different modules of the receiver as a function of their vertical position and flux in the receiver.

Thereafter, the simulation is run to obtain the outlet temperature distribution of the modules as well as the maximum surface temperature distribution from the modules. The pin heights are then modified (increased or decreased) based on the available margin for increasing or decreasing the pin height whilst maintaining the outlet module temperature below a near 720°C. The selective iteration of pin heights continues until the maximum temperatures of the modules cannot be further reduced to produce an averaged fluid outlet temperature of 720°C. The peak surface temperature for the solar noon simulation was 799.6^0C whilst maintaining an average receiver outlet temperature of 720°C.

Figure 36 shows the comparison of the maximum temperature in the receiver modules, and the thermal efficiencies on the variable height receiver. The heat map scales of Figure 36 are similar to that in Figure 29. By comparison, the heat map shows the apparent increase in uniformity of the maximum surface temperatures (2^{nd} column, Figure 36) realized in the receiver.

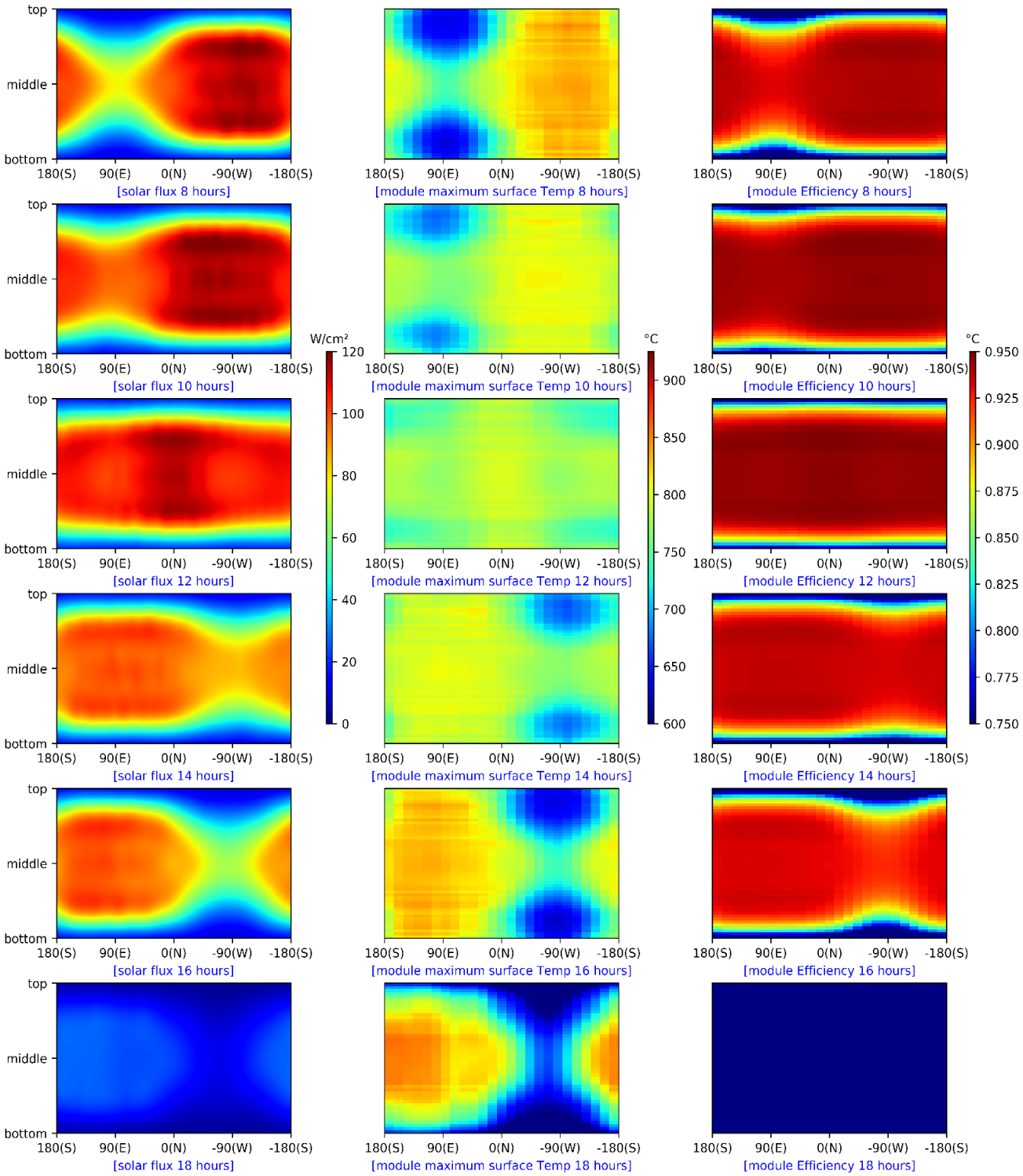

Figure 36: Maps of solar flux (left column) maximum module surface temperatures (middle) and module efficiency (right column) between 8 hours and 18hours on the VPH-AM²PAR between 8hrs and 18hhours.

The highest uniformity is seen at noon, which is a result of the optimized field design. Higher blue and red patches in Figure 36 represent an increase in non-uniformity of the maximum surface temperatures. Hence the farther away from noon time the condition is, the more non-uniform the heat flux, and thus also the temperature distribution. The consequence of increasing the surface temperature uniformity is realized in the fluid temperatures as well. As shown in Figure 37, for the maximum optima case of solar noon, the fluid temperature range to realize the target increase in temperature is narrower as a result. Noting that the solar flux also varies widely across the diameter of the receiver, the diametric variations in heat map are expected.

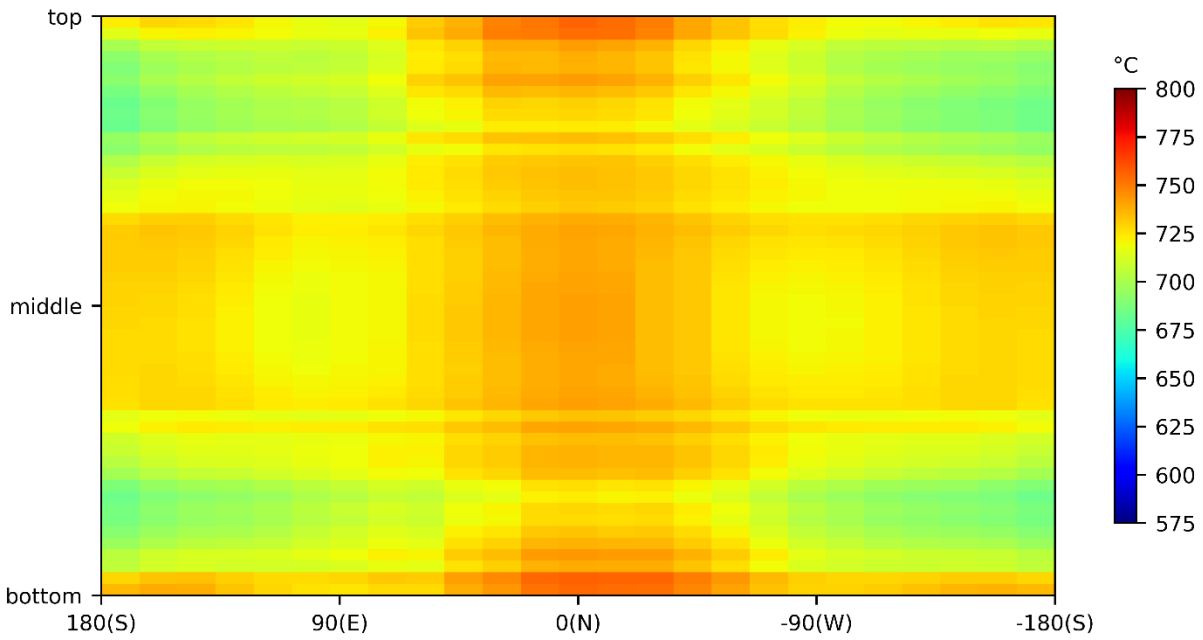

Figure 37: Map of fluid outlet temperatures from each of the 1250 modules simulated ranging from 575^{0}C to 800°C for solar noon for an average fluid outlet temperature of 720°C at noon time.

Figure 38 show the temperature distribution over the surface of the receiver. The surface temperature in the variable pin height receiver is quite like the distribution in the uniform pin height receiver because of the large temperature variations within a flow section: from inlet to outlet. Hence it cannot be emphatically said that the surface temperature uniformity is largely increased as a result of the variation of pin heights; the nature of the micro pin array receiver implies local variations in temperature will always exist.

Figure 38: Surface temperature distribution over the receiver at solar noon on a hot summer day for the variable pin receiver.

The peak temperatures however are minimized, and the fluid outlet temperatures from the modules have less variations with the VPH-AM^{2}PAR design, which has a significant impact on extending the life of the receiver with respect to creep. In Figure 39, the effect of the pin height variation on the mass flow distribution is seen to be significant, with a variation of about 500% throughout the receiver. The largest flow rate is realized in the hottest regions of the receiver near the center of the receiver. A side-by-side comparison of the maximum surface temperatures Figure 40 (a & b) and the receiver thermal efficiencies Figure 40 (c & d) is presented to visualize the differences between both receiver concepts. The variable pin height receiver is observed to lower the peak temperatures as compared to the uniform pin height receiver. In Figure 40 (c & d) a slight difference in thermal efficiency is observed at the extreme edges of the receiver.

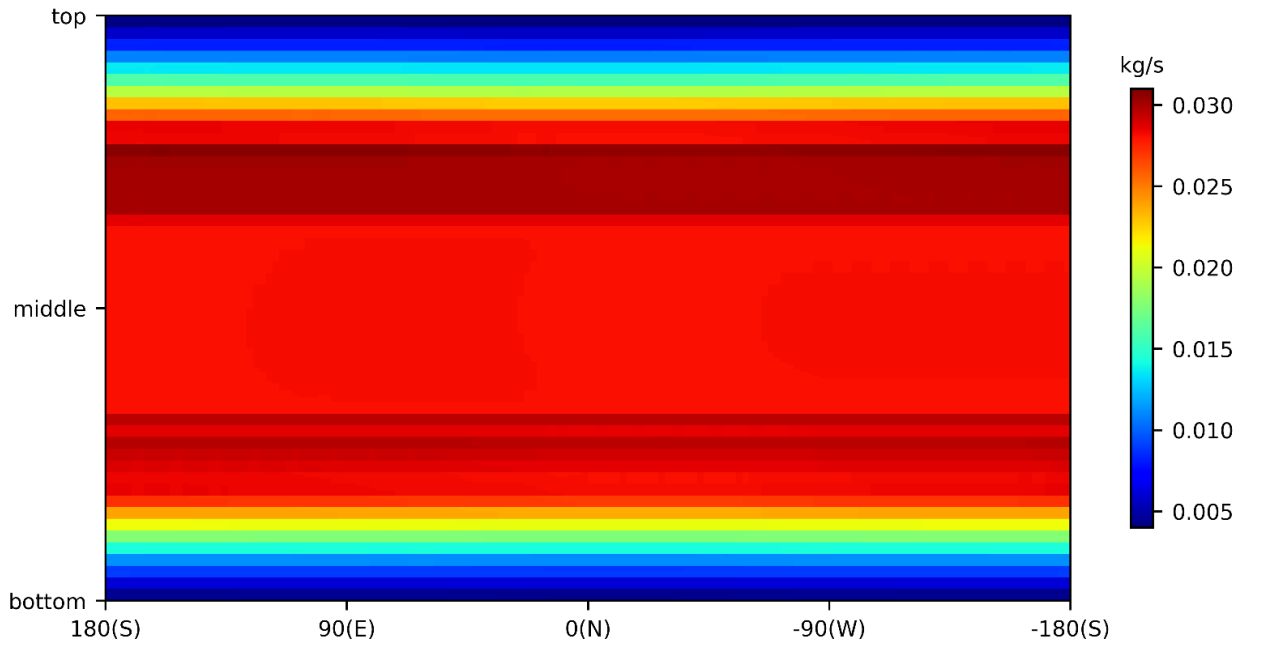

Figure 39: Mass flow distribution in each grid row of the variable height receiver at solar noon.

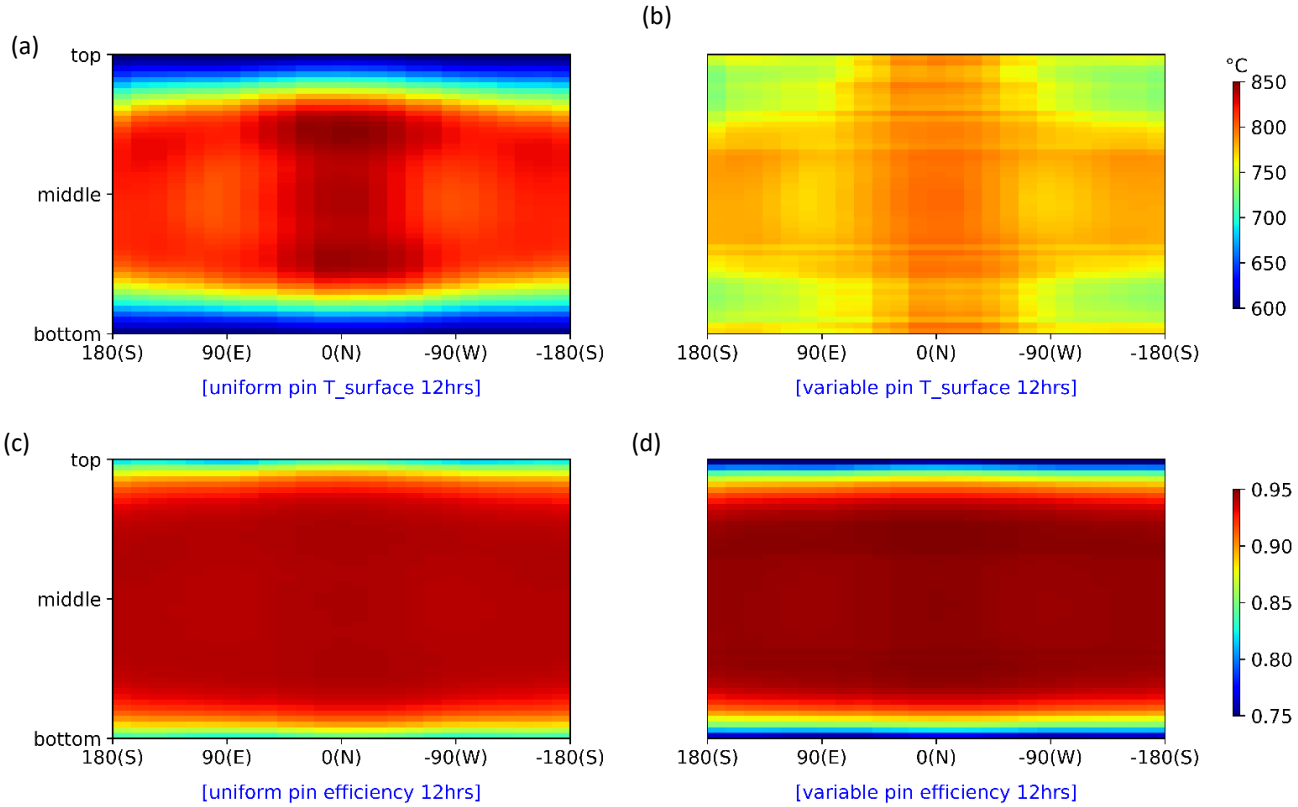

Figure 40: Side by side comparison of the VPH-AM^{2}PAR receiver and the UPH-AM^{2}PAR receiver at solar noon.

In the uniform pin height receiver, the surface temperatures are low at the edges for the given flow rate, as a result of the low heat fluxes. In the variable height receiver however, since the mass flow rate is lower in the low heat flux regions, the surface temperature is higher than in the uniform pin height design. There is thus the competing effect of an increased internal heat transfer coefficient, and a much higher radiation loss from the surface due to the higher temperatures. The center region of the variable pin receiver however has lower surface temperatures, and thus lower radiation losses. The resulting effect is a noticeable decrease in thermal efficiency of the VPH-AM^{2}PAR receiver at the edge modules; however, the magnitude is not known to affect the expected overall performance of a UPH-AM^{2}PAR receiver significantly, as seen in the overlapping curves of the thermal powers produced by the UPH-AM^{2}PAR and the VPH-AM^{2}PAR in Figure 41.

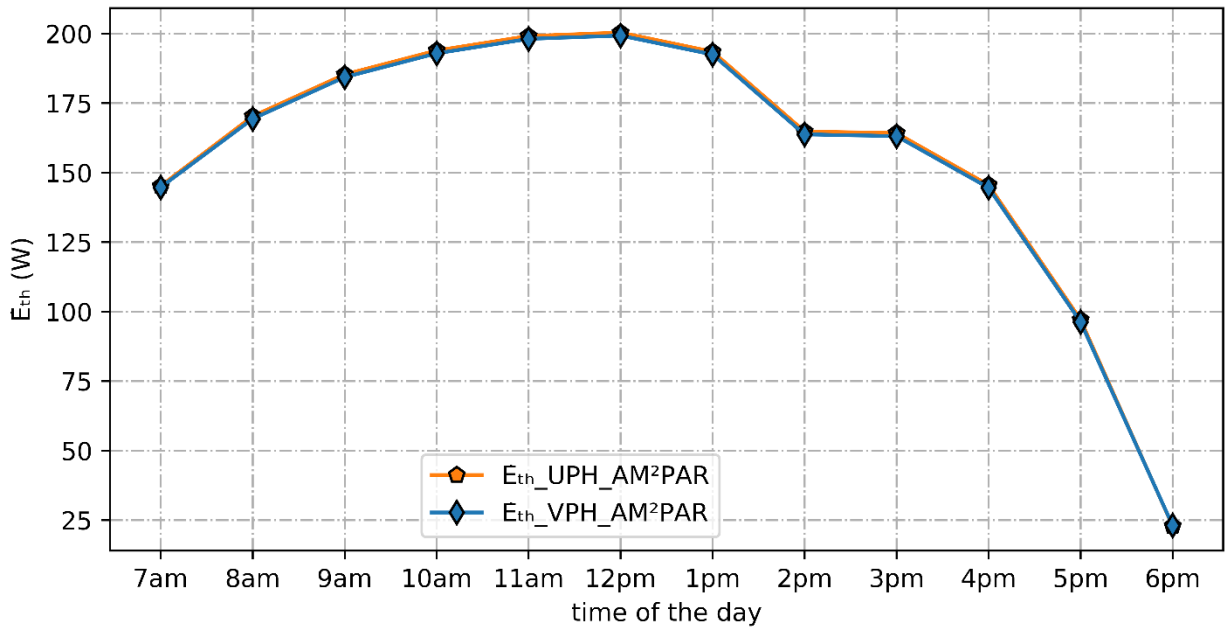

Figure 41: plot of the fluid thermal power of the VPH-AM2PAR vs UPH-AM2PAR given a fixed inlet fluid temperature of 550°C and a constrained outlet temperature of 720°C.

Variable Pin vs Uniform Pin vs Ideal Case Over a Summer Day

Comparisons have been made between the distribution of maximum surface temperatures and thermal efficiency of the UPH-AM^{2}PAR and VPH-AM^{2}PAR with variable spatial solar flux distribution. In this section, a comparison is made between the benchmark ideal case with uniform heat flux over the entire central receiver, the uniform pin height receiver, and the variable pin height receiver. In both cases, the inlet temperatures and the target fluid outlet temperatures have the same values at all simulated hours of the day: 550°C and 720°C respectively. Also, the average pin height in the VPH-AM^{2}PAR (1.654µm) will vary from the UPH-AM^{2}PAR (1.8µm), resulting in different pressure drops as well as pumping power requirements to meet the target fluid outlet temperatures. In Figure 42, the impact of the uniform height receiver on the peak surface temperature is seen. The variable pin heights as well as the heliostats in the solar field are optimized for solar noon, hence the reason why the maximum receiver surface temperature at the various times are the lowest at solar noon for the AM^{2}PAR receivers. The ideal case has a uniform flux distribution and will thus see its maximum surface temperatures at the solar noon because the maximum average heat flux occurs at that time. As seen in Figure 42, the difference between the ideal heat flux case and the UPH-AM^{2}PAR peak surface temperatures is minimum at solar noon: 75^{0}C.

However, with the VPH-AM^{2}PAR receiver, the difference at solar noon compared to the ideal heat flux case is 25^{0}C. The maximum surface temperature in the VPH-AM2PAR is 858^{o}C and occurs at 7 hours, whilst the maximum in the UPH-AM^{2}PAR is 915^{o}C (57^{0}C higher) . It is thus evident, from the presented results, that the VPH-AM^{2}PAR receiver considerably reduces the peak surface temperature of the receiver at all simulated hours. The thermal efficiencies of the variable height receiver are however lower by a few percentage points at all times of the day due to the higher surface temperatures at the edges of the receiver; this would result in a slightly reduced thermal power—but also relatively insignificant when compared to surface temperature impact—produced by the VPH-AM^{2}PAR compared to the UPH-AM^{2}PAR receiver.

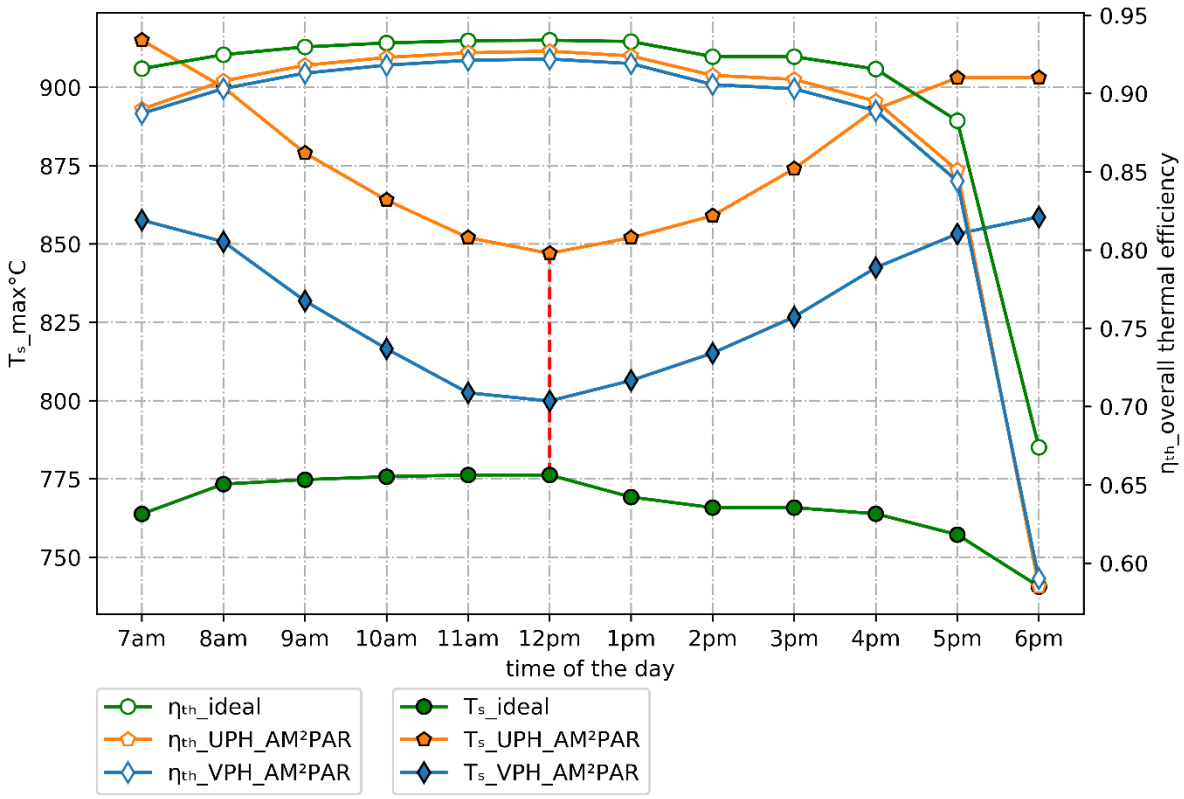

Figure 42: plots of the thermal efficiencies and the maximum surface temperatures of the different receiver concepts and the ideal case at different times of a hot summer day in Daggett-Barstow.

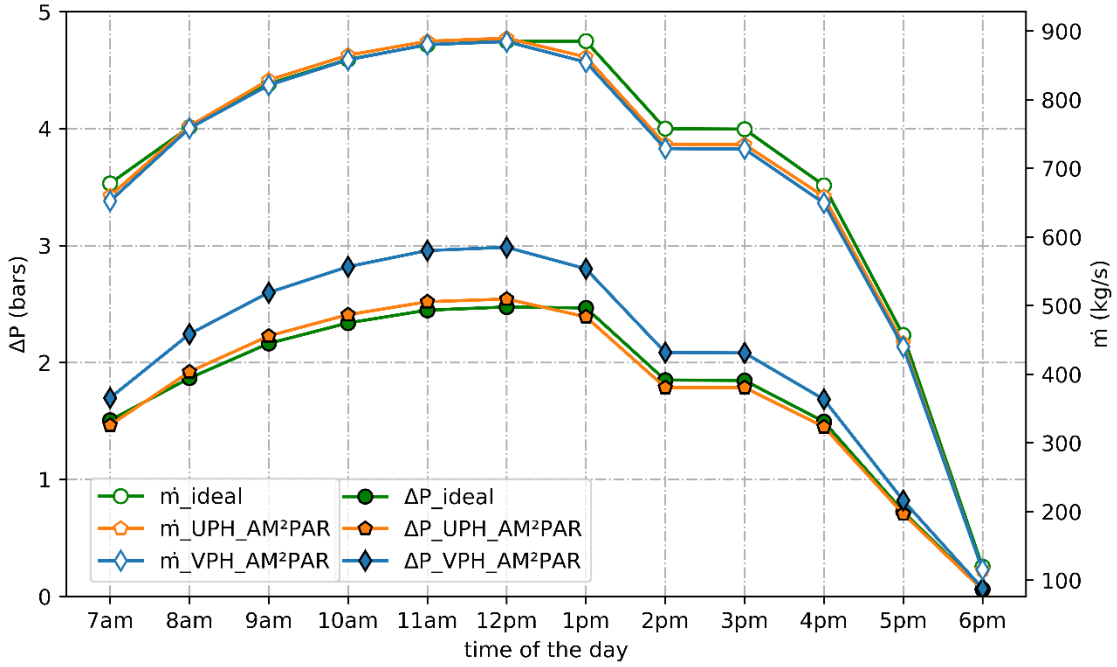

Figure 43: plot of the hydraulic parameters of the uniform height, variable height receiver and the ideal case for a target bulk outlet temperature of 720°C.

From Figure 43, the difference in pressure drop (parasitic pumping power) and mass flow rate required by the VPH-AM^{2}PAR and UPH-AM^{2}PAR is seen. For the same incident power at the given simulated hours, the VPH-AM^{2}PAR with its lower averaged pin height, compared to the UPH-AM^{2}PAR, tends to have a higher pressure drop than the latter for a similar mass flow rate into the receiver, with variations estimated to be a maximum of 20% at solar noon; hence, the VPH-AM^{2}PAR will see an average increase in parasitic pump power to supply fluid to the receiver of 17%.

To summarize the impact of the variable pin receiver on the peak surface temperatures, Figure 44 shows the histogram of the maximum surface temperatures realized in the uniform pin receiver and the variable pin height receiver. The red line in both plots is placed at a point T = 770°C to represent the creep limit of a certain design of Haynes 282 receiver. Firstly, the variable pin height receiver is shown to have more cluster of temperature bars around the red line, as compared to the uniform pin height receiver i.e. the uniform pin height has a wider range of temperatures when compared to the uniform pin height receiver at all times of the day. Secondly, the number of modules with maximum temperatures above 770°C are greater in the uniform pin height receiver than at the variable pin height receiver.

Significantly, peak temperatures are a challenge from an operational standpoint in the implementation of the micro-pin-array receiver. There are several methods of mitigating the impact of peak temperatures in design and operation of the receiver:

1. Modifying the geometry of the pin array within each module from inlet to exit to decrease the creep stress in the modules.
2. Reducing the operating fluid outlet temperature from the receiver at several times of the day to ensure that the maximum surface temperature is within the creep limits of the material.

The latter is discussed in the next section.

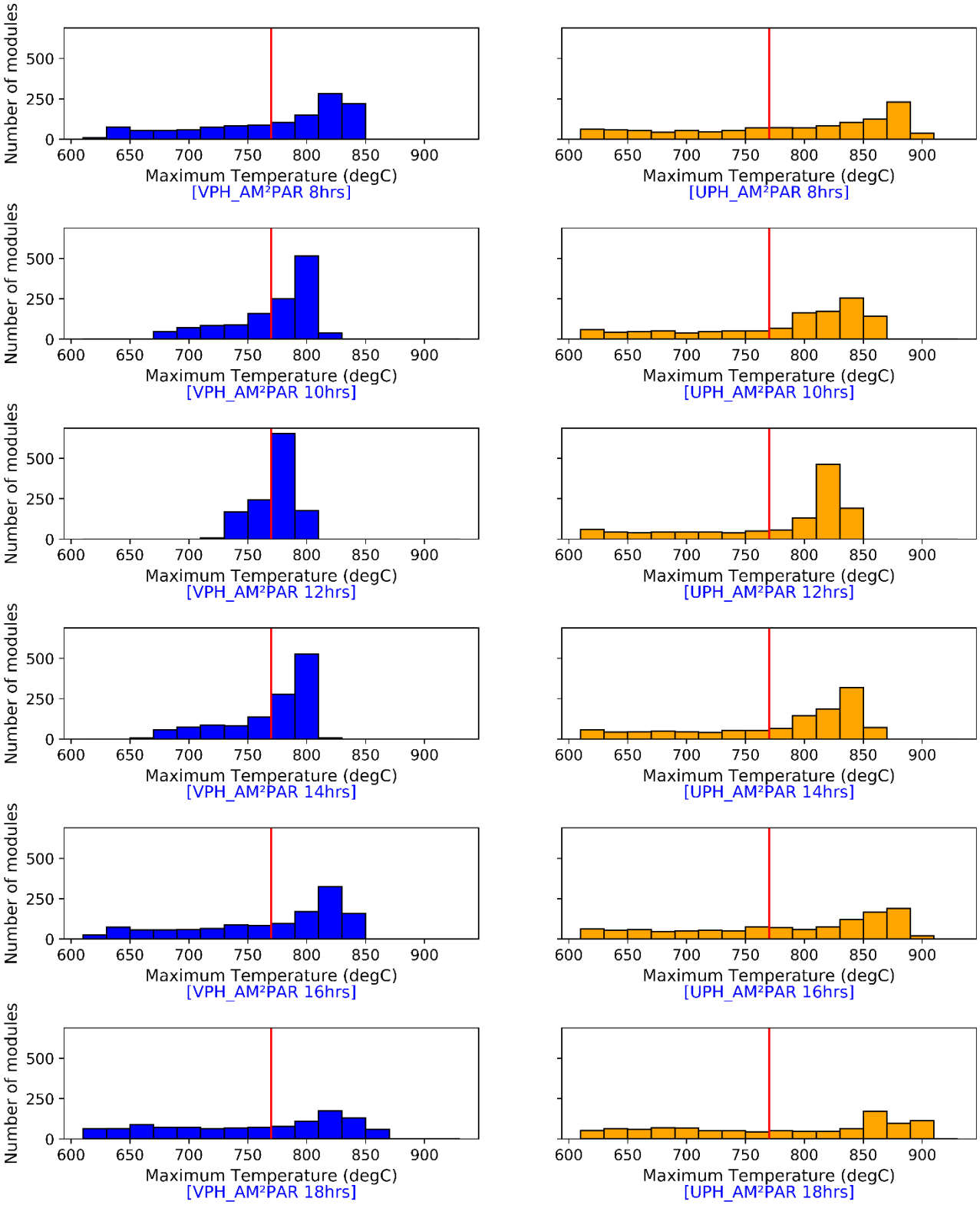

Figure 44: Distribution of module maximum temperatures of the UPH-AM^{2}PAR and the VPH-AM^{2}PAR receivers.

Operational Modification for Improved Creep Life

One of the ways of ensuring the creep life of the receiver meets the 30 year lifetime of the central receiver is by limiting the attainable exit fluid temperatures such that the maximum surface temperature does not exceed 770^{o}C for Haynes 282. Hence, simulations were performed to determine the exit fluid temperature from the receiver with a maximum surface temperature constraint of 770°C.

In Figure 45, the algorithmic sequence for obtaining the flow solution to ensure the maximum surface temperature of the receiver does not exceed the maximum value of 770°C is described. The sequence is similar to the sequence for solving to get a target fluid temperature (see Figure 28, Chapter 4), the exception being that the target fluid temperature solution seeks an average fluid temperature value whilst the target maximum surface temperature seeks a maximum value. The main constraint that governs the iterative procedure is the pressure drop in the unit cells. An increase in mass flow leads to an increase in pressure drop, and vice versa. The process of choosing the initial pressure drop condition in this algorithm is intuitive and manual: an initial guess pressure drop is chosen, and if the resulting maximum output surface temperature is higher than 770°C, the pressure drop guess is increased to a higher value and vice versa. After two simulations, the maximum surface temperatures and the corresponding pressure drops are linearly interpolated to get an estimated pressure drop that gives a 770°C maximum surface temperature. Such a step accelerates the convergence to a desired solution if the interpolation points are within a closer bound; since the relationship between maximum surface temperature and the pressure drop over a non-uniform flux receiver cannot be described as linear.

By increasing the mass flow rate to the receiver and thus causing a larger pressure drop, the fluid temperature and the corresponding surface temperature become lower. In Figure 46, the outlet fluid temperatures and the maximum surface temperatures are plotted for two conditions:

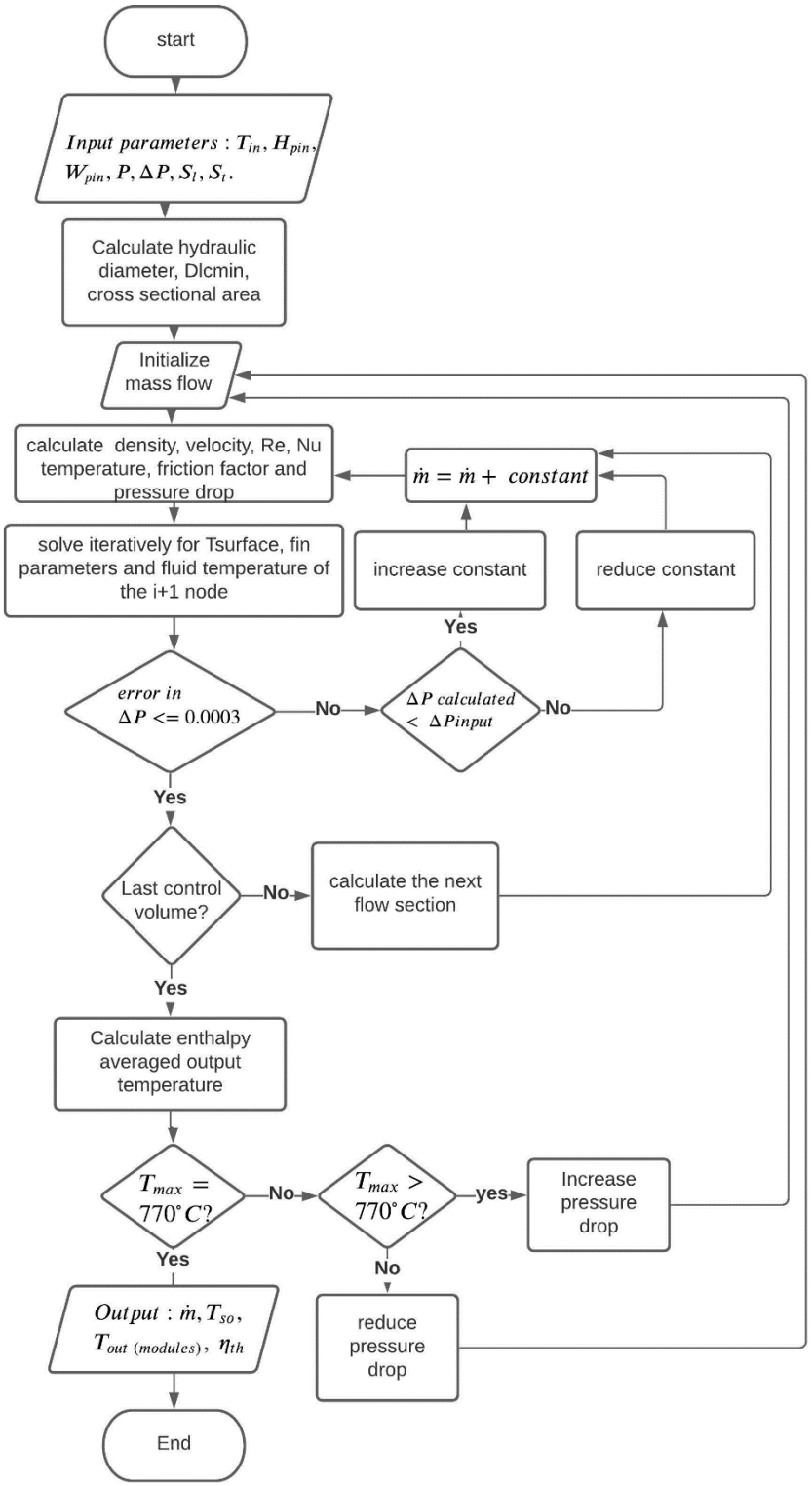

Figure 45: Flow chart showing the algorithmic sequence for obtaining the solution of a maximum receiver surface temperature less than 770°C.

a. Passive control of the receiver with variable pin height and fixed fluid outlet temperature (VPH-AM^{2}PAR-FT)

b. Passive control of the receiver with variable pin height and fixed maximum surface temperatures (VPH-AM^{2}PAR-ST).

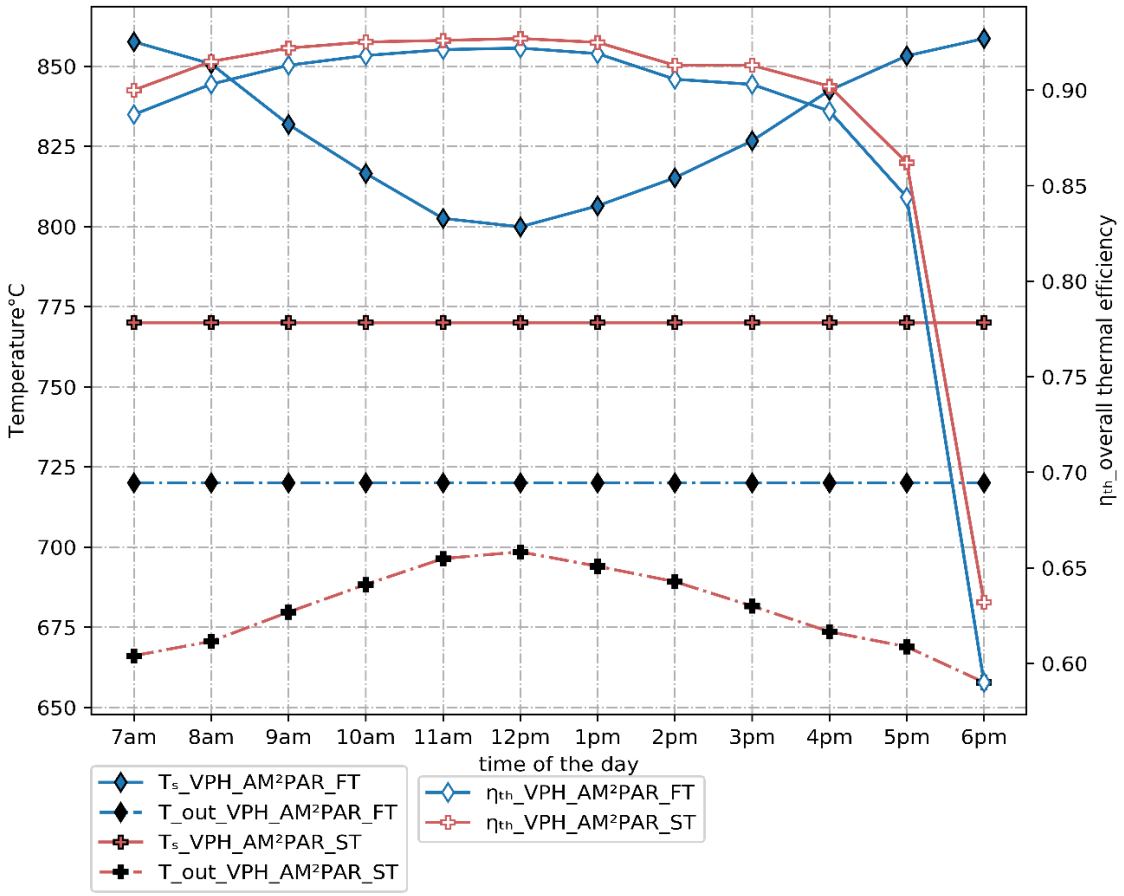

Figure 46: Thermal behavior of the variable pin height receiver comparing the fixed outlet fluid temperature condition and the fixed maximum surface temperature condition of 770°C.

It is important to note from Figure 46 that the overall efficiency of the receiver is higher at most times of the day when the maximum surface temperature constraint is imposed. The reason is due to a higher internal convective heat transfer coefficient to the fluid due to higher mass flow rate, and a corresponding lower surface temperature on the surface causing reduced external radiation and convection losses. However, between 10am and 2pm, the difference in efficiency between the two conditions is about 0.5%, numerically insignificant compared to the mitigating impact of surface temperature reduction. Another

important point from Figure 46 is the comparison of the fluid outlet temperatures between the fixed fluid temperature simulation and the fixed surface temperature simulation. From Figure 46, maximum surface temperatures as high as 857^0C are observed at 7hours and 17 hours, which is 87^0C above the benchmark. A significant result from the fixing of the surface temperature below 770°C is that the mean fluid temperature is in the worst case 62^0C below the target operating fluid temperature. Thus, accommodations can be made for power generation demands to utilize lower than targeted temperatures at certain times of the day, or under unprecedented weather conditions towards ensuring the maximum safety in the operation of the receiver. Hybrid systems using Auxiliary energy input to control the final fluid temperature are also an option.

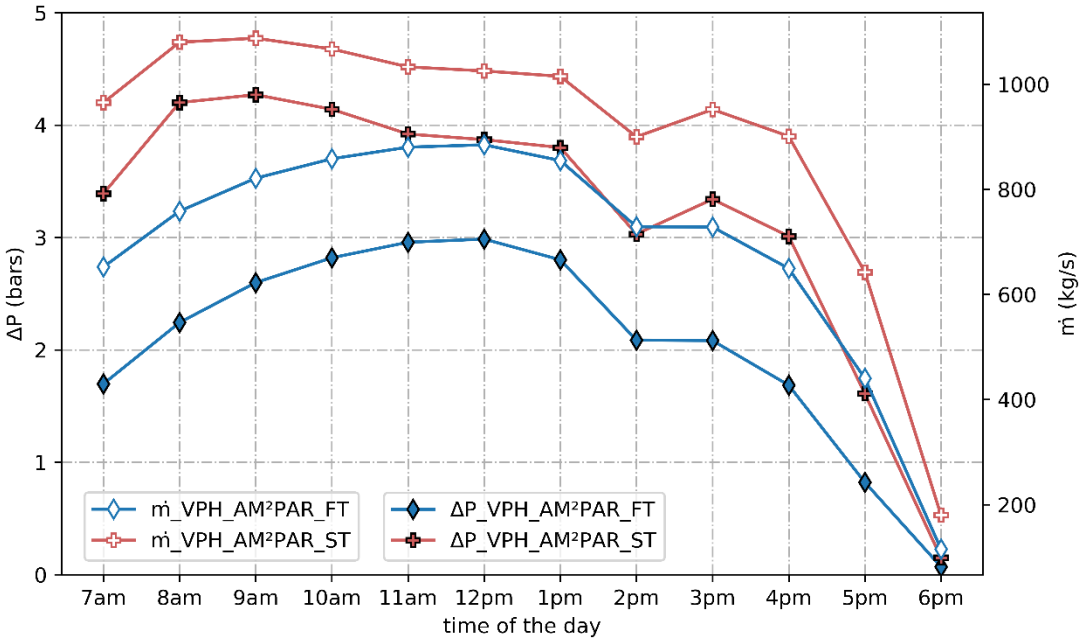

Figure 47: Comparison of the hydraulic parameters (mass flow and pressure drop) in the variable pin fixed fluid temperature (VPH-AM²PAR-FT) and variable pin fixed surface temperature (VPH-AM²PAR--ST) modes of receiver control.

The higher efficiency and lower temperatures in the surface temperature controlled mode of the receiver comes with its own penalty in pressure drop (Figure 47) which reflects in the parasitic pump power required for the operation of the plant. The mass flow and pressure drop behave as expected displaying

curve convergence closer to noon time for which the heliostat field is designed for optimal operation and similar convergence closer to 6pm when the incident heat flux has dropped by 85% from its peak value. Furthermore, the impact of the higher efficiency in the VPH-AM^{2}PAR-ST is further buttressed in Figure 48, where the plot of thermal power generated from the receiver is compared for the UPH-AM^{2}PAR, VPH-AM^{2}PAR-FT and VPH-AM^{2}PAR-ST. Noting the impact of reducing the surface temperatures in the VPH-AM^{2}PAR-ST also reduces the outlet fluid temperatures at all simulated hours (with a minimum of 658^{0}C at 6pm and a maximum of 699^{0}C at 12pm), the fluid thermal power at all simulated hours overlap very significantly. Hence the increased efficiency of the receiver does not translate to an increase in efficiency of the overall plant. The VPH-AM^{2}PAR receiver is capable of mitigating one of the major challenges of the non-uniformity in flux on the central receiver—peak fluxes.

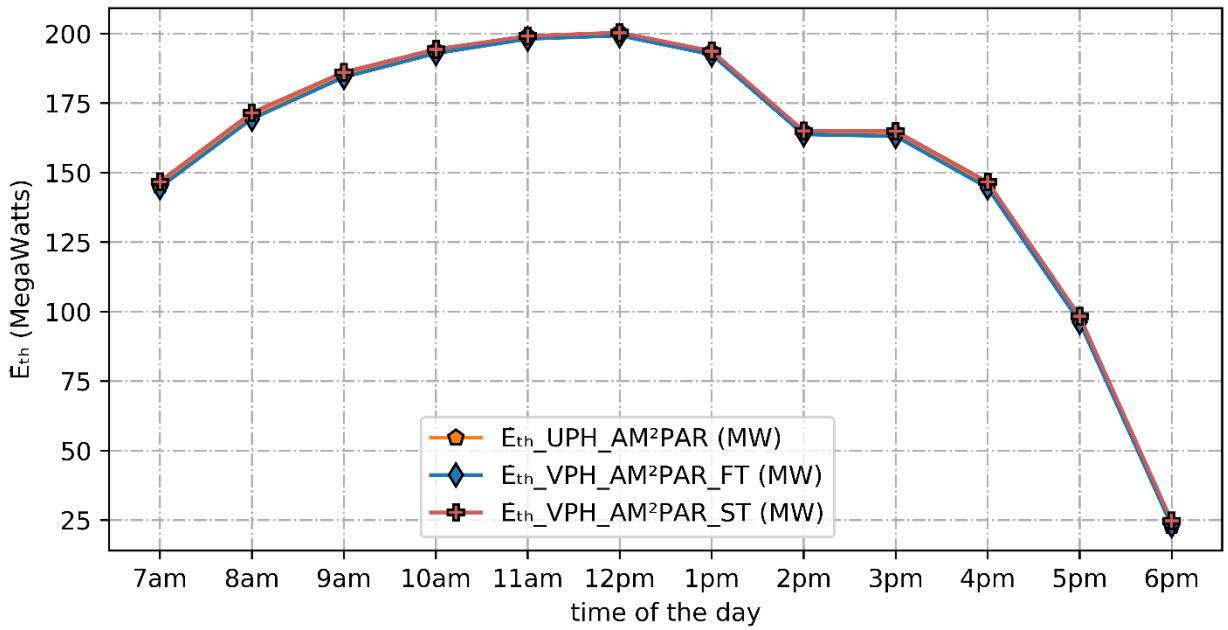

Figure 48: Fluid thermal power for the various concepts of the receiver. UPH-AM^{2}PAR and the VPH_AM^{2}PAR_FT have a constrained outlet fluid temperature of 720°C at all hours, whilst the VPH_AM^{2}PAR_ST has a constrained surface temperature of 770°C at all hours.

The comparison of the modular peak surface temperatures obtained in the VPH-AM^{2}PAR-FT (fluid temperature constrained) and VPH-AM^{2}PAR-ST (surface temperature constrained) receivers is presented in the histogram plotted in Figure 49. Each receiver concept consists of 1250 modules. The left column is made up of the fluid temperature constrained receiver, and the right column consists of the surface temperature constrained receiver. As seen in Figure 49, the histogram bars around the 770°C mark (which is the surface temperature limit for a 30 year creep lifetime of the receiver) have the tallest bins in the VP-AM^{2}PAR-ST receiver at all simulated hours but 6pm. Also, Figure 49 shows that the VP-AM^{2}PAR-ST receivers have more surface temperature uniformity as a result of the increased mass flow (and reduced maximum surface temperature) as seen by the more centralized clustering of the histograms at all simulated hours, compared to the VP-AM^{2}PAR-FT receiver.

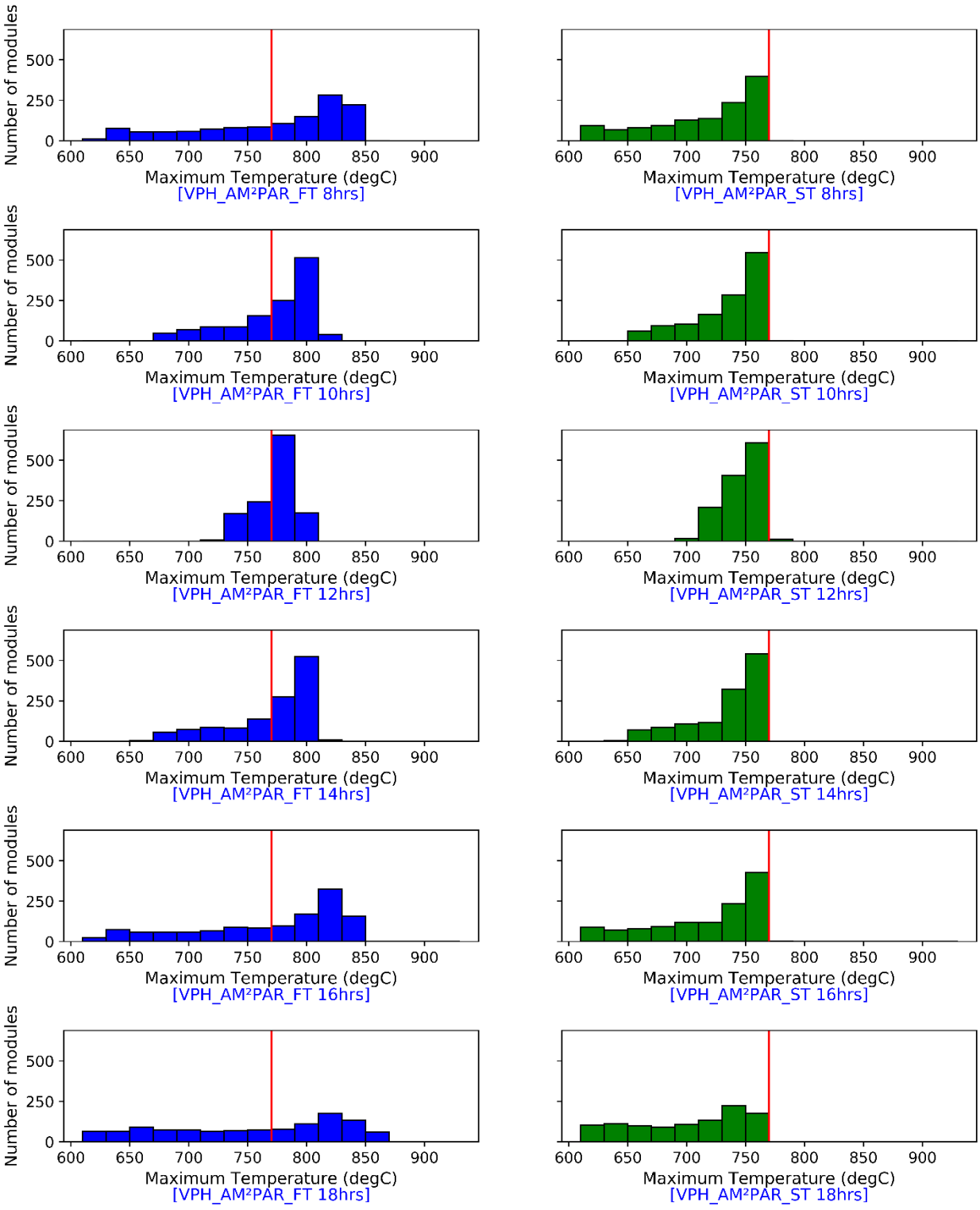

Figure 49: Distribution of the maximum surface temperatures in the VPH-AM²PAR-FT (Variable pin fixed outlet fluid temperature = 720°C) and the VPH-AM²PAR--ST (variable pin fixed maximum surface temperature of 770°C) modes of receiver operation.

CHAPTER 6
ANALYSIS MODEL FOR EXPERIMENTAL STUDY OF THE MICRO-PIN-ARRAY RECEIVER

Analysis Code for Flux Estimation in a Parabolic Dish

The μLPAR is in its early stages of development. Early on-sun characterization of a 8 cm x 8 cm μLPAR prototype have demonstrated the potential of the receiver to reach thermal efficiencies exceeding 90% [13], with sCO_2 as the working fluid albeit under low inlet fluid temperatures of 100-150^oC. The next stage in the scale-up is a 15 cm x 15 cm module with 6 pin arrays that are 2.5 cm each in length. The on-sun performance will in the future be demonstrated using a seven meter parabolic dish at the STEEL (Solar/Supercritical CO_2 Thermal and Energy Enhancement Laboratory) at University of California, Davis [13]. A significant thermal measurement challenge with the parabolic dish (Figure *50*), however is that the trackers on the foci that track the sun's movement occlude the possibility of getting direct solar irradiation distribution measurements from the receiver; such sensors are only likely to give a point or area averaged estimate of the incident solar irradiation on the receiver. An alternative method of assessing the receiver's performance in a parabolic dish plant is hence needed.

One method of assessing the receiver is by using the surface temperatures as a boundary condition, obtained through infrared cameras at periodic time intervals, and back-calculating the heat flux distribution on the receiver surface, and the internal heat transfer coefficient of the flow in the receiver. The numerical formulation of this analysis is less computationally intensive because of the known parameters: the flow rate of the fluid, the inlet temperature of the fluid, the fluid outlet temperatures from the receiver, and the surface temperature of the receiver. To tune the accuracy of the numerical solution, one of the known parameters, such as the outlet temperature can be kept as an unknown and the other parameters (such as the heat transfer coefficient) are simulated to verify the accuracy of the

numerical model. As thermal measurements are included in this analysis, the effect of the uncertainty of measurements in the results are imperative in interpreting the model solutions.

Figure 50*: Two-axis tracking 7-m parabolic solar dish at the STEEL lab (UC Davis) in operation during an on-sun experiment with a prototype 8 cm x 8 cm micro-pin-array receiver.*

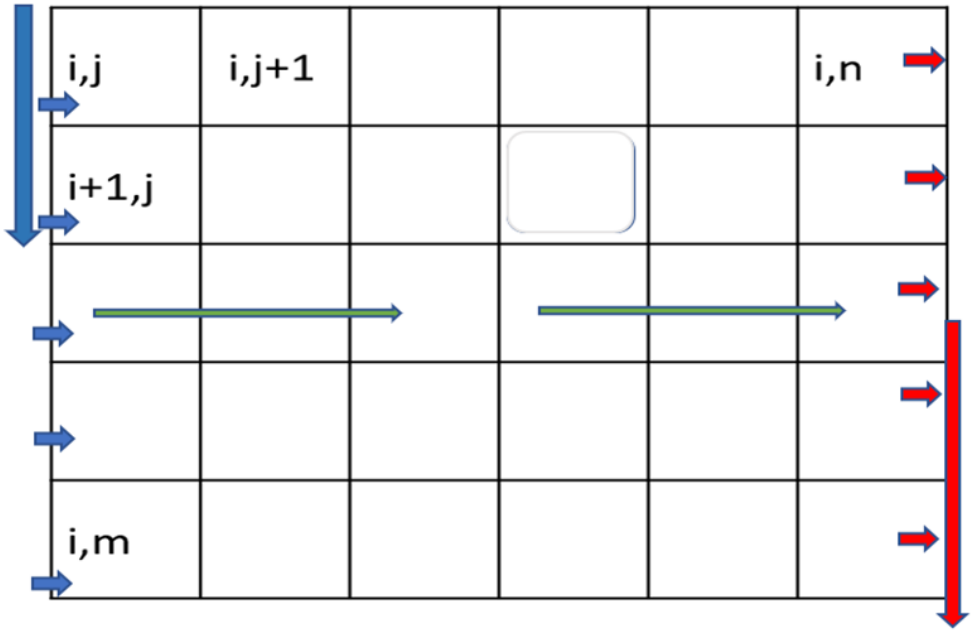

Figure 51: control volume discretization of the AM²PAR receiver in 2 dimensions.

In this method of evaluating the receiver performance, a surface temperature map is imposed in a numerical grid that represents the receiver geometry. The analysis code solves the energy balance equation by calculating for each control volume and estimating the fluid temperature rise based on the surface temperature. Parameters such as the internal heat transfer coefficients for micro-pin array receivers and the heat loss coefficients to the environment will be tuned until the fluid outlet temperature from the simulation matches the experimental results.

The analysis code propagates the fluid temperatures and the surface heat flux by balancing the resistance network and the heat transfer to the fluid:

$$dq_{i,j} = m_i \cdot (h_{i,j} - h_{i,j-1}) \quad = \frac{\left(T_{so_{i,j}} - 0.5(T_{f_{i,j}} + T_{f_{i,j-1}})\right)}{R_{i,j}} \tag{6.1}$$

And the fluid temperature of the next grid is gotten by re-arranging the equations:

$$T_{i,j} = \frac{2T_{so_{i,j}} - T_{i,j-1} \cdot \left(1 - 2R_{t_{i,j}} \dot{m}_i Cp_i\right)}{2 \cdot R_{t_{i,j}} \dot{m}_\iota \cdot C_{p_{i,j}} + 1} \tag{6.2}$$

Uncertainty Analysis

The absolute uncertainty of quantities measured and calculated to understand and validate the results from experiments on the micro-pin-array receiver. The important parameters to be determined from experiments include the fluid outlet temperature, the heat flux and the overall thermal efficiency of the receiver.

Uncertainty In The Nodal Temperature

The nodal temperature, for every node after the inlet is given by the equation 6.2. Its uncertainty is propagated until the last node of the control volume.

The temperature can be simplified further

$$T_{i,j} = \frac{T_{so_{i,j}}}{0.5 + R_{t_{i,j}} \cdot m_i \cdot C_{p_{i,j}}} - T_{i,j-1} \cdot \frac{0.5 - R_{t_{i,j}} \cdot \dot{m}_\iota \cdot C_{p_{i,j}}}{0.5 + R_{t_{i,j}} \cdot \dot{m}_\iota \cdot C_{p_{i,j}}} \tag{6.3}$$

There is no measurement of heat transfer coefficients involved, and because the heat transfer coefficient is a denominator in the thermal resistance term which would mean near zero sensitivity coefficients, relative negligible uncertainty is assumed in the thermal resistance of the unit cell receiver. The quantities with uncertainties therefore are T_s, $\dot{m}$, T_x. Sensitivity coefficients are obtained for each of the quantities using the Kline Mackintosh method.

Surface temperature sensitivity:

$$\frac{\delta T_{i,j}}{\delta T_{so\,i,j}} = \frac{1}{0.5 + R_{t_{i,j}} \cdot \dot{m}_\iota \cdot C_{p_{i,j}}} \tag{6.4}$$

For the sensitivity coefficient of the mass flow rate, the equation is divided into two:

$$\frac{\delta T_{i,j}}{\delta m_{1i}} = -T_{so_{i,j}} \times R_{t_{i,j}} \times C_{p_{i,j}} \times \left(\frac{1}{0.5 + R_{t_{i,j}} \cdot \dot{m}_i \cdot C_{p_{i,j}}}\right)^2 \quad (6.5)$$

$$\frac{\delta T_{i,j}}{\delta m_{2_i}} = \frac{-\left(0.5 + R_{t_{i,j}} \cdot \dot{m}_i \cdot C_{p_{i,j}}\right)\left(-R_{t_{i,j}} \cdot C_{p_{i,j}} \cdot T_{i_{i,j-1}}\right) - T_{i,j-1} \cdot \left(0.5 - R_{t_{i,j}} \cdot \dot{m}_i \cdot C_{p_{i,j}}\right)\left(R_{t_{i,j}} \cdot C_{p_{i,j}}\right)}{\left(0.5 + R_{t_{i,j}} \cdot \dot{m}_i \cdot C_{p_{i,j}}\right)^2} \quad (6.6)$$

Where m_1 is the first term in equation (6.3) and m_2 is the second term in the same equation.

$$\frac{\delta T_{i,j}}{\delta_{m_i}} = \frac{\delta T_{i,j}}{\delta_{m_{1_i}}} + \frac{\delta T_{i,j}}{\delta m_{2_i}} = \frac{0.5 - R_{t_{i,j}} \cdot \dot{m} \cdot C_{p_{i,j}}}{0.5 + R_{t_{i,j}} \cdot \dot{m} \cdot C_{p_{i,j}}} \quad (6.7)$$

$$\frac{\delta T_{i,j}}{\delta T_{i,j-1}} = \frac{0.5 - R_{t_{i,j}} \cdot \dot{m} \cdot C_{p_{i,j}}}{0.5 + R_{t_{i,j}} \cdot \dot{m} \cdot C_{p_{i,j}}} \quad (6.8)$$

Hence the overall uncertainty in the nodal Temperature is given by:

$$u(T_{i,j}) = \sqrt{\left(\frac{\delta T_{i,j}}{\delta m_i}\right)^2 \cdot b_{m_i}^2 + \left(\frac{\delta T_{i,j}}{\delta T_{i,j-1}}\right)^2 \cdot b_{T_{i,j-1}}^2 + \left(\frac{\delta T_{i,j}}{\delta T_{so_{i,j}}}\right)^2 \cdot b_{T_{so_{i,j}}}^2} \quad (6.9)$$

<u>Uncertainty In The Surface Heat Flux</u>

$$Q_{in_{i,j}} = Q_{fluid\ absorbed_{i,j}} + Q_{convection\ loss_{i,j}} + Q_{radiation\ loss_{i,j}} \quad (6.10)$$

$$uncertainty\ in\ Q_{in_{i,j}} = \sqrt{u_{f_{i,j}}^2 + u_{conv_{i,j}}^2 + u_{rad_{i,j}}^2} \quad (6.11)$$

The rms of the uncertainty in the fluid heat gain, and convection and radiation heat losses need to be obtained to get the uncertainty in the surface heat flux.

Uncertainty In Fluid Heat Absorbed

$$\delta Q_{fluid_{i,j}} = \dot{m}_i \cdot \left(h_{i,j} - h_{i,j-1}\right) \tag{6.12}$$

$$\frac{\delta Q_{fluid_{i,j}}}{\delta m_i} = \left(h_{i,j} - h_{i,j-1}\right) \tag{6.13}$$

$$\frac{\delta Q_{fluid_{i,j}}}{\delta h_{i,j}} = \dot{m}_i \tag{6.14}$$

$$\frac{\delta Q_{fluid}}{\delta h_{i,j-1}} = -\dot{m}_i \tag{6.15}$$

Hence the uncertainty in the fluid heat absorption is:

$$u_{f_{i,j}} = \sqrt{\left\{\left(\frac{\delta Q_{fluid_{i,j}}}{\delta \dot{m}_i}\right)^2 \cdot b_{\dot{m}_i}^2 + \left(\frac{\delta Q_{fluid_{i,j}}}{\delta h_{i,j}}\right)^2 \cdot u_{h_{i,j}}^2 + \left(\frac{\delta Q_{fluid}}{\delta h_{i,j-1}}\right)^2 \cdot u_{h_{i,j-1}}^2 + 2 \cdot \left(\frac{\delta Q_{fluid}}{\delta h_{i,j}}\right)\left(\frac{\delta Q_{fluid}}{\delta h_{i,j-1}}\right) \cdot u_{h_{i,j}} \cdot u_{h_{i,j-1}}\right\}} \tag{6.16}$$

Uncertainty In Convection

$$Q_{convection_{i,j}} = h \cdot dx \cdot dy \cdot \left(T_{so_{i,j}} - T_{ambient}\right) \tag{6.17}$$

$$\frac{\delta Q_{convection_{i,j}}}{\delta h} = dx \cdot dy \cdot \left(T_{so_{i,j}} - T_{ambient}\right) \tag{6.18}$$

$$\frac{\delta Q_{convection_{i,j}}}{\delta T_{so_{i,j}}} = h \cdot dx \cdot dy \tag{6.19}$$

$$\frac{\delta Q_{convection_{i,j}}}{\delta T_{ambient}} = -h \cdot dx \cdot dy \tag{6.20}$$

Where the area of the control surface is given as $A = dx * dy$ for a control volume, and dx and

$$\frac{\delta Q_{convection_{i,j}}}{\delta A} = h \cdot (dx + dy) \cdot (T_{so_{i,j}} - T_{ambient}) \tag{6.21}$$

Uncertainty in convection heat transfer is given by

$$u_{c_{i,j}} = \sqrt{\begin{aligned}\{&\left(\frac{\delta Q_{conv_{i,j}}}{dh}\right)^2 \cdot b_h^2 + \left(\frac{\delta Q_{conv_{i,j}}}{\delta T_{so_{i,j}}}\right)^2 \cdot b_{T_{so_{i,j}}}^2 + \left(\frac{\delta Q_{conv_{i,j}}}{\delta T_{amb}}\right)^2 \cdot b_{T_{amb}}^2 + \\ &\left(\frac{\delta Q_{conv_{i,j}}}{\delta A}\right)^2 \cdot b_A^2 + \\ &2 \cdot \left(\frac{\delta Q_{conv_{i,j}}}{\delta T_{so_{i,j}}}\right) \cdot \left(\frac{\delta Q_{conv_{i,j}}}{\delta T_{amb}}\right) \cdot b_{T_{amb}} \cdot b_{T_{so_{i,j}}}\}\end{aligned}} \tag{6.22}$$

Uncertainty In Radiation

$$Q_{radiation_{i,j}} = \varepsilon \cdot \sigma \cdot A_{surface} \cdot (T_{so_{i,j}}^4 - T_{dish}^4) \tag{6.23}$$

$$\frac{\delta Q_{rad_{i,j}}}{\delta \varepsilon} = \sigma \cdot A_{surf} \cdot (T_{so_{i,j}}^4 - T_{dish}^4) \tag{6.24}$$

$$\frac{\delta Q_{rad_{i,j}}}{\delta \sigma} = \varepsilon \cdot A_{surf} \cdot (T_{so_{i,j}}^4 - T_{dish}^4) \tag{6.25}$$

$$\frac{\delta Q_{rad_{i,j}}}{\delta Q_{A_{surf}}} = \varepsilon \cdot \sigma \cdot (dx + dy) \cdot (T_{so_{i,j}}^4 - T_{dish}^4) \tag{6.26}$$

$$\frac{\delta Q_{rad_{i,j}}}{\delta T_{so_{i,j}}} = 4 \cdot \varepsilon \cdot \sigma \cdot A_{surf} \cdot T_{so_{i,j}}^3 \tag{6.27}$$

$$\frac{\delta Q_{rad_{i,j}}}{\delta T_{dish}} = \varepsilon \cdot \sigma \cdot A_{surf} \cdot (-4 \cdot T_{dish}^3) \tag{6.28}$$

Uncertainty in radiation heat loss is obtained from the root mean squared average of the product of the sensitivity coefficients and the elemental uncertainty of each of the quantities.

$$u_{r_{i,j}} = \sqrt{\left\{\left(\frac{\delta Q_{rad_{i,j}}}{\delta \varepsilon}\right)^2 \cdot b_\varepsilon^2 + \left(\frac{\delta Q_{rad_{i,j}}}{\delta \sigma}\right)^2 \cdot b_\sigma^2 + \left(\frac{\delta Q_{rad_{i,j}}}{\delta A_{surf}}\right) \cdot b_x^2 + \left(\frac{\delta Q_{rad_{i,j}}}{\delta T_{so_{i,j}}}\right)^2 \cdot b_{T_{so_{i,j}}}^2 + \left(\frac{\delta Q_{rad_{i,j}}}{\delta T_{dish}}\right)^2 \cdot b_{T_{dish}}^2 + 2 \cdot \left(\frac{\delta Q_{rad}}{\delta T_{so_{i,j}}}\right)\left(\frac{\delta Q_{rad_{i,j}}}{\delta T_{dish}}\right) \cdot b_{T_{so_{i,j}}} \cdot b_{T_{dish}}\right\}} \tag{6.29}$$

Hence the uncertainty in the value calculated for the surface heat flux is:

$$u_{Q_{in_{i,j}}} = \sqrt{u_{f_{i,j}}^2 + u_{r_{i,j}}^2 + u_{c_{i,j}}^2} \tag{6.30}$$

<u>Uncertainty In Receiver And Thermal Efficiency</u>

Thermal efficiency values range from 0 to 1, and this quantity is numerically the smallest quantity being estimated in this section. The thermal efficiency uncertainty computation is obtained not for each control volume, but for the entire receiver surface because the results using the Kline-McClintock uncertainty calculation method will be unphysical because of the high sensitivity coefficients. Using computer programming indexing to represent the quantities in a two-dimensional array, in which

$$Q_{fluid\_total} = \sum Q_{fluid_{i,j}} \tag{6.31}$$

$$Q_{in\_total} = \sum Q_{in_{i,j}} \tag{6.32}$$

Since each of the control volumes has its uncertainty $u_f[i]$, the uncertainty in the sum of the fluid heat absorption ($Q_{f1} + Q_{f2+}\ Q_{f3} + \cdots Q_{fN}$) is given by:

$$ou.f = \sqrt{u_{f1}^2\ + u_{f2}^2\ + u_{f3}^2 + \cdots u_{fN}^2} = \sqrt{\sum {u_f}_{i,j}^2} \tag{6.33}$$

The uncertainty in the calculated heat input is also computed for each section, and is given as:

$$ou.q = \sqrt{(u_{q1}^2\ +\ \ u_{q2}^2 + u_{q3}^2\ + \cdots u_{qN}^2} = \sqrt{\sum u_{Q_{in_{i,j}}}^2} \tag{6.34}$$

Receiver efficiency uncertainty

$$\eta_{receiver} = \frac{Q_{fluid\_total}}{Q_{in\_total}} \tag{6.35}$$

$$\frac{\delta \eta_{receiver}}{\delta Q_{in\_total}} = -\frac{Q_{fluid\_total}}{Q_{in\_total}^2} \tag{6.36}$$

$$\frac{\delta \eta_{receiver}}{\delta Q_{fluid\_total}} = \frac{1}{Q_{in\_total}} \tag{6.37}$$

$$u_{\eta_{recevier}} = \sqrt{\left(\frac{\delta \eta_{receiver}}{\delta Q_{in\_total}}\right)^2 \cdot ou.q^2\ + \left(\frac{\delta \eta_{receiver}}{\delta Q_{fluid\_total}}\right)^2 \cdot ou.f^2} \tag{6.38}$$

Thermal efficiency uncertainty

$$\eta_{th} = \frac{Q_{fluid\_total}}{\alpha \cdot Q_{in\_total}} \qquad where\ \alpha = 1 - \rho_\lambda \tag{6.39}$$

$$\frac{\delta \eta_{th}}{\delta Q_{fluid\_total}} = \frac{1}{\alpha \cdot Q_{in\_total}} \tag{6.40}$$

$$\frac{\delta\eta_{th}}{\delta\alpha} = -\frac{Q_{fluid\_total}}{Q_{in\_total}} \times \frac{1}{\alpha^2} \tag{6.41}$$

$$\frac{\delta\eta_{th}}{\delta Q_{in}} = -\frac{Q_{fluid\_total}}{\alpha} \cdot \frac{1}{Q_{in\_total}^2} \tag{6.42}$$

$$u_{\eta_{th}} = \sqrt{\left(\frac{\delta\eta_{th}}{\delta Q_{fluid\_total}}\right)^2 \cdot ou.f^2 + \left(\frac{\delta\eta_{th}}{\delta Q_{in\_total}}\right)^2 \cdot ou.q^2 + \left(\frac{\delta\eta_{th}}{\delta\alpha}\right)^2 \cdot b_{alpha}^2} \tag{6.43}$$

In conclusion, the temperature map on the receiver can be used to make an estimate of the flux map distribution over the surface of the receiver. For a parabolic dish, a parabolic heat flux distribution is expected, and the result from computations can be plotted to verify that the simulations indeed give a good approximation of the heat flux distribution. A careful resolution of the uncertainty coefficients in the quantities leads reasonable and applicable results within a 95% confidence interval range..

Uncertainty Estimates for Representative Experimental Data

The uncertainty estimates were calculated by imposing a dummy surface temperature profile generated from simulations with an input from an assumed parabolic heat flux distribution on the receiver (as of the time of writing, actual experiments were yet to commence). The uncertainty of variables used in these calculations (Table 6) are taken from experimental data as reported in Rasouli et al. [13]. The propagation of the errors is done in a numerical code based on the equations above, and executed in python 3.8. The results of the error propagation are shown in Table 7.

Table 6: Representative measurement uncertainties used in error propagation.

Variables (*units*)	Uncertainty ($\pm$)
sCO_2 Inlet temperature, T_{in}, ($°C$)	± 1.1
Surface/ambient Temperature, T_{so} ($°C$)	± 0.5

CO_2 mass flow rate, $\dot{m}$ (g/s)	$\pm 0.1\%$ of reading
Surface reflectivity, ρ	$\pm 3\%$

In the uncertainty propagation, the internal convective heat transfer coefficient correlation is assumed to be accurate; the goal is to use experimental data in future work to assess and iterate upon the convective heat transfer coefficient based on the experimental results.

Table 7: Results of the error propagation with a dummy surface temperature map.

Variable	Propagated uncertainty
Absorbed heat by sCO_2 , Q_{fluid_total} , (W)	$\pm$ 0.103 (0.0003%)
Heat loss due to radiation, Q_{rad}, (W)	$\pm$ 64.7 (7.34%)
Heat loss due to convection, Q_{conv}, (W)	$\pm$ 0.024 (0.0193%)
Incident heat flux, Q_{in}, (W)	$\pm$64.70 (0.20%)
Receiver efficiency, η_{rec}	$\pm$ 0.00182 (0.19%)
Thermal efficiency, η_{th}	$\pm$ 0.0154 (1.59%)
Bulk fluid outlet Temperature, T_{out}, (W)	$\pm$ 30.35 (3.04%)

The analysis code is able to predict experimental parameters such as the bulk outlet fluid temperature from the receiver, the local solar flux distribution over the surface of the receiver, the thermal efficiency of the receiver. The analysis code can be further used with experimental data (measured inlet and outlet temperatures to calibrate the heat transfer coefficient model equation. Thus, the uncertainty analysis on the dummy data has shown the potential of the numerical code to estimate receiver performance parameters within a 95% confidence interval.

CHAPTER 7
CONCLUSIONS AND RECOMMENDATIONS

This work has investigated the application of AM micro-pin array receiver for concentrated solar power generation. Microlamination as a manufacturing method for pin array receivers, has faced setbacks in development due to failures in diffusion bonded and/or brazed joints [16]. In addition, chemical etching limits the design flexibility, requiring shallow pin heights to achieve the necessary pin spacing to maintain mechanical integrity as the channel height/width cannot be independently varied. A case for AM (in which channel height/width can be independently varied) as an alternate means of manufacturing the receiver and de-risking the challenges posed by microlaminated receivers has been presented in this study. It has been demonstrated that the additively manufactured receiver (AM^2PAR), which allows for flexibility in manipulating pin dimensions, and which allows larger aspect ratio pin arrays, can accommodate a unit cell length of about 16.6cm as compared to a microlaminated (µLPAR) receiver length of 3.3 cm—within the 2% of line pressure drop constraint as stipulated by the DOE SETO Receiver targets [9]. By simulating flow in the respective receiver designs for a constrained outlet temperature of 720°C and inlet of 550°C, (µLPAR and AM^2PAR) the µLPAR (3.3cm long pin array) has a thermal efficiency of 94.45% and a peak surface temperature of 777.01°C while the AM^2PAR (at 16.6cm pin array length), has a thermal efficiency of 94.06% and a maximum surface temperature of 777.17°C. Hence the additively manufactured receiver has comparable heat transfer performance with the microlaminated receiver, with the advantage of a reduced receiver header complexity.

This study has also demonstrated the application of the AM^2PAR receiver in an external receiver for power generation of 200 MW—by generating a conceptual CSP field in the Daggett-Barstow region from SolarPILOT, producing heat maps for a typical summer day in July, and implementing a 2-dimensional grid to study the local and global performance of the receiver over the course of the day. By additively

manufacturing the receivers for a 250m^2 receiver area, an external receiver can be built with 1250 modules encompassing 3 unit cells each (with pin array lengths of 16.6 cm, module length of 1 m, and module width of 0.2 m). Furthermore, the flux maps implemented in the numerical code have been used to study the impact of spatial and temporal non-uniformity in heat flux on the performance of the receiver. The results showed that the AM^{2}PAR receiver has the potential to absorb high heat flux as high as 95W/cm^2 with thermal efficiencies $\eta_{th} > 90\%$ at the design condition at noon and an average of 88.5% over the course of the summer day.

Non-uniformity of solar flux is a practical challenge, having a significant impact on surface temperature distribution of the receiver. Non-uniformity in heat flux gives rise to highly non-uniform temperatures within the receiver, and a target bulk outlet temperature of 720°C occurs with some parts of the receiver having fluid temperatures as high as 800°C and other parts with fluid temperatures as low as 575°C. The resulting impact of these uneven and high temperature distributions on the thermal stresses, thermal cycling in the receiver and the creep life of the receiver are not desirable. Active and passive control methods are suggested to mitigate the highly non-uniform temperatures that result on the receiver surface. A good candidate for passively mitigating the peak heat fluxes and surface temperatures is the VPH-AM^{2}PAR design, which creates lower pin heights in regions of low heat fluxes so as to decrease the mass flow through them and increase the fluid temperature from those sections. The simulation results demonstrate that the VPH-AM^{2}PAR receiver can lower the peak surface temperatures on the receiver by up to 50°C, however a maximum pressure drop penalty of 17% exists (which is significant in parasitic pump power supply) in utilizing variable height receiver. More so, by limiting the attainable exit fluid temperatures, and thus limiting the surface temperature of the receiver to a maximum of 770°C, the creep life of the receiver can be made to meet a 30 year lifetime. To this end, the outlet fluid temperature is decreased from 720°C to 658°C in the worst case (15.77W/cm^2 mean flux at 6pm), however the impact on the power generation is an insignificant reduction in power by 0.55% averaged over the day.

The feasibility of the AM^{2}PAR receiver concept is to be tested in the future with a prototype receiver module installed in a parabolic dish and surface temperature distribution on the receiver obtained from infra-red heat map images. When experiments are conducted, a local heat flux distribution on the receiver can be calculated with the code presented. In addition, results of the outlet temperature from the receiver and the surface temperature distribution from an on-sun experiment can be used to calibrate and validate the model for the internal heat transfer coefficient of the AM^{2}PAR receiver.

In the next steps of the AM^{2}PAR receiver development, experimental data on a prototype module of the receiver should be analyzed to validate the numerical code presented in this study. Also, experimental results of the mass flow distribution within the receiver will be vital toward understanding the behavior of flow within the receiver and the magnitude and impact of maldistribution on the receiver performance.

REFERENCES

[1] M. Mehos *et al.*, “Concentrating Solar Power Gen3 Demonstration Roadmap,” NREL/TP--5500-67464, 1338899, Jan. 2017. doi: 10.2172/1338899.

[2] V. Narayanan, B. M. Fronk, T. L’Estrange, and E. Rasouli, “Supercritical Carbon Dioxide Solar Thermal Power Generation—Overview of the Technology and Microchannel Receiver Development,” in *Advances in Solar Energy Research*, Singapore, 2019, pp. 333–355. doi: 10.1007/978-981-13-3302-6_11.

[3] T. L’Estrange *et al.*, “High Flux Microscale Solar Thermal Receiver for Supercritical Carbon Dioxide Cycles,” in *ASME 2015 13th International Conference on Nanochannels, Microchannels, and Minichannels*, San Francisco, California, USA, Jul. 2015, p. V001T03A009. doi: 10.1115/ICNMM2015-48233.

[4] K. R. Zada, M. B. Hyder, M. Kevin Drost, and B. M. Fronk, “Numbering-Up of Microscale Devices for Megawatt-Scale Supercritical Carbon Dioxide Concentrating Solar Power Receivers,” *J. Sol. Energy Eng.*, vol. 138, no. 6, p. 061007, Dec. 2016, doi: 10.1115/1.4034516.

[5] Y.-L. He, K. Wang, Y. Qiu, B.-C. Du, Q. Liang, and S. Du, “Review of the solar flux distribution in concentrated solar power: Non-uniform features, challenges, and solutions,” *Appl. Therm. Eng.*, vol. 149, pp. 448–474, Feb. 2019, doi: 10.1016/j.applthermaleng.2018.12.006.

[6] A. Boretti, S. Castelletto, and S. Al-Zubaidy, “Concentrating solar power tower technology: present status and outlook,” *Nonlinear Eng.*, vol. 8, no. 1, pp. 10–31, Jan. 2019, doi: 10.1515/nleng-2017-0171.

[7] M. J. Wagner, “Simulation and Predictive Performance Modeling of Utility-Scale Central Receiver System Power Plants,” 2008.

[8] M. R. Rodriguez-Sanchez, A. Sanchez-Gonzalez, C. Marugan-Cruz, and D. Santana, “Flow patterns of external solar receivers,” *Sol. Energy*, vol. 122, pp. 940–953, Dec. 2015, doi: 10.1016/j.solener.2015.10.025.

[9] Department of Energy (DOE), “Solar Energy Technologies Office Fiscal Year 2021 Funding Program: Photovoltaics and Concentrating Solar Power.,” USA, DE-FOA-0002378, Mar. 2021.

[10] D. Wait, “Development of 800°C Integrated Flow Channel Ceramic Receiver,” Solar Reserve LLC, USA, DE-EE0007113, 2018.

[11] C. K. Ho, “Advances in central receivers for concentrating solar applications,” *Sol. Energy*, vol. 152, pp. 38–56, Aug. 2017, doi: 10.1016/j.solener.2017.03.048.

[12] M. Wagner, “Direct s-CO2 Receiver Development,” National Renewables Energy Laboratory, USA, DE-EE00025832, Feb. 2017. doi: 10.2172/1505150.

[13] E. Rasouli, C. W. Mande, M. M. Stevens, and V. Narayanan, “On-Sun Characterization of Microchannel Supercritical Carbon Dioxide Solar Thermal Receivers: Preliminary Findings,” in *ASME 2019*

13th International Conference on Energy Sustainability, Bellevue, Washington, USA, Jul. 2019, p. V001T03A007. doi: 10.1115/ES2019-3898.

[14] M. B. Hyder and B. M. Fronk, "Simulation of thermal hydraulic performance of multiple parallel micropin arrays for concentrating solar thermal applications with supercritical carbon dioxide," *Sol. Energy*, vol. 164, pp. 327–338, Apr. 2018, doi: 10.1016/j.solener.2018.02.035.

[15] C. Naderi, E. Rasouli, V. Narayanan, and C. Horend, "DESIGN AND PERFORMANCE OF A MICROCHANNEL SUPERCRITICAL CARBON DIOXIDE RECUPERATOR WITH INTEGRATED HEADER ARCHITECTURE," *J. Enhanc. Heat Transf.*, vol. 26, no. 4, pp. 365–392, 2019, doi: 10.1615/JEnhHeatTransf.2019027787.

[16] P. McNeff *et al.*, "Practical Challenges and Failure Modes During Fabrication of Haynes 230 Micro-pin Solar Receivers for High Temperature Sueprcritical Carbon Dioxide Operation," in *Conference Proceedings of the European sCO2 Conference*, Oct. 2019, pp. 180–189. doi: 10.17185/DUEPUBLICO/48871.

[17] E. Rasouli, C. Naderi, and V. Narayanan, "Pitch and aspect ratio effects on single-phase heat transfer through microscale pin fin heat sinks," *Int. J. Heat Mass Transf.*, vol. 118, pp. 416–428, Mar. 2018, doi: 10.1016/j.ijheatmasstransfer.2017.10.105.

[18] I. H. Bell, J. Wronski, S. Quoilin, and V. Lemort, "Pure and Pseudo-pure Fluid Thermophysical Property Evaluation and the Open-Source Thermophysical Property Library CoolProp," *Ind. Eng. Chem. Res.*, vol. 53, no. 6, pp. 2498–2508, Feb. 2014, doi: 10.1021/ie4033999.

[19] "EOS M290 Additive Manufacturing Equipment Manual .pdf." [Online]. Available: https://www.eos.info/03_system-related-assets/system-related-contents/_pdf_system-data-sheets/eos_system_data_sheet_eos_m_290_en.pdf

[20] M. J. Wagner and T. Wendelin, "SolarPILOT: A power tower solar field layout and characterization tool," *Sol. Energy*, vol. 171, pp. 185–196, Sep. 2018, doi: 10.1016/j.solener.2018.06.063.

[21] J. G. Barberena, A. M. Larrayoz, M. Sánchez, and A. Bernardos, "State-of-the-art of Heliostat Field Layout Algorithms and their Comparison," *Energy Procedia*, vol. 93, pp. 31–38, Aug. 2016, doi: 10.1016/j.egypro.2016.07.146.

[22] M. R. Rodríguez-Sánchez, A. Sánchez-González, and D. Santana, "Feasibility study of a new concept of solar external receiver: Variable velocity receiver," *Appl. Therm. Eng.*, vol. 128, pp. 335–344, Jan. 2018, doi: 10.1016/j.applthermaleng.2017.08.173.

[23] A. Sánchez-González, M. R. Rodríguez-Sánchez, and D. Santana, "Aiming strategy model based on allowable flux densities for molten salt central receivers," *Sol. Energy*, vol. 157, pp. 1130–1144, Nov. 2017, doi: 10.1016/j.solener.2015.12.055.

[24] A. Zolan, W. Hamilton, M. Wagner, and K. Liaqat, "Solar Field Layout and Aimpoint Strategy Optimization," NREL/TP--5700-80596, 1813972, MainId:66327, Aug. 2021. doi: 10.2172/1813972.

[25] M. Mehos *et al.*, "Concentrating Solar Power Best Practices Study," NREL/TP-5500-75763, 1665767, MainId:7049, Jun. 2020. doi: 10.2172/1665767.

[26] A. Sánchez-González and D. Santana, “Solar flux distribution on central receivers: A projection method from analytic function,” *Renew. Energy*, vol. 74, pp. 576–587, Feb. 2015, doi: 10.1016/j.renene.2014.08.016.

[27] C. He, H. Zhao, Q. He, Y. Zhao, and J. Feng, “Analytical radiative flux model via convolution integral and image plane mapping,” *Energy*, vol. 222, p. 119937, May 2021, doi: 10.1016/j.energy.2021.119937.

[28] F. J. Collado and J. Guallar, “Fast and reliable flux map on cylindrical receivers,” *Sol. Energy*, vol. 169, pp. 556–564, Jul. 2018, doi: 10.1016/j.solener.2018.05.037.

[29] P. Garcia, A. Ferriere, and J.-J. Bezian, “Codes for solar flux calculation dedicated to central receiver system applications: A comparative review,” *Sol. Energy*, vol. 82, no. 3, pp. 189–197, Mar. 2008, doi: 10.1016/j.solener.2007.08.004.

[30] G. Kolb, “An evaluation of possible next-generation high temperature molten-salt power towers.,” SAND2011-9320, 1035342, Dec. 2011. doi: 10.2172/1035342.

APPENDIX

NUMERICAL PROGRAM FOR COMPUTING THE MPAR RECEIVER THERMAL AND HYDRAULIC PARAMETERS FOR A CONSTRAINED INLET AND OUTLET TEMPERATURE

```
import numpy as np
from CoolProp.CoolProp import PropsSI
import matplotlib.pyplot as plt

IC = np.array([15,20,30,40,50,60,70,80,90,100,110,120])
#IC = np.array([65.5,75.3,81.07,84.37,86.36,86.8,84.1,72.6,72.54,65.30,45.82,15.73])

e = 0.95            # emissivity constant
pl = 0.05           # reflectivity constant

Bo = 5.67e-8        #Boltzmann constant
Td = 39 +273.15     #dish temperature
Ta = 39 + 273.15    #ambient temperature
ha  = 8.8           #convective heat loss coefficient of the air
Tin = 550 + 273     #inlet temperature of CO2 supercritical
Tout = 720 + 273
P = 1.92e7          #fixed pressure through the pin-array

d = 4e-4            #the thickness of the film before heat transfer

Hpin = 1.8e-3       #height of the pin
Wpin = 1.2e-3       #width of the pin
```

```
Sl = 2.13e-3         #longitudinal pitch
St = 2.46e-3        #transverse pitch


Min_l = 26e-3  #minimum length of flow path
yy = Min_l/Sl  # whole number that gives length closest to 15cm
yy = int(yy)
yy
zz = len(IC)

#l = Min_l * 6  # length of the receiver dervied by aiming for 15.6cm
l = 0.166
w = 0.20            # width of the receiver


Npin_t = w/ St       #Number of pins transverse
Npin_l = l/ Sl #no of pins in a length of each section (array) --index index zz

dx = l/yy   #dx = one pin

A = dx*w          #area of a dx section  --index zz

Dlcmin =  4*(Hpin*w - Npin_t*(Wpin*Hpin) ) /  ( 2*( (w - Npin_t*Wpin) + Hpin*Npin_t ) ) #hydraulic
diameter = 4*Area/P
Dh = Wpin
Across = Hpin*w
Across_2 = Hpin*w - Npin_t*Wpin*Hpin #flow crosssectional area

#1.calculate the maximum velocity through flow
Sd1 = np.sqrt(Sl**2 + (St**2/2)**2)
```

```
Sd1
pass1 = (St + Wpin)/2
#Sd1 > (St + D)/2 hence we have a transverse plane



#2. Arrays for model
Tr2 = np.zeros([zz,yy])
T2  = np.zeros([zz,yy]) #T(x+dx)
T1  = np.zeros([zz,yy]) #Tx = fluid inlet temperature at every section
ku  = np.zeros([zz,yy])  #conductivity of Haynes
Qf  = np.zeros([zz,yy])   #fluid temperature

h1  = np.zeros([zz,yy])  #enthalpy at inlet
h2  = np.zeros([zz,yy])  #enthalpy at outlet

Qin = np.zeros([zz])

m   = np.zeros([zz])           #mass flow rate of CO2
m_1 = np.zeros([zz])

T_diff    = np.ones([zz])
DP_sum = np.zeros([zz])
DP_sum_2 = np.zeros([zz])

Re = np.zeros([zz,yy])
Rt = np.zeros([zz,yy])

fD = np.zeros([zz,yy])
DP = np.zeros([zz,yy])
```

```
fD_2 = np.zeros([zz,yy])  #based on erfan correlation
DP_2 = np.zeros([zz,yy])  #based on erfan correlation

hi = np.zeros([zz,yy])
n_fi = np.zeros([zz,yy])
no_fi = np.zeros([zz,yy])

q_conv = np.zeros([zz,yy])
q_rad = np.zeros([zz,yy])
m_rad = np.zeros([zz])
m_conv = np.zeros([zz])

n_th = np.zeros([zz,yy])

a_Qf = np.zeros([zz])
a_Qin = np.zeros([zz])
n_th_1 = np.zeros([zz])
Trmax = np.zeros([zz])
hi_mean = np.zeros([zz])
m_Re = np.zeros([zz])
m_Rt = np.zeros([zz])
m_no_fi = np.zeros([zz])

#solving for the parameter distribution in the receiver

for k in range(zz):        #zz

   m[k] = (IC[k] * l * w *1e4) /(1000*(Tout-Tin)*1.58)
   q = 0
   while (T_diff[k] > 0.003):
```

```
if (k==0):
  m_1[k] =  m[k]*(1 +(0.001*q))
else:
   m_1[k] = m_1[k-1]*(1 +(0.001)*q)
if(T2[k,yy-1] > Tout):
   q+=1
else:
   q-=1
for i in range(yy): #xx   by moving from j to j because thats the flow pattern

  if(i==0):
    T1[k,i] = Tin
  else:
     T1[k,i] = T2[k,(i-1)]

  Qin[k] = IC[k]*(A*1e4)
  rho = PropsSI('D','P',P,'T',T1[k,i],'CO2') #density of supercritical CO2

  V = m_1[k] / (rho * Across)                    #I am not sure about the area
  Vmax = V * (St / (St - Wpin))                #maximum velocity in flow direction

  Cp = PropsSI('C','P',P,'T',T1[k,i],'CO2')     #Cp of CO2
  kf = PropsSI('L','P',P,'T',T1[k,i],'CO2')     #conductivity of fluid beetween 500 and 600
  uu = PropsSI('V','P',P,'T',T1[k,i],'CO2')     #dynamic viscosity between 500 and 60°C (engineering
toolbox)
  Pr = (uu/rho) / ( kf/(rho * Cp) )

  Re_2 = rho * Vmax * Dh / uu

  #1 using Erfan correlation
```

```
Re[k,i] = rho * Vmax * Dlcmin / uu                #Reynold's number

Nu = 0.039*( (Sl - Dlcmin)/Dlcmin )**(-0.19) * Re[k,i]**0.837 * Pr**0.557 #Nusslet number

hi[k,i]  = Nu * kf/Dlcmin  #convective heat transfer coefficient of the pin based on Dh = Dlcmin for square form


fD[k,i] = 4*0.221*(Sl/Dh)**(-1.4)*(St/Dh)**(-0.54)*(Hpin/Dh)**(0.056)*Re_2**(-0.08)*((l/yy)/(Dh*(Npin_l/yy)) )


DP[k,i] = ( fD[k,i] * 0.5 * rho * Vmax**2 * (Npin_l/yy) )


fD_2[k,i] = 9.2 * (Hpin/Dh) **(-0.43) * ((St - Dh)/Dh)**0.07 *((Sl - Dh)/Dh)**0.07*Re[k,i]**(-0.15)

DP_2[k,i] = ( fD_2[k,i] * 0.5 * rho * Vmax**2 * (Npin_l/yy) )


#iteration to solve for the surface temperature



if(i==0):
  Tr = 1000
else:
   Tr = Tr2[k,i-1]
error = 1
cc1 = 0
cc2 = 0
while (error > 0.0005):
   ku[k,i] = 0.0191*Tr + 10.627    #conductivity of the haynes230 #move into the loop
   m_fi = np.sqrt( ( hi[k,i] * np.pi*Wpin )/ (ku[k,i] * 0.25*np.pi*Wpin**2)) #m parameter
   n_fi[k,i] = np.tanh(m_fi*Hpin)/ (m_fi*Hpin)    #fin efficiency


   Af_fi = np.pi*Wpin*Hpin  #fin exposed area, for one fin Af = P x L
   At_fi = (Npin_l/yy * Npin_t)*Af_fi + (A - (Npin_l/yy *Npin_t)*(0.25*np.pi*Wpin**2)  )
```

```
    no_fi[k,i] = 1 - Af_fi/At_fi * (Npin_l/yy) * Npin_t * (1 - n_fi[k,i])  #overall fin array efficiency
    Rt[k,i]      =  (1 / At_fi) * (1/(hi[k,i]*no_fi[k,i]) )   #overall resistance
    cc1 = 1 / (0.5 + Rt[k,i] * (m_1[k]) * Cp)
    cc2 = (T1[k,i] * (0.5 - Rt[k,i]*(m_1[k])*Cp) )/ (0.5+Rt[k,i]*(m_1[k])*Cp)
    Tr2[k,i] = (  Qin[k]*(1-pl) + (m_1[k])*Cp*(cc2 + T1[k,i]) + ha*(A)*Ta -
          e*Bo*(A)*(Tr**4 - Td**4)  ) /  (m_1[k]* Cp* cc1 + ha*A )
    error = abs ( (Tr2[k,i] - Tr)/Tr )
    Tr = abs(0.5*(Tr2[k,i] + Tr))

  T2[k,i] = cc1*Tr2[k,i] - cc2
  #h1[k,i] = PropsSI('H','P',P,'T',T1[k,i],'CO2')  #enthalpy at CV inlet section
  #h2[k,i] = PropsSI('H','P',P,'T',T2[k,i],'CO2')  #enthalpy at  CV outlet section
  Qf[k,i] = (m_1[k])*Cp*(T2[k,i] - T1[k,i])         #CV fluid heat transfer
  n_th[k,i] = Qf[k,i] / (( 1-pl)*Qin[k])
  q_rad[k,i] = e*Bo*(A)*(Tr2[k,i]**4 - Td**4)
  q_conv[k,i] = ha * A * (Tr2[k,i] - T2[k,i])

a_Qf[k] = np.sum(Qf[k,::])
a_Qin[k] = Qin[k]*yy
n_th_1[k] =  a_Qf[k] / (   (1 - pl)*a_Qin[k]  )
DP_sum[k] = np.sum(DP[k,::])
DP_sum_2[k] = np.sum(DP_2[k,::])
T_diff[k] = abs(  (T2[k,yy-1] - Tout) / Tout  )
Trmax[k] = Tr2[k,yy-1]
hi_mean[k] = np.mean(hi[k,::])
m_rad[k] = np.sum(q_rad[k,::])
m_conv[k] = np.sum(q_conv[k,::])
m_Re[k] = np.mean(Re[k,::])
m_Rt[k] = (np.sum(1/Rt[k,::]))**-1
m_no_fi[k] = np.mean(no_fi[k,::])
```

```
#convert back to degree
T1 = T1-273
T2 = T2-273
Tr2 = Tr2 - 273
Tout = Tout - 273
Trmax = Trmax - 273
Pressure = np.array([DP_sum,DP_sum_2])
```

NUMERICAL CODE FOR OBTAINING THE RECEIVER PERFORMANCE PARAMETERS (TEMPERATURES, EFFICIENCIES AND PRESSURE DROP) FOR A GIVEN HEAT FLUX DISTRIBUTION

```
import numpy as np
from CoolProp.CoolProp import PropsSI
import matplotlib.pyplot as plt
from scipy.optimize import curve_fit

time_t = 18
delta_P   = 15250

degC = "\u00b0C"
def trans(p):
   return np.transpose(p)

clock = "{a}hrs".format(a = time_t)
if clock=="7hrs":
   time = 0
elif clock=="8hrs":
   time= 1
elif clock=="9hrs":
   time= 2
elif clock=="10hrs":
   time = 3
elif clock=="11hrs":
   time = 4
elif clock == "12hrs":
   time = 5
elif clock == "13hrs":
```

```
    time = 6
elif clock == "14hrs":
    time = 7
elif clock == "15hrs":
    time = 8
elif clock == "16hrs":
    time = 9
elif clock == "17hrs":
    time = 10
elif clock == "18hrs":
    time = 11
else:
    time = 80000



e = 0.95             # emissivity constant
pl = 0.05            # reflectivity constant

Bo = 5.67e-8         #Boltzmann constant
tmy = np.array([26.1,27.2,29.4,32.2,33.9,36.1,38.9,39.4,39.4,40.6,39.4,37.2])

Ta = tmy[time] + 273.15     #ambient temperature
Td = Ta
ha  = 8.8            #convective heat loss coefficient of the air
Tin = 550 + 273      #inlet temperature of CO2 supercritical
P = 1.92e7           #fixed pressure through the pin-array

d = 4e-4             #the thickness of the film before heat transfer
```

```
#curve fit function
def T_from_H(h):
    Tempo = np.linspace(800,1200,40)
    H_big = np.zeros(len(Tempo))
    for i in Tempo:
        H_big = (PropsSI('H','P',P,'T',Tempo,'CO2'))
    def objective(x,a,b):
        return a*x + b

    popt, _ = curve_fit(objective, H_big, Tempo)
    a, b = popt
    return a*h + b

aa = 25     #Number of packs modules horizontal (g index)
bb = 50     #Number of modules vertical  10*5 (h index)
zz = 6      #Number of unit cells in a module (k)
xx = 6      #Number of columns in a unit cell(j)
yy = 5      #Number of rows on the strip 25/5 (i)

'''
hence
modules units = 50*25
module control volume x-axis = 6(xx) * 6(zz) * 25(aa) = 900
module control volume y-axis = 5(yy) * 50(bb) = 250
'''

l = 0.99684            # length of the receiver
w = 0.984/5            # width of the receiver

N = xx*zz
```

```
dx = l/(6*xx)          # sectional length   --index zz, which changes with length of section

dy = w/yy

A = dx*dy


Hpin = np.zeros(bb)

Hpin[0] = 0.525e-3; Hpin[1] = 0.65e-3; Hpin[2] = 0.85e-3; Hpin[3] = 1.0e-3; Hpin[4] = 1.2e-3; Hpin[5] =
1.4e-3;

Hpin[6] = 1.6e-3; Hpin[7] = 1.75e-3; Hpin[8] = 1.925e-3; Hpin[9:11] = 2.0e-3;

Hpin[11] = 2.025e-3; Hpin[12] = 2.05e-3; Hpin[13] = 2.075e-3; Hpin[14] = 2.025e-3;Hpin[15] = 2.075e-3;

Hpin[16:32] = 2.0e-3; Hpin[32] = 2.025e-3; Hpin[33:38] = 2.1e-3; Hpin[38] = 2.125e-3;

Hpin[40:38:-1] = Hpin[9:11]

Hpin[41] = 1.85e-3; Hpin[42] = 1.7e-3; Hpin[43] = 1.5e-3; Hpin[44] = 1.3e-3; Hpin[45] = 1.15e-3

Hpin[46] = 0.975e-3 ;Hpin[47] = 0.8e-3; Hpin[48] = 0.625e-3 ; Hpin[49] = 0.50e-3;


Hpin[7] +0.07e-3

Hpin = Hpin - 0.07e-3

np.mean(Hpin)

#2 = 0.8mm 3 seems fine, and 4 change to 1mm, try 1.4 for row 6. Just make it 1.8 from9 to 37

#1.calculate the maximum velocity through flow

#Sd1 = np.sqrt(Sl**2 + (St**2/2)**2)

#Sd1

#pass1 = (St + Wpin)/2

#Sd1 > (St + D)/2 hence we have a transverse plane


##

#Building the flux distribution array. Make sure to have a  header and skip it to avoid errors.

Ts_2raw = np.genfromtxt('C:\\Users\\raymo\\OneDrive\\Documents\\A Thesis
Research\\action_folder\\Codes\\python_codes\\4_CSP codes\\{a}hrs-900x250-
flux.csv'.format(a=time_t),

                dtype=np.float32,skip_header = 1, delimiter = ',')

Ts_2 = Ts_2raw/10
```

```
#build an array to model the 2_D flow distribution with reverse flows
ICn = np.zeros([aa,bb*yy,zz*xx])
ICnn = np.zeros([aa,bb,yy,zz*xx])
IC = np.zeros([aa,bb,zz,yy,xx])



for a in range(aa):
   ICn[a,::,::] = Ts_2[::,(a*xx*zz):((a+1)*(xx*zz)):1]
   for b in range(bb):
      ICnn[a,b,::,::] = ICn[a,(b*yy):((b+1)*yy):1]
      for k in range(zz):
         IC[a,b,k,::,::] = ICnn[a,b,::,(k*xx):((k+1)*xx):1 ]  #must get array before reversing the N-1 rows
         for i in range(yy):
            if (k%2!= 0):
               IC[a,b,k,i,::]= IC[a,b,k,i,::-1]    #loop to invert the values of the 2nd, 4th and 6th sections

ta = np.mean(IC[::,0:10,::,::,::])
tb = np.mean(IC[::,10:40,::,::,::])
tc = np.mean(IC[::,40:50,::,::,::])
tm = (ta*10 + tb*30 + tc*10 ) / 50

#Arrays for model
Tr2 = np.zeros([aa,bb,zz,yy,xx])
T2  = np.zeros([aa,bb,zz,yy,xx]) #T(x+dx)
T1  = np.zeros([aa,bb,zz,yy,xx]) #Tx = fluid inlet temperature at every section
Qin = np.zeros([aa,bb,zz,yy,xx])  #Inlet heat at sections based on energy balance
ku  = np.zeros([aa,bb,zz,yy,xx])  #conductivity of Haynes
```

```
Qf  = np.zeros([aa,bb,zz,yy,xx])   #fluid temperature
Eff = np.zeros([aa,bb,zz,yy,xx])
h1  = np.zeros([aa,bb,zz,yy,xx])  #enthalpy at inlet
h2  = np.zeros([aa,bb,zz,yy,xx])  #enthalpy at outlet

rho      = np.zeros([aa,bb,zz,yy,xx])
Vmax     = np.zeros([aa,bb,zz,yy,xx])
fD       = np.zeros([aa,bb,zz,yy,xx])
Re_2     = np.zeros([aa,bb,zz,yy,xx])

m        = 0          #mass flow rate of CO2
m_1      = np.zeros([aa,bb,zz,yy])
Tout     = np.zeros([aa,bb,zz,yy])


P_diff = np.ones([aa,bb,zz,yy])
DP = np.zeros([aa,bb,zz,yy,xx])
DP_sum = np.zeros([aa,bb,zz,yy])
n_fi = np.zeros([aa,bb,zz,yy,xx])
no_fi = np.zeros([aa,bb,zz,yy,xx])

#Section 4: Modular parameters
T_out_module = np.zeros([aa,bb])
Eff_module = np.zeros([aa,bb])
m_module = np.zeros([aa,bb])
Ts_max = np.zeros([aa,bb])
h_module = np.zeros([aa,bb])

#solving for the parameter distribution in the receiver
```

```
for g in range(aa):
   for h in range(bb):

      Wpin = 1.2e-3      #width of the pin
      Sl = 2.13e-3       #longitudinal pitch
      St = 2.46e-3       #transverse pitch

      Npin_t = w/ St      #Number of pins
      Npin_l = l/(Sl*6) #no of pins in a length of each sixth section

      Dlcmin =  4*(Hpin[h]*w - Npin_t*(Wpin*Hpin[h]) ) /  ( 2*( (w - Npin_t*Wpin) + Hpin[h]*Npin_t ) )
#hydraulic diameter = 4*Area/P
      Dh = Wpin
      Across = Hpin[h]*w       #flow crosssectional area

      #define the mass flow function
      for k in range(zz):       #zz
         def m_flow(Hpin):
            T = 670 + 273
            Wpin = 1.2e-3      #width of the pin
            Sl = 2.13e-3       #longitudinal pitch
            St = 2.46e-3
            w  = 0.20/yy
            l = 0.166

            Npin_t = w/ St      #Number of pins
            Npin_l = l/Sl #no of pins in a length of each sixth section

            Dlcmin =  4*(Hpin*w - Npin_t*(Wpin*Hpin) ) /  ( 2*( (w - Npin_t*Wpin) + Hpin*Npin_t ) )
#hydraulic diameter = 4*Area/P
            Dh = Wpin
```

```
    Across = Hpin*w

    rho = PropsSI('D','P',P,'T',T,'CO2') #density of supercritical CO2
    uu = PropsSI('V','P',P,'T',T,'CO2')

    error = 1
    fD_guess = 2.0
    it = 0
    while error > 0.001:
        Vmax = np.sqrt( delta_P / ( fD_guess * 0.5 * rho * (Npin_l) )  )
        Re = rho * Vmax * Dlcmin / uu
        fD = 9.2 * (Hpin/Dh) **(-0.43) * ((St - Dh)/Dh)**0.07 *((Sl - Dh)/Dh)**0.07*Re**(-0.15)
        error = abs( (fD_guess - fD)/fD )
        fD_guess = fD
        it = it + 1

    V = Vmax /(St / (St - Wpin))                #maximum velocity in flow direction
    m_1 = rho * Across * V
    #print ('mass_flow' = m_1, "iter" = it, "friction_factor" = fD)
    return (m_1)
if g == 0:
   m = m_flow(Hpin[h])   #for heights considered, fd_2 varies from 1.4 to 2.6
else:
   m = m_1[g-1,h,k,i]
for i in range(yy):     #yy #it solves for each i, along the columns
    q = 0
    it_b = 0
    while (P_diff[g,h,k,i] > 0.005):
        if (i==0):
            m_1[g,h,k,i] = m*(1 +(0.001*q))
```

```
            else:
                m_1[g,h,k,i] = m_1[g,h,k,i-1]*(1 +(0.001*q))
            if(DP_sum[g,h,k,i] < delta_P):
                q+=1
            else:
                q-=1
            for j in range(xx): #xx   by moving from j to j because thats the flow pattern


                if(j==0):
                 T1[g,h,k,i,j] = Tin
                else:
                   T1[g,h,k,i,j] = T2[g,h,k,i,(j-1)]


                Qin[g,h,k,i,j] = IC[g,h,k,i,j]*A*1e4
                rho[g,h,k,i,j] = PropsSI('D','P',P,'T',T1[g,h,k,i,j],'CO2') #density of supercritical CO2


                V = m_1[g,h,k,i] *yy / (rho[g,h,k,i,j] * Across)                    #I am not sure about the area
                Vmax[g,h,k,i,j] = V * (St / (St - Wpin))              #maximum velocity in flow direction


                Cp = PropsSI('C','P',P,'T',T1[g,h,k,i,j],'CO2')     #Cp of CO2
                kf = PropsSI('L','P',P,'T',T1[g,h,k,i,j],'CO2')     #conductivity of fluid beetween 500 and 600
                uu = PropsSI('V','P',P,'T',T1[g,h,k,i,j],'CO2')     #dynamic viscosity between 500 and 60°C
(engineering toolbox)
                Pr = (uu/rho[g,h,k,i,j]) / ( kf/(rho[g,h,k,i,j] * Cp) )


                Re_2[g,h,k,i,j] = rho[g,h,k,i,j] * Vmax[g,h,k,i,j] * Dh / uu


                #1 using Erfan correlation
                Re = rho[g,h,k,i,j] * Vmax[g,h,k,i,j] * Dlcmin / uu                #Reynold's number
                Nu = 0.039*( (Sl - Dlcmin)/Dlcmin )**(-0.19) * Re**0.837 * Pr**0.557 #Nusslet number
```

```
            hi  = Nu * kf/Dlcmin  #convective heat transfer coefficient of the pin based on Dh = Dlcmin
for square form


            fD[g,h,k,i,j] = 9.2 * (Hpin[h]/Dh) **(-0.43) * ((St - Dh)/Dh)**0.07 *((Sl -
Dh)/Dh)**0.07*Re**(-0.15)


            DP[g,h,k,i,j] = ( fD[g,h,k,i,j] * 0.5 * rho[g,h,k,i,j] * Vmax[g,h,k,i,j]**2 * (Npin_l/xx))
            #iteration to solve for the surface temperature


            if(j==0):
              Tr = 800
            else:
               Tr = Tr2[g,h,k,i,j-1]
            it_a = 0
            error = 1
            cc1 = 0
            cc2 = 0
            while (error > 0.0005):
               ku[g,h,k,i,j] = 0.0191*Tr + 10.627    #conductivity of the haynes230 #move into the loop
               m_fi = np.sqrt( ( hi * np.pi*Wpin )/ (ku[g,h,k,i,j] * 0.25*np.pi*Wpin**2))
               n_fi[g,h,k,i,j] = np.tanh(m_fi*Hpin[h])/ (m_fi*Hpin[h])


               Af_fi = np.pi*Wpin*Hpin[h]    #fin exposed area, for one fin Af =P x L
               At_fi = (Npin_l/xx*Npin_t/yy)*Af_fi  +  (A - (Npin_l/xx*Npin_t/yy)*0.25*np.pi*Wpin**2 )


               no_fi[g,h,k,i,j] = 1 - Af_fi/At_fi * (  Npin_l/xx) *(Npin_t/yy) * (1 - n_fi[g,h,k,i,j])
               Rt      =  (1 / At_fi) * (1/(hi*no_fi[g,h,k,i,j]))    #overall resistance
               cc1 = 1 / (0.5 + Rt * (m_1[g,h,k,i]) * Cp)
               cc2 = (T1[g,h,k,i,j] * (0.5 - Rt*(m_1[g,h,k,i])*Cp) )/ (0.5+Rt*(m_1[g,h,k,i])*Cp)
               Tr2[g,h,k,i,j] = (  Qin[g,h,k,i,j]*(1-pl) + (m_1[g,h,k,i])*Cp*(cc2 + T1[g,h,k,i,j]) + ha*(A)*Ta -
                     e*Bo*(A)*(Tr**4 - Td**4)  ) /  (m_1[g,h,k,i]* Cp* cc1 + ha*A )
```

```
                error = abs ( (Tr2[g,h,k,i,j] - Tr)/Tr )
                Tr = 0.5*(Tr2[g,h,k,i,j] + Tr)
                it_a = it_a + 1

            T2[g,h,k,i,j] = cc1*Tr2[g,h,k,i,j] - cc2
            h1[g,h,k,i,j] = PropsSI('H','P',P,'T',T1[g,h,k,i,j],'CO2')  #enthalpy at CV inlet section
            h2[g,h,k,i,j] = PropsSI('H','P',P,'T',T2[g,h,k,i,j],'CO2')  #enthalpy at  CV outlet section
            Qf[g,h,k,i,j] = (m_1[g,h,k,i])*(h2[g,h,k,i,j] - h1[g,h,k,i,j])         #CV fluid heat transfer
            Eff[g,h,k,i,j] =  Qf[g,h,k,i,j] / ( (1-pl)*Qin[g,h,k,i,j] )
            it_b = it_b + 1

        DP_sum[g,h,k,i] = np.sum(DP[g,h,k,i,::])
        P_diff[g,h,k,i] = abs(  (DP_sum[g,h,k,i] - delta_P) / DP_sum[g,h,k,i]  )
        Tout[g,h,k,i] = T2[g,h,k,i,xx-1]

    Ts_max[g,h]      = np.amax(Tr2[g,h])
    T_out_module[g,h] = np.mean(Tout[g,h,::,::])
    h_module[g,h]  =  (PropsSI('H','P',P,'T',T_out_module[g,h],'CO2'))
    m_module[g,h]   = np.sum(m_1[g,h,::,::])
    Eff_module[g,h] = np.mean(Eff[g,h,::,::,::])
T_out_receiver = np.mean(T_out_module)



#Convert to celsius
Tr2 = Tr2-273
T2 = T2 - 273
Tout = Tout - 273
Ts_max = Ts_max -273
T_out_module = T_out_module - 273
T_out_receiver = T_out_receiver - 273
```

```
#Arrays for reversing
#Temperature
Tr2_r = Tr2
Tr2_4 = np.zeros([aa,bb,yy,zz*xx])
Tr2_3 = np.zeros([aa,bb*yy,zz*xx])
Tr2_2 = np.zeros([bb*yy,aa*zz*xx])

#Velocity
Vmax_r = Vmax
Vmax_4 = np.zeros([aa,bb,yy,zz*xx])
Vmax_3 = np.zeros([aa,bb*yy,zz*xx])
Vmax_2 = np.zeros([bb*yy,aa*zz*xx])

#Efficiency
Eff_r = Eff
Eff_4 = np.zeros([aa,bb,yy,zz*xx])
Eff_3 = np.zeros([aa,bb*yy,zz*xx])
Eff_2 = np.zeros([bb*yy,aa*zz*xx])

#mass flux
m_4 = np.zeros([aa,bb,yy,zz])
m_3 = np.zeros([aa,bb*yy,zz])
m_2 = np.zeros([bb*yy,aa*zz])



for k in range (zz):
   for i in range(yy):
      if (k%2!=0):
         Tr2_r[::,::,k,i,::] = Tr2[::,::,k,i,::-1]
```

```
        Vmax_r[::,::,k,i,::] = Vmax[::,::,k,i,::-1]
        Eff_r[::,::,k,i,::] = Eff[::,::,k,i,::-1]
for k in range (zz):
    Tr2_4[::,::,::,(k*xx):((k+1)*xx):1] = Tr2_r[::,::,k,::,::]
    Vmax_4[::,::,::,(k*xx):((k+1)*xx):1] = Vmax_r[::,::,k,::,::]
    Eff_4[::,::,::,(k*xx):((k+1)*xx):1] = Eff_r[::,::,k,::,::]
    m_4[::,::,::,k] = m_1[::,::,k,::]
    for b in range(bb):
        Tr2_3[::,(b*yy):((b+1)*yy):1] = Tr2_4[::,b,::,::]
        Vmax_3[::,(b*yy):((b+1)*yy):1] = Vmax_4[::,b,::,::]
        Eff_3[::,(b*yy):((b+1)*yy):1] = Eff_4[::,b,::,::]
        m_3[::,(b*yy):((b+1)*yy):1,::] = m_4[::,b,::,::]
        for a in range(aa):
            Tr2_2[::,(a*xx*zz):((a+1)*(xx*zz)):1] = Tr2_3[a,::,::]
            Vmax_2[::,(a*xx*zz):((a+1)*(xx*zz)):1] = Vmax_3[a,::,::]
            Eff_2[::,(a*xx*zz):((a+1)*(xx*zz)):1] = Eff_3[a,::,::]
            m_2[::,(a*zz):((a+1)*zz):1] = m_3[a,::,::]
```

NUMERICAL CODE FOR CONDUCTING UNCERTAINTY ANALYSIS OF A MPAR RECEIVER MODULE'S PERFORMANCE PARAMETERS

```
import numpy as np

from CoolProp.CoolProp import PropsSI


dTs_2 = np.genfromtxt('C:\\Users\\raymo\\OneDrive\\Documents\\A Thesis
Research\\action_folder\\Codes\\python_codes\\6_analysis code\\py_Tprofile_2b.csv',

                dtype=None,skip_header = 0, delimiter = ',')



Ts_2 = dTs_2 + 50

Ts_2 = Ts_2 + 273


Ts_2.shape

#dTs_3.shape

#surface temperature distribution with maximum of 800 and minimum of 500 T - quadratic

l = 0.15            # length of the receiver

w = 0.15            # width of the receiver


e = 0.95            # emissivity constant

pl = 0.05           # reflectivity constant


Bo = 5.67e-8        #Boltzmann constant

Td = 45 +273.15     #dish temperature

Ta = 30 + 273.15    #ambient temperature

ha  = 8.8           #convective heat loss coefficient of the air

m  = 0.138/6          #mass flow rate of CO2 in kg

Tin = 550 + 273     #inlet temperature of CO2 supercritical

P = 1.92e7          #fixed pressure through the pin-array
```

```
d = 4e-4            #the thickness of the film before heat transfer



Hpin = 200e-6       #height of the pin

Wpin = 500e-6       #width of the pin

Sl = 1000e-6        #longitudinal pitch

St = 1000e-6        #transverse pitch

Npin_t = w/ St      #Number of pins

Npin_l = l/(Sl*6) #no of pins in a length of each sixth section

N  = Npin_t + 1           #number of sections

N  = int(N)

dx = l/(N-1)          # sectional length

A = dx*w          #area of a dx section

Dlcmin =  4*(Hpin*w - Npin_t*(Wpin*Hpin) ) /  ( 2*( (w - Npin_t*Wpin) + Hpin*Npin_t ) ) #hydraulic
diameter = 4*Area/P

Dh = np.sqrt(4*Wpin**2/np.pi)

Across = Hpin*w - Npin_t*Wpin*Hpin #flow crosssectional area

#Dlcmin and Dh are the same

#1.calculate the maximum velocity through flow

Sd1 = np.sqrt(Sl**2 + (St**2/2)**2)

Sd1

pass1 = (St + Wpin)/2

#Sd1 > (St + D)/2 hence we have a transverse plane
```

```
#build an array to model the 2_D flow distribution with reverse flows
xx = (N - 1)/6
xx = int(xx)
yy = N - 1
zz = 6

Ts_arr = np.zeros([zz,yy,xx])



for k in range(zz):
   Ts_arr[k,::,::] = Ts_2[::, (k*xx):(xx*(k+1) ):1 ]  #must get array before reversing the N-1 rows
   for i in range(yy):
      if (k%2!= 0):
         Ts_arr[k,i,::]= Ts_arr[k,i,::-1]   #loop to invert the values of the 2nd, 4th and 6th sections



#Arrays for model
IC = np.zeros([zz,yy,xx]) #heat flux incident
T2 = np.zeros([zz,yy,xx]) #T(x+dx)
T1 = np.zeros([zz,yy,xx]) #Tx = fluid inlet temperature at every section

ku =  np.zeros([zz,yy,xx])  #conductivity of Haynes

Eff = np.zeros([zz,yy,xx])  #efficiency at control volume
h1  = np.zeros([zz,yy,xx])  #enthalpy at inlet
h2  = np.zeros([zz,yy,xx])  #enthalpy at outlet
Tout = np.zeros(6)

Qin = np.zeros([zz,yy,xx])  #Inlet heat at sections based on energy balance
```

```
Qf = np.zeros([zz,yy,xx])   #fluid temperature
Qrad = np.zeros([zz,yy,xx])
Qconv = np.zeros([zz,yy,xx])

#Section 4: Uncertainty data
#Arrays for uncertainty quantities

u_c = np.zeros([zz,yy,xx])
u_ra = np.zeros([zz,yy,xx])
u_f = np.zeros([zz,yy,xx])
u_T2 = np.zeros([zz,yy,xx])
u_T1 = np.zeros([zz,yy,xx])
u_Qi = np.zeros([zz,yy,xx])
u_nth = np.zeros([zz])
u_re  = np.zeros([zz])
punth = np.zeros([zz])
purec = np.zeros([zz])

a_Qf  = np.zeros([zz])
a_Qin = np.zeros([zz])
n_th  = np.zeros([zz])
n_rec = np.zeros([zz])

#estimating the errors in the measurements
#assuming the errors in thermocouple, IR imaging, and receiver dimension measurement are elemental errors
#with a normal distribution
#assuming a normal distribution
be  = 0.02/1.96        #error in emissivity
bA  = 0                #uncertainty in the length or breadth of receiver
```

```
bTs = 1.1/1.96       #uncertainty in the surface temperature
bTd = 0.5/1.96       #uncertainty in the dish temperature
bTa = 0.5/1.96       #uncertainty in the ambient temperature measurement
bh  = 0.5/1.96       #uncertainty in the convective loss coefficient
bm  = ( (0.1/100)/1.96)*(m/yy) #uncertainty in the mass flow rate
bTi = 1.1/1.96       #uncertainty in T1;the inlet temperature measurement
bpl = 0.015      #uncertainty in the reflectivity constant

#Section 5:
#solving for the parameter distribution in the receiver

for k in range(zz):        #zz
   for i in range(yy):     #yy #it solves for each i, along the columns
      for j in range(xx): #xx   by moving from j to j because thats the flow pattern



         if(j==0):
           T1[k,i,j] = Tin
         else:
            T1[k,i,j] = T2[k,i,(j-1)]
         rho = PropsSI('D','P',P,'T',T1[k,i,j],'CO2') #density of supercritical CO2

         V = m / (rho * Across)                    #I am not sure about the area
         Vmax = V * (St / (St - Wpin))               #maximum velocity in flow direction
         Cp = PropsSI('C','P',P,'T',T1[k,i,j],'CO2')     #Cp of CO2
         kf = PropsSI('L','P',P,'T',T1[k,i,j],'CO2')     #conductivity of fluid beetween 500 and 600
         uu = PropsSI('V','P',P,'T',T1[k,i,j],'CO2')     #dynamic viscosity between 500 and 60°C (engineering
toolbox)
         Pr = (uu/rho) / ( kf/(rho * Cp) )
```

```
#1 using Erfan correlation

Re = rho * Vmax * Dlcmin / uu                #Reynold's number


Nu = 0.039*( (Sl - Dh)/Dh )**(-0.19) * Re**0.837 * Pr**0.557 #Nusslet number


hi  = Nu * kf/Dlcmin  #convective heat transfer coefficient of the pin based on Dh = Dlcmin for
square form


ku[k,i,j] = 0.02*Ts_arr[k,i,j] + 8.4    #conductivity of the haynes230 #move into the loop


m_fi = np.sqrt( ( hi * 4 * Wpin )/ (ku[k,i,j] * Wpin**2))

n_fi = np.tanh(m_fi*Hpin)/ (m_fi*Hpin)


At_fi = St*Sl

Af_fi = 4*Wpin*Hpin

no_fi = 1 - Af_fi/At_fi * (1 - n_fi)

Rt    = 1 / ( At_fi * (hi*no_fi + ku[k,i,j]/d) )   #overall resistance


T2[k,i,j] =  ( Ts_arr[k,i,j] - T1[k,i,j]*(0.5 - Rt*(m/yy)*Cp) ) / ( 0.5 + Rt*(m/yy)*Cp ) #CV outlet
Temperature


h1[k,i,j] = PropsSI('H','P',P,'T',T1[k,i,j],'CO2')  #enthalpy at CV inlet section

h2[k,i,j] = PropsSI('H','P',P,'T',T2[k,i,j],'CO2')  #enthalpy at  CV outlet section


Qf[k,i,j] = (m/yy)*(h2[k,i,j] - h1[k,i,j])         #CV fluid heat transfer

Qin[k,i,j] =  ( Qf[k,i,j]  +  ha*(dx*dx)*(Ts_arr[k,i,j] - Ta) + e*Bo*(dx*dx)*(Ts_arr[k,i,j]**4 - Td**4)  )
/ (1 - pl)


Qconv[k,i,j] = ha*(dx*dx)*(Ts_arr[k,i,j] - Ta)

Qrad[k,i,j] = e*Bo*(dx*dx)*(Ts_arr[k,i,j]**4 - Td**4)
```

```
IC[k,i,j] = Qin[k,i,j] / (dx * dx * 1e4)



#Uncertainty calculations
if(j==0):
  u_T1[k,i,j] = bTi
else:
   u_T1[k,i,j] = u_T2[k,i,(j-1)]

#uncertainty in fluid temperature
dTss = 1/(0.5 + Rt*(m/yy)*Cp)
dTxx = (0.5 - Rt*(m/yy)*Cp)/(0.5 + Rt*(m/yy)*Cp)
dmm  = -Rt*Cp*(Ts_arr[k,i,j] + 2*Rt*(m/yy)*Cp*T1[k,i,j])  / (0.5 + Rt*(m/yy)*Cp)**2

u_T2[k,i,j] = np.sqrt(dTss**2*bTs**2 + dTxx**2*u_T1[k,i,j]**2  + dmm**2*bm**2)

#sensitivity coefficients and uncertainties
#radiation sensitivity coefficients
de    =  dx*Bo*(Ts_arr[k,i,j]**4 - Td**4)          #sensitivity coefficient of emissivity constant
dAr   =  2*e*Bo*dx*(Ts_arr[k,i,j]**4-Td**4)       #sensitivity coefficient of area
dTsr  =  e * Bo * dx**2 * 4 * Ts_arr[k,i,j]**3      #sensitivity coefficient for surface temeprature error in radiation
dTd   = -e * Bo * dx**2 * 4 * Td**3     #sensitivity coefficient of the dish surface temperature

#radiation losses
ue      = np.sqrt(de**2 * be**2)  #uncertainty in emissivity
uAr     = np.sqrt(dAr**2 * bA**2)  #uncertainty in the area of receiver
uTsr    = np.sqrt(dTsr**2 * bTs**2) #uncertainty in the surface temperature
uTd     = np.sqrt(dTd**2 * bTd**2) #uncertainty in dish tempeature
u_ra[k,i,j] = np.sqrt(ue**2 + uAr**2 + uTsr**2 + uTd**2 + 2*dTsr*dTd*bTs*bTd) #uncertainty in radiative heat loss
```

```
#convection sensitivity coefficients

dTa  = -ha * dx**2                #sensitivity coefficient of ambient temperature error

dTsc = ha * dx**2              #sensitivity coefficient for surface temeprature error in convection

dh   = dx**2 * (Ts_arr[k,i,j] - Ta)          #sensitivity coefficient of convective heat transfer coefficient

dAc  = ha * 2 * dx * ( Ts_arr[k,i,j] - Ta )  #sensitivity coefficient of the area


#convective heat losses

uh   = np.sqrt(dh**2 * bh**2)     #uncertainty in convective heat transfer coefficient

uAc  = np.sqrt(dAc**2 * bA**2)    #uncertainty in area of receiver

uTsc = np.sqrt(dTsc**2 * bTs**2) #uncertainty in dish surface temperature

uTa  = np.sqrt(dTa**2 * bTa**2)   #uncertainty in ambient temperature

u_c[k,i,j] = np.sqrt(uh**2 + uAc**2 + uTsc**2 + uTa**2 + 2*dTsc*dTa*bTs*bTa)  #uncertainty in convective heat transfer.


#Fluid energy sensitivity coefficient

dm  = h2[k,i,j] - h1[k,i,j]   #sensitivity coefficient of mass flow

dTo =  (m/yy)         #sensitvity coefficient of outlet Temperature

dTi = -(m/yy)         #sensitivity coefficient of inlet temperature


#heat transfer to fluid

um    = np.sqrt(dm**2  * bm**2) #uncertainty in mass measurement

uTi   = np.sqrt(dTi**2 * u_T1[k,i,j]**2) #uncertainty in inlet temperature

uTo   = np.sqrt(dTo**2 * u_T2[k,i,j]**2) #uncertainty in outlet temperature

u_f[k,i,j] = np.sqrt(um**2 + uTi**2 + uTo**2 + 2*dTi*dTo*u_T1[k,i,j]*u_T2[k,i,j])  #uncertainty in fluid heat transfer by considering the correlation of the errors


#uncertainty in Energy balance: uncertainty in Qincident

u_Qi[k,i,j] = np.sqrt(u_f[k,i,j]**2 + u_c[k,i,j]**2 + u_ra[k,i,j]**2)
```

```
   Tout[k] =np.mean(T2[k,:,xx-1])     #mean of all rows at the outlet section @ index xx - 1 = outlet temperature


   #2.0 total heat values
   a_Qf[k]   = np.sum( Qf[k,::,::] )          #Qfluid = mcdT for each of the 6 sections
   a_Qin[k]  = np.sum(Qin[k,::,::] )          #Qincident for each of the 6 sections


   #2.1uncertainty values
   ou_f = np.sqrt(np.sum(u_f[k,::,::]**2))
   ou_q = np.sqrt(np.sum(u_Qi[k,::,::]**2))


   #2.2 Efficiency values
   n_th[k]   = a_Qf[k] / (   (1 - pl)*a_Qin[k]  ) #thermal efficiency (does not acccouts for reflectivity)
   n_rec[k]  = a_Qf[k] / a_Qin[k]              #receiver efficiency



   #Receiver Efficiency sensitivity coefficients
   dQf2 = 1/a_Qin[k]             #sensitivity coefficient in fluid heat transfer
   dQi2 = -a_Qf[k]/(a_Qin[k]**2)   #sensitivity coefficient in incident heat


   #uncertainty in receiver efficiency
   udQi2 = np.sqrt(dQi2**2 * ou_q**2)
   udQf2 = np.sqrt(dQf2**2 * ou_f**2)
   u_re[k] = np.sqrt(udQi2**2  + udQf2**2)



   #Thermal Efficiency sensitivity coefficients
   dQf =  1/( (1 - pl) * a_Qin[k] )
   dpl = -a_Qf[k]/a_Qin[k]*(1/(1-pl)**2)
```

```
    dQi = -a_Qf[k]/(1-pl) * (1/a_Qin[k]**2)

    #uncertainty in thermal efficiency
    udQf = np.sqrt(dQf**2 * ou_f**2)
    udpl = np.sqrt(dpl**2 * bpl**2 )
    udQi = np.sqrt(dQi**2 * ou_q**2)
    u_nth[k] = np.sqrt(udQf**2 + udQi**2 + udpl**2) #uncertainty in the efficiency value


    punth[k] = u_nth[k]/n_th[k]*100   #percentage thermal uncertainy in each of 6 sections
    purec[k] = u_re[k]/n_rec[k]*100   #percentage receiver uncertainty in each of 6 sections.


#3.0 Total quantity calculations
QT_q = np.sum(a_Qin)
QT_f = np.sum(a_Qf)
QT_r = np.sum(Qrad)
QT_c = np.sum(Qconv)
#3.1 Total uncertainty calculations
uT_q = np.sqrt(np.sum(u_Qi**2))
uT_f = np.sqrt(np.sum(u_f**2))
uT_r = np.sqrt(np.sum(u_ra**2))
uT_c = np.sqrt(np.sum(u_c**2))

#3.2a Receiver Efficiency sensitivity coefficients
TdQf2 = 1/QT_q              #sensitivity coefficient in fluid heat transfer
TdQi2 = -QT_f/(QT_q**2)   #sensitivity coefficient in incident heat

#3.2b Thermal Efficiency sensitivity coefficients
TdQf = 1/( (1 - pl) * QT_q )
```

```
Tdpl = -QT_f/QT_q*(1/(1-pl)**2)
TdQi = -QT_f/(1-pl) * (1/QT_q**2)

#3.3a uncertainty in receiver efficiency
TudQi2 = np.sqrt(TdQi2**2 * uT_q**2)
TudQf2 = np.sqrt(TdQf2**2 * uT_f**2)
Tu_re = np.sqrt(TudQi2**2  + TudQf2**2)

#3.3b uncertainty in thermal efficiency
TudQf = np.sqrt(TdQf**2 * uT_f**2)
Tudpl = np.sqrt(Tdpl**2 * bpl**2 )
TudQi = np.sqrt(TdQi**2 * uT_q**2)
Tu_nth = np.sqrt(TudQf**2 + TudQi**2 + Tudpl**2) #uncertainty in the efficiency value

#3.4 new quantities
Tn_th = QT_f / (   ( 1 - pl  )*QT_q  ) #total thermal efficiency
Tn_rec = QT_f  / QT_q              #total receiver efficiency

#3.5 Total percentage uncertainties
Tpurad = uT_r/QT_r * 100
Tpucon = uT_c/QT_c * 100
Tpuqf = uT_f/QT_f * 100
Tpuqin = uT_q/QT_q * 100

Tpunth = Tu_nth/Tn_th*100  #total percentage uncertainty in thermal efficiency
Tpurec = Tu_re/Tn_rec*100   #total percentage uncertainty in receiver efficiency
#convert back to degree
T1 = T1-273
T2 = T2-273
Tout = Tout - 273
```